

“The difference between what we do and what we are capable of doing would suffice to solve most of the world's problems.”

- ‘Mahatma’ Mohandas K. Gandhi

1869 – 1948

University of Alberta

Use of the Confined Impinging Jet Reactor for Production of
Nanoscale Iron Oxide Particles

by

Shad Waheed Siddiqui

A thesis submitted to the Faculty of Graduate Studies and Research
in partial fulfillment of the requirements for the degree of

Doctor of Philosophy

in

Chemical Engineering

Department of Chemical and Materials Engineering

©Shad Waheed Siddiqui

Fall, 2009

Edmonton, Alberta

Permission is hereby granted to the University of Alberta Libraries to reproduce single copies of this thesis and to lend or sell such copies for private, scholarly or scientific research purposes only. Where the thesis is converted to, or otherwise made available in digital form, the University of Alberta will advise potential users of the thesis of these terms.

The author reserves all other publication and other rights in association with the copyright in the thesis and, except as herein before provided, neither the thesis nor any substantial portion thereof may be printed or otherwise reproduced in any material form whatsoever without the author's prior written permission.

Examining Committee

Suzanne Kresta, Department of Chemical and Materials Engineering

Zhenghe Xu, Department of Chemical and Materials Engineering

Qi Liu, Department of Chemical and Materials Engineering

Subir Bhattacharjee, Department of Mechanical Engineering

Daniele Marchisio, Department of Materials Science and Chemical Engineering,
Politecnico di Torino, Italy

This work is dedicated to my family - my parents and my younger brother.

Abstract

The confined impinging jet reactor gives efficient mixing performance as required for fast reactions. In this work the mixing performance of CIJR is characterized through three measures: estimates of the energy dissipation, micromixing efficiency based on the yield of a homogeneous (iodide-iodate) reaction and particle size resulting from a heterogeneous (iron oxide) precipitation reaction. Whereas product yield and energy dissipation are used to test operational robustness of CIJR, iron oxide model system is used to study the effect of feed flow rate (mixing) and reactant concentration on precipitate agglomerate size. Mixing and concentration effects on nucleation, particle growth and particle agglomeration are tracked to understand the agglomeration process. Various types of stabilizers and additive concentrations to limit particle agglomeration are also tested. Effects of in situ and post-reaction sonication on agglomerate size are also investigated. Efforts are made to determine variations in mixing efficiency the operational robustness of the scale-up (2X and 4X) geometries. Also efforts are made to identify scaling parameters and the limit on geometric scale-up for good mixing performance.

Energy dissipation is found to vary between 20 W/kg and 6800 W/kg in CIJR and decreases on scale-up at constant Reynolds number. The operation of the CIJR and the scale-up geometries is robust to changes in flow rate, exhibiting stable performance up to 30% difference in inlet flow rates. Reliable mixing performance is obtained until 2X scale-up, while at low flow rates, the jets fail to impinge in 4X scale-up, and sometimes failing to fill the reactor volume.

Iron oxide primary and agglomerate particles are seen to vary with flow rate and reactant concentrations. Largest primary particles (and smallest agglomerates) are obtained at high flow rates and high reactant concentrations, which indicate to size dependent agglomerative tendency of the primary particles. Stabilizers added *in situ* see limited success. Post-reaction sonication is helpful in dispersing soft agglomerates, but *in situ* sonication shows no significant reduction in agglomerate size with or without stabilizer. Primary particles are understood to agglomerate due to collisions induced by Brownian motion, simple shear and velocity fluctuations in turbulent flows. These collision mechanisms operate at different length scales in the fluid mass.

Acknowledgements

My thanks are due to Dr. Suzanne Kresta and Dr. Zhenghe Xu for their guidance, support and encouragement throughout this work. I am thankful to the Umicore project committee members - Dr. Subir Bhattacharjee and Dr. Qi Liu for their help and advise.

I am where I am today because of my parents and my brother. They were always there whenever I needed them.

My thanks are due to my colleagues of the Mixing Group for their interest and in particular to Peter Unwin for helping me to collect TEM data and Alena Kukukova for the CFD simulations.

I appreciate the assistance of the technical staff, and in particular Walter Boddez and James Mckinnon.

I gratefully acknowledge our corporate partner of this project, Umicore Canada Inc., for their financial support.

May 27, 2009

780, CME
Edmonton

Table of Contents

Abstract

Acknowledgements

Table of Contents

List of Figures

List of Tables

Nomenclature

Roman characters

Greek letters

Chapter 1

Introduction	1
General background	1
Structure of this thesis	3
Literature cited	5

Chapter 2

Characteristics of a Confined Impinging Jet Reactor: Energy Dissipation, Homogeneous and Heterogeneous Reaction Products, and Effect of Unequal Flow	6
Introduction	6
Iodide-Iodate reaction	8
Estimation of energy dissipation rate	11
Micromixing reaction probe	11
Mechanical energy balance	14
Experimental setup and operating conditions	15
Iodide-Iodate reaction	16
Iron oxide reaction	17
CFD simulations	19

Results	20
Balanced Flow, Equal Momentum.....	21
Turbulence and Flow.....	21
Product yield in iodide-iodate reaction	23
Particle size in iron oxide precipitation reaction.....	24
Unequal Flow	24
Normalized energy dissipation rate.....	24
Product yield in Iodide-Iodate reaction.....	25
Conclusions	26
Tables	29
Figures.....	31
Literature cited	42

Chapter 3

Nanoparticle Precipitation, Agglomeration and its Control in Confined

Impinging Jet Reactor	47
Introduction	47
Experimental	54
Experimental setup.....	54
Iron oxide reaction	55
Iodide-Iodate reaction	56
Results	57
Flow rate, post-precipitation sonication and feed concentration.....	58
Stabilizer addition	59
Insitu sonication and geometry modification.....	61
Conclusions	64
Tables	66
Figures.....	69
Literature cited	80

Chapter 4

Nucleation, Particle Growth and Agglomeration Mechanisms of Nanoparticles in a Fast Precipitation Reaction in Confined Impinging Jet

Reactor	84
Introduction	84
Theory	87
Mixing, supersaturation and nucleation	88
Diffusional growth of nuclei to primary particles	91
Agglomeration of primary particles	93
Analysis	101
dp^* estimation:	101
d_p estimation:	101
d_{HA} estimation:	102
Experimental	104
Experimental setup	104
Iron oxide reaction	104
Results	106
Conclusions	110
Tables	112
Figures	116
Literature cited	124

Chapter 5

Scale-up of the Confined Impinging Jet Reactor: Energy Dissipation,

Reaction and Effect of Unequal Flow	130
Introduction	130
Experimental setup and operating conditions	135
Iodide-Iodate reaction	136
Results	136
Balanced Flow, Equal Momentum	137
Energy Dissipation Rate	137

Product Yield in Iodide-Iodate Reaction.....	138
Unequal Flow, Unequal Momentum.....	140
Normalized Energy Dissipation Rate.....	140
Product Yield in Iodide-Iodate Reaction.....	140
Conclusions.....	141
Tables.....	142
Da.....	143
Figures.....	144
Literature cited.....	155

Chapter 6

Conclusions and Future Work.....	156
Conclusions.....	156
Mixing characterization - CIJR.....	156
Nanoparticle agglomeration and control.....	157
Nucleation, particle growth and agglomeration mechanisms of nanoparticles	158
Mixing Characterization - Scale-up CIJR.....	158
Future work.....	159

List of Figures

Figure 2-1: CIJR schematic for energy dissipation rate calculation	31
Figure 2-2: CIJR schematic for mechanical energy balance.....	31
Figure 2-3: CIJR (a) dimensions, (b) construction, and (c) configuration of pressure transducers.	33
Figure 2-4: Effect of jet flow rate on reproducibility at $[H^+] = 0.0936$ M and buffer reagent $[H_2BO_3^-] = 0.1818$ M. Standard deviation $< 1.03 \times 10^{-4}$ for all flow rates.	34
Figure 2-5: Effect of jet flow rate on energy dissipation rate at (a) all flow rates and (b) low flow rates. Pressure drop (eqtn. 2-19), Mechanical Energy balance (eqtn. 2-20), Micromixing (eqtn. 2-14) and CFD approach based on the chamber volume.	35
Figure 2-6: Variation of energy dissipation rate in (a) axial direction and (b) radial direction with varying jet flow rates. The origin is placed at the impingement point.....	36
Figure 2-7: Mean velocity contours in CIJR at one time step for flow rates increasing from 70 mL/min to 500 mL/min. The maximum velocity (red) is a) 2.17 m/s, b) 4.44 m/s, c) 7.72 m/s, d) 12.6 m/s. The dark blue regions approach zero mean velocity in all figures.....	37
Figure 2-8: Residence time distribution in the CIJR computed from CFD simulations of tracer dispersion at four flow rates.	37
Figure 2-9: Effect o flow rate on product yield under varying limiting reagent concentration $[H^+]$ and for buffer reagent concentration $[H_2BO_3^-] = 0.1818$ M	38
Figure 2-10: Effect of jet flow rate on iron oxide mean particle size (D_{65})	38
Figure 2-11: Effect of unequal flow on normalized energy dissipation rate at (a) all flow rates and (b) flow rates > 165 mL/min. The flow rate of stream 1 is held constant at the given value, while the flow rate of stream 2 is reduced.	39

Figure 2-12: Effect of reduced sulfuric acid flow rate on product yield at (a) dilute: $[H^+] = 0.0936$ M and (b) high concentration: $[H^+] = 0.1818$ M. $[H_2BO_3^-] = 0.1818$ M for all experiments	40
Figure 2-13: Effect of reduced buffer flow rate on product yield at (a) dilute conditions $[H^+] = 0.0936$ M and b) high concentration, $[H^+] = 0.1818$ M. $[H_2BO_3^-] = 0.1818$ M for all experiments	41
Figure 3-1: Isometric view of CIJR and its dimensions.....	69
Figure 3-2: Effect of post-reaction sonication on iron oxide agglomerate size. $[Fe^{2+}] = 0.18$ M, $[Fe^{3+}] = 0.36$ M and $[OH^-] = 1.45$ M in all experiments...	70
Figure 3-3: Effect of post-reaction sonication on iron oxide agglomerate PSD. $[Fe^{2+}] = 0.18$ M, $[Fe^{3+}] = 0.36$ M, $[OH^-] = 1.45$ M and flow rate = 165 mL/min in the experiment.	70
Figure 3-4: Effect of jet flow rate and reactant concentrations on iron oxide particle size at (a) varying $[Fe^{2+}]$ and $[Fe^{3+}]$ and (b) varying $[OH^-]$. $[OH^-] = 1.45$ M in (a) and $[Fe^{2+}] = 0.18$ M and $[Fe^{3+}] = 0.36$ M in (b).....	71
Figure 3-5: Effect of (a) point of stabilizer addition and (b) various stabilizers and concentrations added in situ (to NaOH stream) on iron oxide agglomerate size. $[Fe^{2+}] = 0.18$ M, $[Fe^{3+}] = 0.36$ M, $[OH^-] = 1.45$ M and flow rate = 165 mL/min in all experiments.....	72
Figure 3-6: Effect of triethylene glycol v/v (added in situ) on iron oxide hard agglomerate size at (a) flow rate = 165 mL/min and (b) flow rate = 509 mL/min. $[OH^-] = 1.45$ M in all experiments.	73
Figure 3-7: Effect of triethylene glycol (TEG) added in situ on iron oxide particle size and morphology: (a) TEM image at $[TEG] = 5\%$ (v/v), (b) TEM image at $[TEG] = 50\%$ (v/v), (c) agglomerate PSD for $[TEG] = 5\%$ and 50% (v/v) and (d) primary PSD for $[TEG] = 50\%$ (v/v). $[Fe^{2+}] = 0.18$ M, $[Fe^{3+}] = 0.36$ M, $[OH^-] = 1.45$ M and flow rate = 165 mL/min in all experiments.	74
Figure 3-8: Effect of dextran added in situ on iron oxide agglomerate size at $[Fe^{2+}] = 0.18$ M, $[Fe^{3+}] = 0.36$ M and $[OH^-] = 1.45$ M for all experiments.	75

Figure 3-9: Effect of Dextran added in situ on iron oxide morphology and primary particle size: (a) TEM image and (b) primary PSD. [Dextran] = 2 mM and flow rate = 165 mL/min in all experiments.	75
Figure 3-10: Variation of energy dissipation rate in (a) axial direction and (b) radial direction at various jet flow rates. The origin is placed at the impingement point.....	76
Figure 3-11: Effect of jet flow rate and modified geometry on product yield in iodide-iodate reaction. [H ₂ BO ₃ ⁻] = 0.1818M in all experiments.....	77
Figure 3-12: Effect of in situ sonication on product yield in iodide-iodate reaction. [H ⁺] = 0.1818M and [H ₂ BO ₃ ⁻] = 0.1818M in all experiments.	77
Figure 3-13: Effect of in-situ sonication and stabilizer (added in situ) (a) no stabilizer, (b) 5% v/v triethylene glycol (TEG) and (c) 5% v/v polyacrylamide (PAM) on iron oxide agglomerate size. [Fe ²⁺] = 0.18 M, [Fe ³⁺] = 0.36 M, [OH ⁻] = 1.45 M and flow rate = 165 mL/min in all experiments.	79
Figure 3-14: Primary PSD in a hard agglomerate (a) with no in situ sonication and (b) 160 W input in situ sonication. [Fe ²⁺] = 0.18 M, [Fe ³⁺] = 0.36 M, [OH ⁻] = 1.45 M and flow rate = 165 mL/min in all experiments.....	79
Figure 4-1: Isometric view (a) of CIJR and (b) its dimensions.....	116
Figure 4-2: (a) TEM image of iron oxide hard agglomerate at magnification of (a) 500,000x and (b) 800,000x. [Fe ²⁺] = 0.18 M, [Fe ³⁺] = 0.36 M, [OH ⁻] = 1.45 M and flow rate = 509 mL/min.	117
Figure 4-3: A schematic of the process of hard agglomerate formation.....	118
Figure 4-4: Effects of colliding particle sizes (a) d _{p1} = 10nm, d _{p2} = 10, 30, 50, etc. and (b) d _{HA} = 200nm, d _{p2} = 10, 30, 50 nm etc. on collision frequency function in Brownian, laminar and turbulent agglomeration models.....	119
Figure 4-5: Effect of pH on iron oxide (a) agglomerate size and (b) primary particle size at flow rate = 500 mL/min. [Fe ²⁺] = 0.05 M, [Fe ³⁺] = 0.10 M and [OH ⁻] is varied between 0.39 M to 0.42 M in the experiments.	120
Figure 4-6: Effect of jet flow rate and varying ferrous-ferric concentration on iron oxide hard agglomerate size, nucleation and particle details at (1) [Fe ²⁺]	

= 0.01 M and 509 mL/min, (2) $[\text{Fe}^{2+}] = 0.036 \text{ M}$ and 509 mL/min, (3) $[\text{Fe}^{2+}] = 0.18 \text{ M}$ and 509 mL/min and (4) $[\text{Fe}^{2+}] = 0.18 \text{ M}$ and 165 mL/min. $[\text{Fe}^{3+}] = 2[\text{Fe}^{2+}]$, $[\text{OH}^-] = 1.45 \text{ M}$ in all experiments.	121
Figure 4-7: Primary PSD in a hard agglomerate at (a) $[\text{Fe}^{2+}] = 0.01 \text{ M}$, $[\text{Fe}^{3+}] = 0.02 \text{ M}$, (b) $[\text{Fe}^{2+}] = 0.036 \text{ M}$, $[\text{Fe}^{3+}] = 0.072 \text{ M}$ and (c) $[\text{Fe}^{2+}] = 0.18 \text{ M}$, $[\text{Fe}^{3+}] = 0.36 \text{ M}$. $[\text{OH}^-] = 1.45 \text{ M}$ and flow rate = 509 mL/min in all experiments.	122
Figure 4-8: Effect of jet flow rate and varying ferrous-ferric concentration on iron oxide hard agglomerate size, nucleation and particle details at (5) $[\text{OH}^-] = 1 \text{ M}$ and 509 mL/min and (6) $[\text{OH}^-] = 1 \text{ M}$ and 63 mL/min. $[\text{Fe}^{3+}] = 2[\text{Fe}^{2+}] = 0.36 \text{ M}$ in all experiments.....	123
Figure 5-1: Scale-up CIJR (a) dimensions and (b) configuration of pressure transducers.....	144
Figure 5-2: Effect of jet Reynolds number on energy dissipation rate. Based on total (mechanical) energy balance.....	145
Figure 5-3: Effect of jet momentum on energy dissipation rate	145
Figure 5-4: Effect of time of flight on energy dissipation rate.....	146
Figure 5-5: Effect of residence time on energy dissipation rate	146
Figure 5-6: Effect of jet Reynolds number on product yield at (a) $[\text{H}^+] = 0.0936 \text{ M}$, (b) $[\text{H}^+] = 0.1818 \text{ M}$ and $[\text{H}_2\text{BO}_3^-] = 0.1818 \text{ M}$ in all experiments.....	147
Figure 5-7: Effect of Damkoehler on product yield at (a) $[\text{H}^+] = 0.0936 \text{ M}$, (b) $[\text{H}^+] = 0.1818 \text{ M}$ and $[\text{H}_2\text{BO}_3^-] = 0.1818 \text{ M}$ in all experiments	148
Figure 5-8: Effect of energy dissipation on product yield at (a) $[\text{H}^+] = 0.0936 \text{ M}$ and (b) $[\text{H}^+] = 0.1818 \text{ M}$ and $[\text{H}_2\text{BO}_3^-] = 0.1818 \text{ M}$	149
Figure 5-9: Effect of jet momentum on product yield at $[\text{H}^+] = 0.1818 \text{ M}$ and $[\text{H}_2\text{BO}_3^-] = 0.1818 \text{ M}$	150
Figure 5-10: Effect of residence time on product yield at $[\text{H}^+] = 0.1818 \text{ M}$ and $[\text{H}_2\text{BO}_3^-] = 0.1818 \text{ M}$	150
Figure 5-11: Effect of time of flight on the product yield at varying hydrogen concentrations.....	151

Figure 5-12: Effect of reduced flow on normalized energy dissipation rate at varying jet Reynolds number in (a) original geometry (from Siddiqui et al., 2009) and (b) 2X scale-up geometry	152
Figure 5-13: Effect of reduced sulfuric acid flow on product yield at (a) $[H^+] = 0.0936$ M, (b) $[H^+] = 0.1818$ M and $[H_2BO_3^-] = 0.1818$ M in all experiments in 2X scale-up geometry	153
Figure 5-14: Effect of reduced sulfuric acid flow on product yield at (a) $[H^+] = 0.0936$ M, (b) $[H^+] = 0.1818$ M and $[H_2BO_3^-] = 0.1818$ M in all experiments in 4X scale-up geometry	154

List of Tables

Table 2-1: Reagent concentrations for iodide-iodate reaction	29
Table 2-2: Reagent concentrations for iron oxide precipitation reaction.....	29
Table 2-3: Time steps used for unsteady reactor simulations	29
Table 2-4: Energy dissipation rates in CIJR.....	30
Table 2-5: Comparison of mixing performance in CIJR and Stirred Tank.....	30
Table 3-1: Effect of flow rates and reactant concentrations on iron oxide mean agglomerate and primary particle sizes.....	66
Table 3-2: Reagent concentrations for iodide-iodate reaction	66
Table 3-3: Effect of stabilizers (added in situ) on iron oxide mean agglomerate and primary particle sizes. $[\text{Fe}^{2+}] = 0.18 \text{ M}$, $[\text{Fe}^{3+}] = 0.36 \text{ M}$ and $[\text{OH}^-] =$ 1.45 M and flow rate = 165 mL/min for all experiments.....	67
Table 3-4: Energy dissipation and Energy density in insitu sonication in CIJR..	67
Table 3-5: Effect of in situ sonication on iron oxide agglomerate and primary particle size with/out in-situ added stabilizer. $[\text{Fe}^{2+}] = 0.18 \text{ M}$, $[\text{Fe}^{3+}] = 0.36$ M , $[\text{OH}^-] = 1.45 \text{ M}$ and flow rate = 165 mL/min in all experiments.	68
Table 4-1: Turbulence collision (agglomeration) kernel.....	112
Table 4-2: Batchelor length, limiting length for Brownian agglomeration and estimated particle spacing within CIJR. * based on particle diffusivity. \$ based on mean or maximum energy dissipation.	112
Table 4-3: Effect of flow rate and reactant concentration on iron oxide mean agglomerate and primary particle sizes.....	112
Table 4-4: Mass transfer limited growth. Time required to grow nuclei to the observed primary particle size. $[\text{Fe}^{3+}] = 2[\text{Fe}^{2+}]$	113
Table 4-5: Time required to form a material bridge between colliding particles	114
Table 4-6: Effect of reactant concentration and jet flow rate on hard agglomerate size, estimated nucleus size, generation rate of nuclei, reactant concentration available for nucleic growth, number of moles available per nucleus for growth, fraction of available reactant used for diffusional growth, size of	

primary particle, number of primary particles sintered together in a hard agglomerate and generation rate of hard agglomerates.....	115
Table 5-1: Dimensions of the three sizes of CIJR.....	142
Table 5-2: Reagent concentrations for the iodide-iodate reaction	142
Table 5-3: Scale-up criterion.....	143

Nomenclature

Roman characters

a	chemical activity (M)
C, c	concentration (M)
C^*	critical concentration (M)
C_{Ao}	initial concentration limiting reagent (M)
C_{eq}	Equilibrium concentration at supersaturation = 1 (M)
C_g	feed concentration available for particle growth (M)
d_i	inlet jet diameter (m)
d_o	outlet jet diameter (m)
d_{cv}	diameter of control volume (m)
d_p^*	nucleus diameter (m)
$d_p (= d_i)$	primary particle diameter (m)
d_{HA}	hard agglomerate diameter (m)
Da	Damkoehler number
D_{AB}	molecular diffusivity (m^2/s)
D_c	jet separation in CIJR (m)
g	acceleration due to gravity (m/s^2)
G	growth rate (m/s)
ΔG	free energy associated with nucleation (J)
ΔG^*	free energy associated with critical/stable nucleus size (J)
ΔG_v	free energy associated with change in particle volume (J)
h_i	length of a section in CIJR (m)
i	stream number (unitless)
J_{ij}	collision frequency per unit volume ($m^{-3} s^{-1}$)
k	rate constant ($M^{-4} s^{-1}$)

k_B	Boltzmann constant (J/K)
k_n	n^{th} order rate constant ($\text{M}^{1-n} \text{s}^{-1}$)
K_{CIJR}	CIJR constant (unitless)
K_{sp}	solubility product (M^3)
ΔKE	rate of kinetic energy change (drop) across CIJR (W)
L_i	inlet tube length in CIJR (m)
m_i	mass component i (kg)
$\dot{m}_i (\dot{M}_i)$	mass flow rate component i (kg/s)
\dot{m}_g	product mass available for growth (mol)
m_{pp}	mass of each primary particle (g)
MW_i	molar mass component i (g/gmole)
n_i	moles component i (moles)
\dot{n}_i	molar flow rate component i (moles/s)
n_{pp}	primary particle generation rate (s^{-1})
n_{HA}	number of primary particles in a hard agglomerate (unitless)
N_g	product moles available for particle growth per nuclei (moles)
N_{HA}	agglomerate generation rate (s^{-1})
$\%N_g$	percentage of the available moles used for growth
p_i	hydrostatic pressure stream i (N/m^2)
P	available power for dissipation (W)
Δp	pressure change (drop) across CIJR (N/m^2)
Q_i	flow rate stream i (m^3/s)
r	reaction rate ($\text{M} \text{s}^{-1}$)
r_c	radius of hemispherical section in CIJR (m)
r	particle radius
r^*	particle radius (critical) (m)

R	theoretical radius of primary particles in CIJR when particles are in close packing (m)
Re	jet Reynolds number (unitless)
S	supersaturation (unitless)
SA	material bridge surface area (m ²)
Sh	Sherwood number (Unitless)
t	time (s)
t_f	time of flight (s)
T	temperature (K)
\bar{U}_i	mean square velocity deviation of the flux
V_{avg+}	region where dissipation drops from peak value to volume average value (m ³)
V_b	volume of the crystalline bridge (m ³)
V_i	jet velocity stream i (m/s)
V'_i	fluid velocity in control volume (m/s)
V_{max}	region where dissipation drops from peak value to 50% peak value (m ³)
V_{total}	reactor volume (m ³)
V_{CIJR}	reactor volume (m ³)
V_{LJR}	reactor volume (m ³)
x	distance (M)
Y	product yield in iodide-iodate reaction (unitless)
Y	product yield in iodide-iodate reaction (unitless)
z_i	potential head stream i (m)

Greek letters

ε_{max}	maximum turbulent energy dissipation at the impeller or at jet impingement point (W/kg)
$\bar{\varepsilon}$	average turbulent energy dissipation over the volume (W/kg)

λ_k	Kolmogorov length scale (m)
Δ	dimensionless jet separation in CIJR w.r.t. jet diameter ($= D_c/d_i$, unitless)
Γ	density of the adsorbed species (mol/m ²)
β	collision (agglomeration) frequency kernel (m ³ /s)
$\dot{\gamma}$	simple shear (s ⁻¹)
γ	interfacial tension (N/m)
∂	differential change in property (unitless)
$\bar{\rho}$	mixture fluid density (kg/m ³)
ρ_c	particle density (kg/m ³)
ρ_i	fluid density stream i (kg/m ³)
η_β	Batchelor length (m)
η_{HA}	measure of agglomeration efficiency (unitless)
μ	dynamic viscosity (kg/m-s)
μ_i	chemical potential (J/mole)
v_m	molecular volume (m ³)
v_i	kinematic viscosity stream i (m ² /s)
\bar{v}	mixture kinematic viscosity (m ² /s)
τ_{res}	residence time (s)
τ_m	mixing time (s)
τ_B	Batchelor time scale (s)
τ_g	diffusional growth time (s)
$\tau_R (= \tau_r)$	reaction/precipitation time (s)
τ_b	bridging/contact time (s)
τ_i	interaction time (s)

Chapter 1

Introduction

General background

Mixing is an important unit operation in chemical and pharmaceutical industries. It has the ability to affect the product yield and selectivity of liquid phase chemical reactions and product's physical and chemical properties in precipitation and reactive crystallization reactions. The stirred tank is a standard mixing geometry employed for chemical reactions and in general for all mixing-facilitated operations at lab and industrial scale. Despite improvements in impeller designs and feed addition strategies for industrial application over the last few decades, its success is often challenged by low volume-average energy-dissipation (a measure of mixing intensity), wide variation in dissipation across the mixing volume, mechanical moving parts and its batchwise operation. On the other hand, impinging jets with fast mixing, high dissipation (10-100x times higher than stirred tank) and continuous operation offer a wide industrial applicability for mixing sensitive reactions. Works by Midler (1994), Kirwan et al. (1996), Johnson et al. (2003), Schwarzer et al. (2004) and Marchisio et al. (2006) refer to the use of impinging jets to meet the high mixing requirements of fast chemical reactions. It is important to note that although slow chemical reactions can be successfully carried out in stirred tanks by increasing the residence time; impinging jets can only be used when the reaction time of the desired reaction is smaller than the reactor's residence time. This ensures completion of the reaction within the reactor and therefore high product yield and product selectivity.

Mixing in the CIJR has previously been characterized through chemical means (Johnson et al., 2003), but a very simple concept that has been overlooked in impinging jets – pressure drop and mechanical energy balance – is used in this work to estimate energy dissipation in the mixing volume. CFD is also used to support the estimations. The mixing effect on chemical reactions also needs to be explored and for that purpose two reaction systems – iodide-

iodate (homogeneous system) and iron oxide precipitation (heterogeneous system) are used. In the first, the mixing efficiency is tracked through product yield measurements while in the second reaction; the effect of mixing on precipitate particle size is investigated. Mixing facilitates a rapid build-up of local supersaturation that is discharged through precipitation of nuclei from the liquid phase. Mixing can thus have a significant effect on particle size and morphology. Microscopic images of the precipitate show that it is made up of smaller units here referred to in the text as primary particles. In the larger hard agglomerates primary particles are strongly bound together through hard chemical bridges. The primary particles are much bigger than the estimated nuclei diameter precipitated under high supersaturation conditions. Hard agglomerates are resistant to both fluid shearing and sonication effects. The goal of this thesis is to better understand the effect of mixing on particle agglomeration and to determine if it can be controlled? In order to control it, a thorough understanding of the competing processes like mixing, supersaturation generation, nucleation, particle growth, chemical bridge formation and aggregation is important. Additive types (surfactants and stabilizers), additive concentration, reaction pH, reagent concentrations, jet flow rates and sonication affect particle agglomeration and thus their effects need to be investigated. A section of this thesis addresses these issues. A largely experimental approach has been followed to answer the questions. A model based on the competing processes and the ensuing particle agglomeration is developed, and experimental evidence is used to explain the observed phenomena.

In industries where unbalance in flows and thus momentum may occur affecting mixing performance of CIJR, flow unbalance needs to be tested and tracked through energy dissipation and product yield experiments. Also despite the industrial scale production capacity of the small CIJR in a continuous operation; geometric scale-up of the geometry is desirable for greater production. Thus the effects of unequal jet momentum due to flow fluctuations on mixing efficiency also need to be quantified by tracking variations in energy dissipation and the product yield of iodide-iodate reaction in the original and scale-up CIJRs.

A comprehensive literature review has been done to support our work and is divided between various chapters.

Structure of this thesis

This thesis is based on four papers, either published, or submitted for review.

Chapter 2 explore the mixing characteristics of a Confined Impinging Jet Reactor. It considers the characterization of the CIJR over a wide range of jet flow rates (variation up to a factor of 50) by measuring the dissipation, the product yield of iodide-iodate reaction, and particle size from iron oxide precipitation reaction. Operational limits are evaluated by performing experiments at equal flow rates for all three-performance tests and unequal flow rates (upto a 30% difference) for the dissipation and the product yield. A series of pressure drop measurements and mechanical energy balance calculations are used to estimate the mean energy dissipation rate in the CIJR, and compared with the results of CFD simulations. The mixing-sensitive iodide-iodate reaction is used to study the micromixing performance of the CIJR at both balanced (equal momentum) and unequal flow (unequal momentum) conditions. The trends in the iodide-iodate yield results are compared with the energy dissipation results to draw conclusions about flow regimes, and the effect of turbulence on the reaction products. Finally, the iron oxide model system is used to probe the mixing performance of the CIJR for inorganic submicron and nanoparticle precipitation. Both iodide-iodate product yield and iron oxide precipitate particle size confirm the importance of mixing as a determining mechanism.

Chapter 3 discusses the effect of flow rate and feed concentration on iron oxide particle size. The idea is to successfully control agglomeration during intense mixing by identifying a suitable stabilizer, stabilizer concentration, stabilizer point of addition and sonication strategy (in-situ or post-reaction) for large-scale manufacture of submicron oxide particles. The iodide-iodate reaction is used to study mixing effects and to support the observed energy dissipation trends in the CIJR. CFD is used to predict any changes in dissipation associated with geometry modification (to accommodate sonic probe for in situ sonication).

Chapter 4 discusses the complex steps involved in a precipitation reaction: supersaturation generation initiated by mixing, nucleation, particle growth, interparticle growth and particle agglomeration. This whole sequence of events is simplified down to a 3-step mechanism – (i) mixing and its influence on supersaturation and nucleation, (ii) growth of nuclei to primary particles and (iii) agglomeration of primary particles to form hard agglomerates. From the literature, and the understanding drawn from mixing, nucleation theory, diffusional growth of particles under supersaturation, and the experimental evidence of agglomeration; one can infer that both mixing and reactant concentrations conditions have a significant effect on the agglomeration of primary particles and a deep inter-relationship exists between the associated processes. Agglomeration efficiency and shear (laminar and turbulent) are also important.

Chapter 5 considers the effect of scale-up of the CIJR on its mixing efficiency. The product yield of the iodide-iodate reaction and the energy dissipation are used to evaluate mixing efficiency under balanced flow and momentum conditions. Operational robustness is studied by studying variation in product yield and dissipation under unequal momentum conditions. Finally, a set of scaling parameters are compared to determine which ones can be successfully used to scale-up the CIJR and predict its micromixing performance. In Chapter 5, the scale-up limit where micromixing is adversely affected is determined. At this point, there is an unacceptable decrease in product yield and energy dissipation.

Chapter 6 wraps up this work with the major conclusions of the thesis and ideas for possible future work.

Literature cited

- Johnson, B.K., 2003, *Flash NanoPrecipitation of Organic Actives via Confined Micromixing and Block Copolymer Stabilization*, Ph.D. Thesis: Volume 1 and 2, Princeton University, USA.
- Johnson, B.K. and R.K. Prud'homme, 2003, *Chemical Processing and Micromixing in Confined Impinging Jets*, *AIChE Journal*, **49 (9)**, 2264-2282.
- Marchisio, D.L., L. Rivautella and A. Barreri, 2006, *Design and Scale-Up of Chemical Reactors for Nanoparticle Precipitation*, *AIChE Journal*, **52 (5)**, 1877-1887.
- Midler, M., E. Paul, E. Wittington, M. Futran, P. Liu, J. Hsu and S. Pan, 1994, *Crystallization Method to Improve Crystal Structure and Size*, US Patent 5,314,506.
- Schwarzer, H.C, and W. Peukert, 2004, *Combined Experimental/Numerical Study on the Precipitation of Nanoparticles*, *AIChE Journal*, **50 (12)**, 3234-3447.

Chapter 2

Characteristics of a Confined Impinging Jet Reactor: Energy Dissipation, Homogeneous and Heterogeneous Reaction Products, and Effect of Unequal Flow¹

Introduction

Chemical reactions are often carried out in stirred tanks. In many cases multiple reactions producing both desired and undesired products occur simultaneously. Stirred tanks have highly non-uniform mixing conditions and require careful feed addition strategies for successful operation (Bhattacharya, 2005; Bhattacharya and Kresta, 2004). In contrast, the two co-axial jets in a confined impinging jet reactor (CIJR) impinge head-on, generating a localized region of highly intense turbulent-energy dissipation. All of the feed to the confined impinging jet reactor must first visit the region of maximum dissipation, which allows much tighter control over mixing-sensitive reactions. The CIJR residence time is very small due to the high feed velocities and small reactor volume. This makes the CIJR attractive for cases where continuous production is needed and the product quality requirements are tight.

A number of mixing studies of the CIJR have been published over the last decade. Schwarzer and Peukert (2004) investigated barium sulfate nanoparticle precipitation both experimentally and computationally. Their CFD model accurately predicts the mean size of the precipitate nanoparticles. Mahajan and Kirwan (1996) characterized micromixing in impinging jets with a 2-step Bourne reaction (naphthol and diazosulfanic acid) as a function of hydrodynamics and mixing geometry, and used the organic compound Lovastatin as a ‘chemical probe’ to study mixing effects on the final particle size distribution. Quantitative measurements of the mixing time and the kinetic rate constant for Lovastatin nucleation were determined. Marchisio et al. (2006) studied submicron barium sulfate particle production, and specifically the effect of mixing on particle size.

¹ Ind. Eng. Chem. Res. (article in press)

The goal of their study was to develop a predictive CFD precipitation model to assist in the design and scale-up of precipitation reactors. Johnson and Prud'homme (2003) reviewed (Malguarnera and Suh, 1977; Tucler and Suh, 1978; Lee et al., 1980; Baldyga and Bourne, 1983; Sandell et al., 1985) and concluded that most previous researchers had studied mixing at low Reynolds number (50 to 600). The micromixing probes used in these studies were not sensitive enough to capture mixing effects at high Reynolds number and showed a plateau in mixing performance. Nguyen and Suh (1985) found somewhat different results, so Johnson and Prud'homme (2003) concluded that the micromixing studies were inconclusive and subsequently carried out a detailed micromixing study using the DMP reaction. This allowed prediction of mixing performance, product selectivity and scale-up criteria for the CIJR. Johnson and Prud'homme (2003) also studied mixing effects on formation of organic nanoparticles which are produced in a fast precipitation reaction. Liu and Fox (2006) have done detailed computational studies of micromixing with second order parallel DMP reaction in a CIJR.

In parallel, there is an ever-growing interest in the production of inorganic nanoparticles for new materials. The term 'nanoparticle' is used for particles less than 200nm but often it is loosely used to refer to particles as big as few hundred nanometers. Many synthesis methods, including thermal decomposition (Lu et al., 2007), chemical reduction (Lu et al., 2004), flame synthesis (Stark and Pratsinis, 2002), microemulsion (Lu and Schüth, 2007), hydrothermal (Lu and Schüth, 2007), and chemical precipitation (Lu and Schüth, 2007; Matijević, 1991; Jain et al., 2005; Lin et al., 2005; Beattie, 1989; Jolivet et al., 2000; Jotivet et al., 2002; Dong, 2002; Maity and Agrawal, 2007) have been proposed. Most of these synthesis methods require high temperature and controlled atmosphere conditions, whereas chemical precipitation proceeds at ambient conditions. Maity and Agrawal (2007) have argued that the precipitation route is preferable due to its experimental simplicity and its capability to make nanoparticles in large volumes. The CIJR, despite its small geometric dimensions, is capable of making several kgs/day of nanoparticles of mean size 200nm at ambient conditions via

the fast precipitation synthesis route. In a heterogeneous chemical precipitation system; however, mixing has a profound effect on particle size, particle size distribution, particle morphology and other properties (Schwarzer and Peukert, 2004). The size of precipitated particles is highly dependent on the mixing conditions during precipitation.

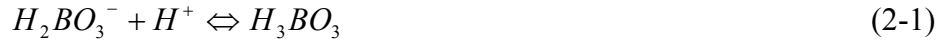
In this work the CIJR is characterized over a wide range of flow rates (50x variation) by measuring the dissipation, the yield of a homogeneous reaction, and the particle size resulting from a heterogeneous reaction. Operational limits are evaluated by performing experiments at equal flow rates for all three-performance tests and unequal flow rates (up to a 30% difference) for the dissipation and the product yield. A series of pressure drop measurements and mechanical energy balance calculations are used to estimate the mean energy dissipation rate in the CIJR, and compared with the results of CFD simulations. The mixing-sensitive reaction (iodide-iodate) is used to study the micromixing performance of the CIJR at both balanced and unequal flow conditions. The trends in the yield of iodide-iodate reactions are compared with the energy dissipation results to draw conclusions about flow regimes, and the effect of turbulence on the reaction products. Finally, iron oxide (Fe_3O_4) was chosen as a model system to probe the performance of the CIJR for inorganic nanoparticle precipitation. Iron oxide finds numerous applications in ceramics, catalysts and controlled pharmaceuticals-drug release (Lin et al, 2005; Goia and Matijević, 1998). While the interacting mechanisms in this last performance test are complex, the overall trends are informative and confirm the importance of mixing as a determining mechanism.

Iodide-Iodate reaction

The three-step competitive-parallel iodide-iodate model reaction system has been extensively used as a micromixing probe for comparing various mixing geometries and varying mixing conditions. Fournier et al. (1996), Assirelli et al. (2005 and 2008), Guichardon et al. (2000) and Monnier et al. (1999) studied mixing effects on product yield (Y) in stirred tanks. The iodide-iodate reaction is

economical to run and has fewer waste disposal and safety issues associated with it than the Bourne (first, second and third) reactions (Bhattacharya, 2005; Bhattacharya and Kresta, 2004) and the DMP (fourth Bourne) reaction (Johnson, 2003).

The neutralization reaction in the iodide-iodate reaction given in reaction (2-1) is fast and desired.



$H_2BO_3^-$ ions are obtained from the coexisting H_3BO_3 and NaOH in the reaction mixture, which form a buffer. The slower and parallel redox reaction (Dushman reaction) forming byproduct (I_2) is:



The byproduct iodine (I_2) reacts further to form triiodide ions (I_3^-).



Iodine (I_2) and triiodide (I_3^-) are the byproducts. The triiodide concentration in the product solution is measured directly using a spectrophotometer and the iodine concentration is determined by mole balance.

The reaction rate for the slower reaction is expressed (Guichardon, 2000) as:

$$r = k[I^-]^2[IO_3^-][H^+]^2 \quad (2-4)$$

Guichardon et al. (2000) reported k to be $1.3 \times 10^9 \text{ M}^{-4} \text{ s}^{-1}$ at 25°C . According to these kinetics, the first reaction is much faster. Under perfect mixing conditions all of the H^+ (from H_2SO_4) reacts in the first (and faster) reaction, but under imperfect mixing conditions, local high concentrations of H^+ occur leading to formation of the undesired byproducts. The ratio of the rate constants (slow to fast reaction) determines the product selectivity. The effect of ionic strength on the rate constant (k) for the slow reaction; however, was neglected in this analysis. A change in k would affect the 'theoretical' yield, and thus shift any further analysis. An increase in ionic strength of 1-1.1 M causes a 11% drop in rate (Guichardon, 2000). Bourne (2008) has discussed many of the shortcomings

of the reported kinetics; concluding that the quantitative conclusions must be considered carefully, but the qualitative trends are correct.

Historically the segregation index (X_s) has been used to quantify micromixing. X_s is given by the ratio of the experimental product yield to the yield when the reagents are in completely segregated state, however; in this study micromixing is quantified by product yield (Y). The product yield (Y) depends on the moles of limiting reagent (H^+) consumed in forming products:

$$Y = 1 - \frac{\text{moles of } H^+ \text{ consumed in byproducts}}{\text{total moles of } H^+ \text{ added to the system}} \quad (2-5)$$

Bourne (2008) has recently reported that although the iodide-iodate reaction gives qualitatively consistent results, it may not be quantitative. Quantitative results require that the kinetics of all the reactions be fully known under the given mixing conditions. Bourne (2008), and Guichardon et al. (2000) reviewed the reaction rate expressions (Wronka and Banas, 1965; Abel and Hilferding, 1928; Abel and Stadler, 1926; Schildcrout and Furtunato, 1975 and Barton et al., 1975) and showed that the reaction rate expressions for the slower iodine-formation step lack agreement. The difference in the published models is due to the complexity of the iodine-formation reaction (Bourne, 2008). Bourne (2008) points out that the discrepancy in the models could also be due to the lack of modern analytical techniques, and variations in the reactant concentrations, ionic strengths, buffers and anions used by different researchers. Guichardon et al. (2000) and Bourne (2008) reported that the rate constant of the slower reaction is strongly affected by the ionic strength due to the many elementary ionic processes involved in the reaction mechanism and also noted that the dissociation equilibrium of the acid (source of H^+) needs to be considered in kinetic modeling.

Assirelli et al. (2008) used the kinetic model for the Dushman reaction as proposed by Guichardon et al. (2000). Although a good qualitative estimate of $\epsilon_{\text{ensemble, max}} / \epsilon_{\text{avg}}$ was obtained for mixing in a stirred tank with a feed pipe at the impeller, the values were higher than those obtained from PIV and LDV studies.

Assirelli (2008) concluded that the discrepancy might be due to either weak kinetic data or the mixing model.

Ehrfeld et al. (1999) studied mixing using a 2-step competing iodine formation reaction in micro-channels. He argued that byproduct formation could occur due to mixing quality, concentration differences due to different stream flows, and/or long time delays between mixing and absorbance measurement that allow the slower reaction to proceed even after mixing is complete. He concluded that the iodine reaction provides good comparative data of mixing quality in spite of these limitations.

Estimation of energy dissipation rate

The energy added to the CIJR is dissipated at the smallest length scales and determines the mixing intensity, or the mixing rate. Zhou and Kresta (1996) argued that as direct measurements of energy dissipation (local and average) are difficult, alternative approaches need to be adopted. To date, the energy dissipation in a CIJR has been estimated through computational models (Gavi et al., 2007) and through micromixing experiments (Johnson, 2003). Johnson (2003) characterized micromixing in CIJR with a mixing sensitive competitive DMP reaction but stopped short of estimating energy dissipation. First, his results are extended to give an estimate of the rate of dissipation of turbulent kinetic energy per unit mass, or the dissipation. Second, a simple but effective estimate of the energy dissipation rate through pressure drop measurements and a mechanical energy balance is proposed. This follows work by Zhou and Kresta (1996) who estimated the average energy dissipation in the impeller region by integrating local energy dissipation over the impeller control volume and found that it fell within 6% of the estimate from the mechanical energy balance. Finally, CFD simulations are performed and the average dissipation at several time steps is compared to the first two methods.

Micromixing reaction probe

The energy dissipation rate is an indicator of the degree of mixing achieved in a mixer. The energy available for dissipation can be estimated by doing a

macroscopic mechanical energy balance over the CIJR, considering the potential energy, kinetic energy and pressure energy. In a flow system, the sum of the changes in each of these together determines the energy dissipated due to friction and shear. This loss in energy is the energy dissipated at the smallest length-scales in the fluid.

Mahajan and Kirwan (1996) assumed that the energy available for dissipation came from an inelastic collision (impingement angle = 160°) of the inlet jets and thus the kinetic energy of the exiting fluid was assumed to be zero. Johnson and Prud'homme (2003) on the other hand assumed that the jet collision (impingement angle = 180°) was elastic and neglected the exit kinetic energy. Johnson (2003) argued that since the mixing chamber diameter was large (4.76 mm) as compared to the inlet jets (1 mm), the exit velocity was small enough to be neglected. In this case, the velocity of the fluid exiting the mixer would not affect the CIJR mixing performance and would only contribute to an increase in pressure drop across the mixer. According to Johnson (2003) the power (P) available for dissipation is proportional to the net kinetic energy leaving a meso-volume at the impingement point in Figure 2-1.

$$P \propto \frac{\dot{m}_1 V_1^2}{2} + \frac{\dot{m}_2 V_2^2}{2} - \frac{\dot{m}_3 V_3'^2}{2} \quad (2-6)$$

However, as V_3' is found to be very small for $d_{cv} \geq 2d_1$, it was neglected in comparison to V_1 and V_2 . Thus the power available for dissipation is P_{\max} :

$$P_{\max} \propto \frac{\dot{m}_1 V_1^2}{2} + \frac{\dot{m}_2 V_2^2}{2} \quad (2-7)$$

when the flows are balanced, their momentums are equal:

$$\dot{m}_1 V_1 = \dot{m}_2 V_2 \quad (2-8)$$

Thus the average energy dissipation rate in CIJR is defined as:

$$\bar{\varepsilon}_{\max} = \frac{P_{\max}}{\rho V_{CIJR}} \quad (2-9)$$

Also the time required to mix to the Kolmogorov length scale (λ_k) by considering half the slab thickness and identical boundary condition in the other half is:

$$\tau_m (= \tau_B) \propto \frac{(0.5\lambda_k)^2}{\nu} \quad (2-10)$$

and

$$\lambda_k = \left(\frac{\nu^3}{\bar{\varepsilon}_{\max}} \right)^{1/4} \quad (2-11)$$

Substituting equations (2-7) and (2-8) in equation (2-9), and back substituting (2-9) and (2-11) in equation (2-10), Johnson and Prud'homme (2003) obtained:

$$\tau_m = K_{CLJR} \frac{\nu^{1/2} \Delta^2 d_1^{1/2}}{2V_1^{3/2}} \frac{1}{\left[\left(\frac{\rho_1}{\rho_3} \right)^{1/2} \right]} \frac{1}{\left[\left(1 + \frac{\dot{m}_1}{\dot{m}_2} \right)^{1/2} \right]} \quad (2-12)$$

Johnson and Prud'homme (2003) used the mixing-sensitive DMP reaction as a micromixing probe to determine K_{CLJR} for various mixer dimensions. In the limit when the mixing time (τ_m) is of the order of the residence time (τ_{res}), τ_m becomes independent of the mixer dimensions and K_{CLJR} was found to be 1470. Johnson and Prud'homme (2003) stopped short of estimating the energy dissipation rate, which is found by substituting (2-11) in (2-10):

$$\tau_m = K_{CLJR} \frac{1}{4} \left(\frac{\nu}{\bar{\varepsilon}_{\max}} \right)^{1/2} \quad (2-13)$$

An expression for energy dissipation rate is thus found by equating (2-12) and (2-13):

$$\bar{\varepsilon}_{\max} = \frac{0.25V_1^3}{\Delta^3 d_1} \left(\frac{\rho_1}{\rho_3} \right) \left(1 + \frac{\dot{m}_1}{\dot{m}_2} \right) \quad (2-14)$$

The approaches adopted by Mahajan and Kirwan (1996) and Johnson and Prud'homme (2003) to estimate energy dissipation rate have certain limitations - they neglect the kinetic energy of the exit fluid and the pressure drop associated with friction at the mixer wall, which could significantly contribute to energy

dissipation over the mixing volume. A second approach to estimating the energy dissipation rate is considered in the following section.

Mechanical energy balance

A mechanical energy balance is applied over the inlet and the exit planes in Figure 2-2 using the pressure drop and fluid exit kinetic energy to determine the energy dissipation rate in the CIJR control volume.

$$\sum_{i=1}^2 (p_i - p_3) + \sum_{i=1}^2 \left(\frac{\rho_i V_i^2}{2} - \frac{\rho_3 V_3^2}{2} \right) + \sum_{i=1}^2 (\rho_i g z_i - \rho_3 g z_3) = \frac{P}{Q} \quad (2-15)$$

The pressure drop takes into account frictional and shear losses due to the fluid flow in CIJR (Schwarzer and Peukert, 2004). For balanced flows, the inlet flow rates are equal ($Q_1 = Q_2$) and the outflow is the sum of the inflows ($2Q_1$). The pressure drop is determined by measuring the hydrostatic pressures at the CIJR inlets and outlet and taking an average:

$$\Delta p = \frac{(p_1 - p_3) + (p_2 - p_3)}{2} \quad (2-16)$$

The energy change associated with the pressure drop is calculated from:

$$\Delta \text{ pressure energy} = (2Q_1) \Delta p \quad (2-17)$$

The mean kinetic energy (*KE*) contribution to the mechanical energy balance incorporates the mean kinetic energy associated with the fluid exiting the CIJR. Here the mass outflow (m_3) is the sum of mass inflows (m_1 and m_2). In this work velocity time fluctuations were calculated using the profiles reported by Munoz (2004) for turbulent pipe flow. The turbulent kinetic energy (TKE) contribution was less than 0.25% of the mean. The mean kinetic energy is used to estimate the mean kinetic energy dissipation in the mixing volume.

$$\Delta KE = \frac{\dot{m}_1 V_1^2}{2} + \frac{\dot{m}_2 V_2^2}{2} - \frac{\dot{m}_3 V_3^2}{2} \quad (2-18)$$

The change in potential energy from the inlets to the exit is very small and can be neglected. The energy dissipation rate is thus estimated from the following expressions:

$$\bar{\varepsilon}_{pressure} = \frac{2Q_1 \Delta p}{\rho V_{CIJR}} \quad (2-19)$$

$$\bar{\varepsilon}_{tot} = \frac{2Q_1 \Delta p + \Delta KE}{\rho V_{CIJR}} \quad (2-20)$$

Thus the rate of dissipation of turbulent kinetic energy (TKE) per unit mass in CIJR can be approximated by the total mechanical energy change over the mixing volume.

Experimental setup and operating conditions

The dimensions of the CIJR are given in Figure 2-3(a) with the fully constructed CIJR shown in Figure 2-3(b). Figure 2-3(c) shows the location of the pressure transducers (Omegadyne, PX600, 0-200 psig miniature flush diaphragm transducer). The pressure taps are located within 1mm of the inlets and the outlet to capture the pressure drop across the mixing volume and avoid any pressure drop associated with the inlet and outlet pipes. The pressure lines are filled with static test fluid (RO water) prior to experiments. All three transducers are connected to a common data-logging system and the data is recorded for two minutes for each experimental run. For the reaction experiments the CIJR with no pressure ports was used.

Constant pulse-free flows to the CIJR were provided by micropump-head (Series GB, external gear pump, max flow rate 4L/min), which were fitted onto pump drives (MCP-Z standard, IDEX corporation). Each of the micropumps was calibrated by volumetric and mass flow methods for a range of flow rates from 20 mL/min to 509 mL/min. Flow visualization with colored dye was used to monitor the stability of the flow in the CIJR. No pulsations were observed in the jet feeds and the jets met in the middle of CIJR volume under balanced flow conditions. No pulsations were either observed under unequal flow and unequal

momentum conditions. The jet impingement point remained stationary between the jet inlets in all cases.

Iodide-Iodate reaction

Reagent solutions were prepared using the procedure given by Guichardon and Falk (2000) with changes in solution concentrations to suit the equal volumetric flow rate conditions in CIJR. Reverse Osmosis (RO) water was used in preparing all reagent solutions. Reagents for the iodide-iodate reaction were prepared using certified grade potassium iodate, potassium iodide, sodium hydroxide, boric acid powder and sulfuric acid 10N solution. Solutions of potassium iodide (KI) and potassium iodate (KIO_3) were prepared in deoxygenated water to prevent any iodine formation by oxidation of iodide ions prior to the chemical reaction. The RO water was deoxygenated by bubbling nitrogen gas through it for 20 minutes. To prevent formation of iodine and coexistence of the iodide and iodate ions in the solution, a specific addition sequence of reagent solutions was followed. The boric acid and sodium hydroxide solutions were first well mixed to make a buffer solution. The KI and KIO_3 solutions were then added in sequence. The solution concentrations are given in Table 2-1. These concentrations are the reagent concentrations in the jet streams. For the equal flow case, the reagents were fed in stoichiometric proportion and the mean concentration in the CIJR prior to reaction would be half of the inlet concentrations. For unequal flows the concentration in the reactor and the ratio of reagents depends on the flow imbalance.

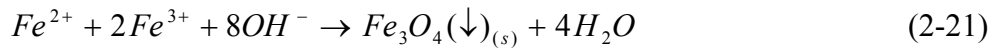
Upon mixing and the reaction, samples were collected at the CIJR outlet. The pH of each sample was measured and the temperature was recorded. The 50 mL sample was subjected to UV absorbance measurements at a wavelength of 352nm using a light probe (7 mm path length) connected via a fiber-optics cable to UV-visible spectrophotometer (Ocean Optics, model SQ 2000). To calibrate the spectrophotometer a series of absorbance measurements were carried out on standard triiodide solutions. Guichardon et al. (2000) reviewed the extinction coefficient values (Custer and Natelson, 1949; Herbo and Sigallia, 1957; Palmer

et al., 1984) which range from 2575 to 2590 (m²/mol), and measured an extinction coefficient of 2395.9 m²/mol. Hirshfeld (2006) established that the extinction coefficient varies from 1894 m²/mol to 2205 m²/mol when the water source is changed from reverse-osmosis to de-ionized ultra-filtered water. The extinction coefficient is also sensitive to the fibre optic characteristics of each probe (Zhao, 2007), varying between the four probes, but providing very consistent results for the single probe used throughout this study. The extinction coefficient measured for reverse-osmosis water with the probe in this work was 1914.8 m²/mol.

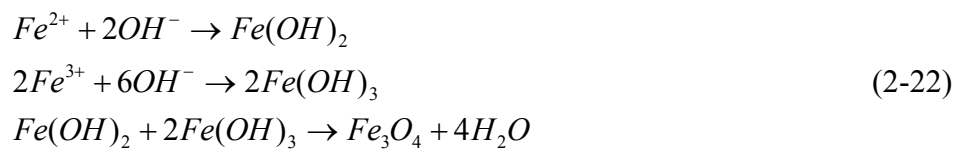
To determine the repeatability of the iodide-iodate reaction experiments, a series of 12 flow rates was repeated three times. The results are shown in Figure 2-4. The standard deviation was less than 1.03×10^{-4} over the full range of flow rates. In subsequent figures, error bars are not plotted because they are of roughly the same size as the symbols on the graphs.

Iron oxide reaction

Co-precipitation experiments with iron oxide were carried out at room temperature. The temperature of the inlet and outlet streams was measured and the ΔT was negligible. The crystalline iron oxide is obtained from co-precipitation of ferrous-ferric hydroxides and removal of water molecules from the amorphous hydroxides. Iron oxide precipitates according to the following overall reaction (Lin et al., 2005; Maity and Agrawal, 2007):



Mixing initiates a complex process of crystal precipitation. Oxide formation is a complex reaction process during which the hydroxides react and lose water, followed by a condensation reaction within newly formed solid phase at high pH $\sim 12-13$ (Leiser, 1969). The intermediate steps are simplified as:



Reagent solutions were prepared using RO water and certified quality ferrous chloride, ferric chloride and sodium hydroxide. The solution concentrations are listed in Table 2-2.

The product solution collected from the CIJR was a suspension of precipitate, excess reagents and reaction products. It was washed multiple times with reverse-osmosis (R.O.) water and decanted prior to particle sizing measurements. The decanted sample was sonicated for 15 minutes and diluted to $\leq 1\%$ v/v (particle sizer specific recommendation) with RO water prior to particle size measurements in DLS Particle Size Analyzer (Brookhaven, model: ZetaPlus). The sample in the vial was re-sonicated for a minute before each size measurement to disperse any loose aggregates. The Brookhaven ZetaPlus measures the effective diameter (d_{65}) of the particles in suspension. d_{65} is the intensity weighted average diameter or the hydrodynamic diameter. Small polydispersity values (~ 0.005) were obtained i.e. the particles were monodisperse. Particle sizing on each sample was repeated five times to ensure consistency in the particle size and polydispersity measurements. The standard deviation varied between 120 nm and 15 nm over particle size measurements ranging from 1.5 micron to 200 nm over the range of flow rates investigated. Zeta potential measurements on the particles in suspension are often reported, but haven't been considered in this study.

To confirm that the precipitate was iron oxide, EDX analysis from TEM and SEM was carried out. It was confirmed that only Fe and O were present. The black precipitate settled rapidly under a magnetic field and also had a particle morphology which matches that of iron oxide (Maity and Agrawal, 2007; Mikhaylova et al., 2004). Selected area diffraction patterns (SAED) obtained from TEM confirmed the presence of iron oxide, but could not conclusively distinguish between the various phases of Fe_2O_3 and Fe_3O_4 . Maity and Agrawal (2007) did an extensive characterization of the precipitate obtained from this co-precipitation technique and confirmed that the precipitate was largely $\gamma\text{-Fe}_2\text{O}_3$, with a small amount of $\epsilon\text{-Fe}_2\text{O}_3$ and Fe_3O_4 due to the rapid oxidative tendency of

Fe₃O₄. This is contrary to the widely held assumption that the precipitate is predominately Fe₃O₄ (Maity and Agrawal, 2007).

CFD simulations

CFD simulations of the confined impinging jet reactor were performed using the commercial software Fluent 6.2.16. Since the kinetics of nanoparticle production is only partially known, only the flow field was simulated. The simulation results were compared with the dissipation rate data, and an injection of passive scalar into one inlet tube was used to determine residence time distributions for a range of flow rates.

The reactor geometry and computational grid were generated using the Gambit 2.2.30. The reactor was modeled by including full length of the inlet pipes in order to get stabilized inlet velocity profiles at the entrance of the reactor chamber and to allow for potential pressure fluctuations or backflow. The geometry was split into multiple connected volumes that allowed it to be meshed by hexahedral cells. The computational grid was refined near the impingement plane of the reactor and boundary layers were used along its walls. The resulting grid consisted of 961938 hexahedral cells. The computational grid used was originally created to perform LES simulations, which were successfully done, but were too time consuming to run for a wider range of flow rates. Instead RANS simulations were used to study flow-field in CIJR.

Four inlet flow rates were simulated: 70 ml/min, 165 ml/min, 300 ml/min and 500 ml/min. Water with a density of 998.2 kg/m³ and a viscosity of 1×10⁻³ Pa-s was used as the working fluid. The standard *k-ε* model was used to model turbulence. No slip boundary conditions were used for all reactor walls, constant inlet velocities were specified at both reactor inlets, and zero gauge pressure was used at the outlet. Second order discretization, SIMPLE pressure-velocity coupling algorithm and a segregated solver were used for the solution. Steady-state flow simulations were performed first but they did not converge because the flow inside the reactor is unsteady, as was observed in the dye visualization experiments. The partially converged flow fields were used to

initialize unsteady-state calculations. The LES turbulence model would be a good choice to model the evolution of time-dependent eddies in the flow field but was found to be too time-consuming. Instead, the unsteady $k-\varepsilon$ turbulence model was used. The time steps used for the unsteady simulations are summarized in Table 2-3. With these settings, all normalized residuals fell to less than 1×10^{-6} . The simulated flow fields and the dye experiments confirmed that the flow field oscillated at high flow rates and was steadier at low flowrates. At low flowrates, steady flow field is expected.

The calculated unsteady flow field animations revealed periodic flapping of the impinging jets, especially for flow rates of 300 ml/min and higher, which confirmed experimental observations. For lower flow rates, the impingement plane was almost perfectly stable, located in the middle of the jets. The turbulence kinetic energy dissipation rate profiles were extracted from all four simulations at a time where the impingement plane was in the middle to allow for better comparison of the flow rates. The average energy dissipation rates in the reactor chamber were calculated by finding an average of the volume averaged values reported by Fluent at three impingement plane (and time step) positions (left, middle and right).

Results

The results are divided into two parts. In the first part, the mixing in the CIJR is characterized for balanced flow and equal momentum. In the second part, the robustness of the CIJR under unbalanced flow conditions is investigated. The balanced flow characterization is done using three performance measures. The first measure is estimates of the energy dissipation rate from pressure drop, a mechanical energy balance, micromixing and CFD. The second measure is the effect of flow rate on the product yield of the mixing-sensitive homogeneous iodide-iodate reaction. The third and final measure is the effect of flow rate on the heterogeneous iron oxide precipitation reaction. In the second part of the results, the effect of unequal flow rates on the energy dissipation rate and on the product yield of the iodide-iodide reaction is investigated.

Balanced Flow, Equal Momentum

Turbulence and Flow

Figure 2-5(a) shows the effect of flow rate on the average energy dissipation for four different methods: pressure drop, total energy balance, micromixing probe and CFD simulations. The results are in very good agreement. Energy dissipation rates vary from 20 W/kg to 6800 W/kg for flow rates from 10-500 mL/min. This is much larger than the mean energy dissipation rate in a stirred tank, which lies between 0.1 W/kg and 100 W/kg. In the CIJR both the mean kinetic energy and the pressure drop associated with jets change significantly with flow rate and thus incorporating the kinetic energy loss in the energy dissipation calculations becomes significant for flow rates higher than of 165 mL/min. This is equivalent to a Reynolds number ($Re = 3500$) based on the diameter and velocity in one inlet jet. Because the range of dissipation rates is so large, the low flow rates end of the figure has been expanded and is shown in Figure 2-5(b). The function has a smooth exponential rise; with the dissipation rising to 50W/kg by a flow rate of roughly 75 mL/min. Table 2-4 compares the average dissipation from experimental measurements and CFD. The computed values are volume averaged, and then averaged over 1 and 3 time steps to capture different positions of the oscillating impingement plane. There is no apparent effect of the position of the impingement plane on the average dissipation.

Figure 2-6(a) and (b) show profiles of the local energy dissipation rates along the axial and inlet centerlines in the CIJR taken from the CFD simulations at 4 flow rates. Note that a log scale is used in both figures to capture the wide range of flow rates simulated and resulting wide range of dissipation rates. High dissipation rates are observed in regions close to the impingement point in each direction. The local dissipation decays rapidly away from the impingement point, rising again in the cone, but only to less than 10% of the peak values.

The inhomogeneity of turbulence in the CIJR is compared to the inhomogeneity in a stirred tank in Table 2-5. Two measures are used: the fraction of the vessel volume where the dissipation is at a maximum, and the ratio of the maximum dissipation to the average dissipation (the power dissipated

per mass). Three volumes are defined: first, the impeller volume, which is the basis for a number of energy balances and scaling rules in stirred tanks; second, the volume of the maximum dissipation, which is the region around the point of maximum dissipation where the dissipation decays away to 50% of the peak value; and third, the volume of the angle resolved volume of maximum dissipation in the trailing vortices behind an impeller. For homogeneous turbulence, the maximum dissipation is equal to the mean and fills 100% of the vessel. Both cases here are far from the ideal. Comparing the CIJR first with the impeller volume in a stirred tank, and then with the conditions in a trailing vortex, the ratio of the maximum local dissipation to the mean is roughly the same (40 for the CIJR, 50 for the stirred tank) and the impeller volume in a stirred tank covers more than twice the volume of the maximum dissipation volume in the CIJR. The maximum dissipation volume in the impeller discharge volume (Zhou and Kresta, 1996) is slightly smaller than the maximum dissipation volume in the CIJR.

The crucial difference between the two vessels is that all of the feed to the CIJR must pass through the maximum dissipation region within a very short time of entering the reactor, while the progress of feed from the surface of a stirred tank to the impeller region and/or the sweet spot in the discharge flow is less well defined. The situation is much worse for cases where the feed must reach the core of the trailing vortex (roughly 500x the average dissipation, but in a tiny volume which is only 0.07% of the tank volume). The odds of a fluid particle passing through this moving volume is very small indeed. Therefore, if these very high levels of dissipation are required, they are more easily achieved at quite moderate flow rates in the CIJR, with the added assurance that all of the feed will visit the maximum dissipation region within milliseconds of entering the reactor. The last point to consider in Table 2-5 is that the local dissipation in a stirred tank certainly decays to the average power per mass within two impeller volumes ($V_{\text{avg}+} \cong 1.3\%$ of the tank volume), while the simulations suggest that values higher than the mean are found over a much larger fraction of the CIJR.

At low flow rates, up to 30% of the CIJR has dissipation higher than the mean, but as the flow rate increases, this volume fraction shrinks from 30% to 7.5%.

The effect of flow rate on the stability of the CIJR flow field is illustrated in Figure 2-7. At the lowest flow rate, the velocity field is very stable, and the core velocity in the jet completely decays before the jets impinge (Figure 2-7a). At the highest flow rate, the oscillations of the impingement plane are evident, and the core velocity in the jet persists almost to the point of impingement.

Figure 2-8 shows the residence time distribution (RTD) in the CIJR at various flow rates. The CIJR shares characteristics of both a plug flow reactor (PFR – delta function appearing at the mean residence time in the vessel) and a continuous stirred tank reactor (CSTR – initial rise followed by exponential decay). As the flow rate increases, the RTD approaches plug flow with a very narrow distribution, but at low flow rates, the distribution is much broader. There is a lag time that increases as the flow rate drops: the fluid passes first through the impingement plane spreading out through the upper hemisphere and the upper part of the cylinder before passing down through the lower part of the cylindrical volume and exiting via the cone. It appears that at low flow rates, the CIJR is partially backmixed, but at higher flow rates it acts primarily as a plug flow device with a very high local energy dissipation.

Product yield in iodide-iodate reaction

Figure 2-9 shows the effect of jet flow rate on product yield for the homogeneous iodide-iodate reaction at varying $[H^+]$ concentrations. The trends are very consistent and it is evident that the product yield increases with an increase in flow rate at all reagent concentrations. The effect of flow rate on product yield is greatest at the higher concentrations. Evidently the effect of flowrate on product yield decreases beyond flow rate of 165 ml/min. Flow is understood to turn fully turbulent past the 300 mL/min flow rate limit. For concentrations < 0.1 M, the solutions are dilute and the effect of concentration disappears. When carried out in a stirred tank, the same reaction has a yield

closer to 90% (Guichardon and Falk, 2000), demonstrating the high mixing intensity present in the CIJR.

Particle size in iron oxide precipitation reaction

Figure 2-10 shows the effect of flow rate and feed concentration on iron oxide particle size. At all feed concentrations, an increase in jet flow rate sees a decrease in particle size. As expected, the effect of flow rate and mixing intensity is larger at higher concentrations. At ferrous and ferric concentrations of 0.18 M and 0.36 M respectively, the particle size decreases from 600 nm to 300 nm when flow rate is doubled from 165 mL/min to 300 mL/min. The effect of flow rate on particle size is very small at flow rates of 300 mL/min and above, as was also the case for the homogeneous reaction. Above flow rates of 300 mL/min mixing is understood to be faster than the particle nucleation, growth and agglomeration rate and hence the former has negligible influence on the final agglomerate size. Gavi (2009) carried out micro-PIV experiments over CIJR and reported that the flow in CIJR turns fully turbulent at around 100 mL/min.

Both precipitation kinetics and turbulence are understood to affect the final particle size. The mechanisms of nucleation, growth, stabilization and agglomeration interact with the mixing conditions to determine the final agglomerate size. This has been discussed in detail by Siddiqui et al. (2009). Under very high supersaturation conditions (as in this case), nucleation and particle growth rates may compete together for supersaturation, limiting the supersaturation available for building material bridges between the colliding particles.

Unequal Flow

Normalized energy dissipation rate

Figure 2-11(a) shows the effect of unequal flow on the average dissipation in a CIJR. All of the dissipation rates have been normalized with respect to the balanced flow condition. At flow rate of 100 mL/min ($Re = 2100$) the dissipation rate drops sharply to about 40% of its initial value as the difference in flow rate

increases. The drop in dissipation stabilizes at flow rate of 165 mL/min and above. This indicates a transition to turbulent flow in CIJR. At flow rates of 200 mL/min and above, 84% of the perfectly balanced average dissipation is retained all the way to a 30% difference between the two inlet flows. This is highlighted in Figure 2-11(b), where only the higher flow rates are shown.

Product yield in Iodide-Iodate reaction

The effect of unequal flowrate on the homogeneous reaction is tested in four sets of experiments. First, the limiting reagent (sulfuric acid) flow is reduced at two concentrations, one which showed mixing sensitive behavior under balanced flow conditions, and the other which was dilute and showed almost no sensitivity to mixing. Then the experiments are repeated, at the same two sulfuric acid concentrations, but with reduced flow of the buffer stream containing the excess reagent and pH buffering solution.

Figure 2-12(a) shows the effect of reduction in limiting reagent flow at the dilute condition. At flow rates above 40 mL/min, an imbalance in flow has a negligible effect on product yield. At low flow rates (30 and 40 mL/min) a drop in product yield is observed at 10% reduction in sulfuric acid flow rate. A further reduction in flow rate has an insignificant effect on product yield. The dilute case remains insensitive to changes in the mixing conditions. Figure 2-12(b) shows the effect of reduced sulfuric acid flow at the high concentration condition. Lower product yields are obtained at the high concentration condition at all flow rates. The product yield remains almost constant up to a 30% reduction in flow, but at higher concentration there is more variability in product yield. The lowest yields are all at the lowest flow rate, and the highest yields are all at the highest flow rates, but again the performance is surprisingly stable.

Figure 2-13 shows the effect of reduced buffer stream flow. Figure 2-13(a) shows the dilute condition, and Figure 2-13(b) shows the high concentration case. With a drop in buffer stream flow rate the $[\text{H}_2\text{BO}_3^-]$ in the CIJR decreases, while the $[\text{H}^+]$ increases slightly due to the smaller total flow. An increase in $[\text{H}^+]$ decreases product yield. At low flow rates the product yield is constant only until

a 10% difference in flow; at higher flow rates (88 mL/min and over) the product yield remains constant up to a 30% difference. Once again, a bigger influence of unequal flow is noted at low flow rates (63 mL/min and below). These results agree with the results in Figure 2-12. Figure 2-13(b) shows the effect of reduced buffer stream flow on product yield at high acid concentration. Comparison of Figure 2-13(a) and (b) confirms that a lower product yield is obtained at higher $[H^+]$, regardless of flow rate. With a drop in buffer stream flow, $[H_2BO_3^-]$, at high $[H^+]$, the reaction pH drops, making the solution more acidic. This has an insignificant effect on product yield until 10% reduction in the buffer stream. Beyond 10%, the pH drops significantly, supporting I_2 formation and dropping the yield significantly. At high concentrations, the effects of mixing are more evident, but the effect of imbalanced flow is surprisingly small as long as the required reaction stoichiometry and pH are respected. There is also a high variability in the yield beyond 10% reduction in buffer solution flow, suggesting an interaction of less stable mixing, and unstable reaction stoichiometry.

The fluids used for the experiments reported in Figure 2-11, Figure 2-12, and Figure 2-13 were either pure water or dilute solutions with nearly equal densities. In many industrial cases, the two solutions would have quite different densities. Therefore even if the flowrates are equal the stream momenta could be different. While a difference in fluid density can have additional effects due to buoyancy, the results in this work indicate that a difference in momentum or volumetric flowrate between the two inlet streams of up to 30% will not affect the performance of the CIJR.

Conclusions

Mixing efficiency of the CIJR has been characterized under both equal and unequal jet flow conditions. The CIJR can be successfully operated under a wide range of flow rates (10 to 500 mL/min). The flow is turbulent above 165 mL/min ($Re = 3500$) and fully turbulent above a flow rate of 300 mL/min ($Re = 6600$). CFD simulations show that the impingement plane is stable at low flow rates but oscillates rapidly at high flow rates. The oscillation frequency is not quantified in

this work. RTD plots, also from CFD simulations, show that the CIJR resembles a PFR at high flow rates and approaches a CSTR with dead volume and large dispersion at low flow rates.

Four methods for estimating energy dissipation were compared and the estimated values show very good agreement over the full range of flow rates. The average energy dissipation varies from 20 W/kg to 6800 W/kg, which is 100x higher than the typical average power per mass in a stirred tank. Energy dissipation profiles from CFD simulations show that the peak dissipation occurs at the impingement point and decays away in both radial and axial directions. The turbulence is thus inhomogeneous in the mixing volume and $\varepsilon_{\max} / \varepsilon_{\text{avg}} \approx 40$. An important advantage of the CIJR is that all the incoming fluid must pass through the maximum energy dissipation region shortly after entering the CIJR.

Both homogeneous and heterogeneous reactions were studied as micromixing probes and confirmed the high mixing efficiency of the CIJR. Experimental results showed that both feed concentration and flowrate affect the product yield in the homogeneous case, and the particle size in the heterogeneous case. The effect of mixing is most pronounced at high reactant concentrations. The product yield from the CIJR was consistently higher than the best performance yield of an equivalent CSTR.

Under unequal flow conditions the energy dissipation retained 84% of the value corresponding to the balanced-flow condition all the way to a 30% difference in flow rates. The product yield values for the homogeneous reaction also showed very robust performance. The yield remains surprisingly stable until the flow difference starts affecting the reaction stoichiometry and the pH. This finding suggests that initial reservations about the practicality of running a CIJR under imperfect plant conditions and varying inlet flow rates can be set aside.

It is thus concluded that the CIJR offers very high energy dissipation rates with the added advantage that all of the incoming fluid must pass through the maximum energy dissipation zone. The fluid mixing performance is remarkably stable even for flow rates which differ by up to 30% by volume. This reactor design shows increasing promise for situations where the mixing conditions must

be tightly controlled to ensure high product quality (i.e. less by-product impurity).

Tables

Table 2-1: Reagent concentrations for iodide-iodate reaction

Feed stream (inlet)	Reagent	Conc. 1 (M)	Conc. 2 (M)	Conc. 3 (M)	Conc. 4 (M)
1	I ⁻	0.0234	0.0234	0.0234	0.0234
1	IO ₃ ⁻	0.00466	0.00466	0.00466	0.00466
1	H ₂ BO ₃ ⁻	0.1818	0.1818	0.1818	0.1818
2	H ⁺	0.0626	0.0936	0.1566	0.1818

Table 2-2: Reagent concentrations for iron oxide precipitation reaction

Feed stream (inlet)	Reagent	Conc. 1 (M)	Conc. 2 (M)	Conc. 3 (M)
1	Fe ²⁺	0.01	0.036	0.18
1	Fe ³⁺	0.02	0.072	0.36
2	OH ⁻	1.45	1.45	1.45

Table 2-3: Time steps used for unsteady reactor simulations

Flow rate (ml/min)	Simulation time step (s)
70	7.5×10^{-6}
165	3.0×10^{-6}
300	1.5×10^{-6}
500	1.0×10^{-6}

Table 2-4: Energy dissipation rates in CIJR

Jet flow rate (mL/min)	Energy dissipation rate (W/kg)		
	Experimental	CFD	
		1 time step	Average of 3 time steps
70	15	19.7	19.7
165	231	235	235
311	1592	1360 (at 300 mL/min)	1365 (at 300 mL/min)
509	6802	6005 (at 500 mL/min)	6018 (at 500 mL/min)

Table 2-5: Comparison of mixing performance in CIJR and Stirred Tank

	$\epsilon_{\max}/\epsilon_{\text{avg}}$	$V_{\max}/V_{\text{total}}$	$V_{\text{avg+}}/V_{\text{total}}$
CIJR – median	44	1/500	1/7
70 mL/min	23	1/109	1/3
165 mL/min	45	1/460	1/5
300 mL/min	43	1/560	1/10
500 mL/min	33	1/513	1/13
Stirred tank – generic comparison	50	1/135	<1/75
Stirred tank – impeller volume ^a PBT4D, D=T/3, C= T/2	147	1/135	
Stirred tank – impeller volume ^a RT, D=T/3, C= T/2	24	1/135	
Stirred tank –impeller discharge ^b PBT4D, D=T/3, C=T/3	46	1/750	
Stirred tank – impeller discharge ^b RT, D=T/3, C=T/3	47	1/640	
Stirred tank –trailing vortex core	≈500	≈1/1500	-

^aZhou and Kresta (Chem Eng Res Des, 1996a); ^bZhou and Kresta (AIChE J, 1996b)

Figures

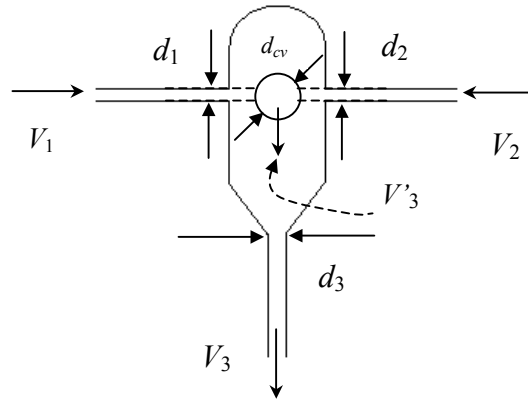


Figure 2-1: CIJR schematic for energy dissipation rate calculation

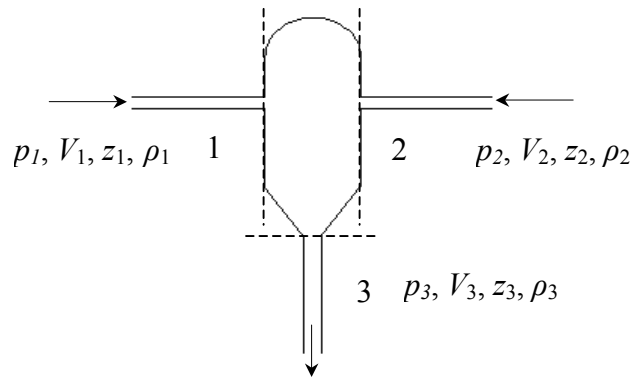
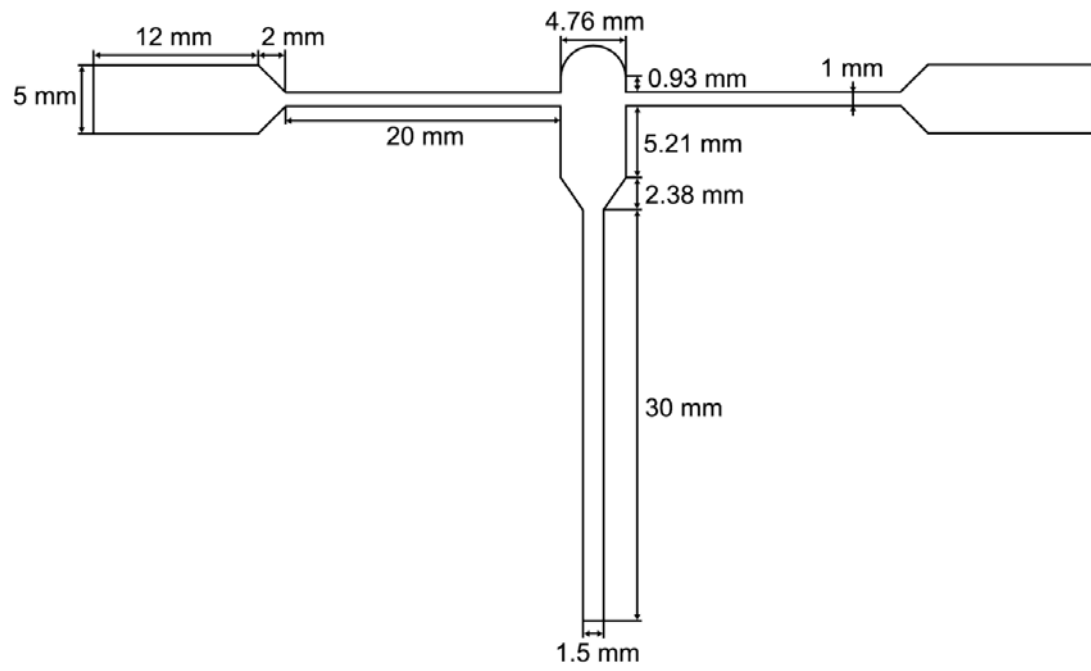
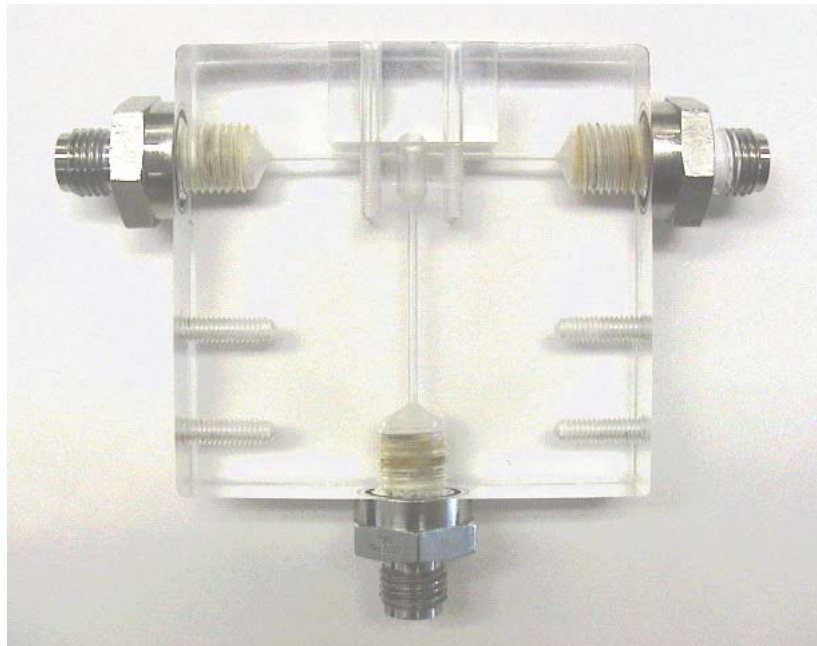


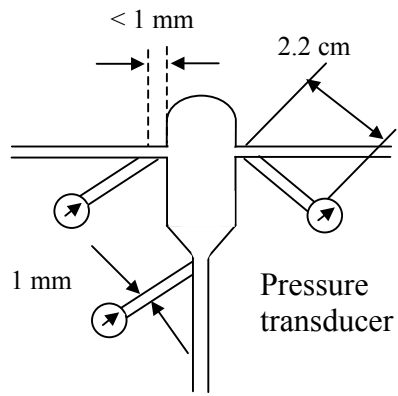
Figure 2-2: CIJR schematic for mechanical energy balance



(a)



(b)



(c)

Figure 2-3: CIJR (a) dimensions, (b) construction, and (c) configuration of pressure transducers.

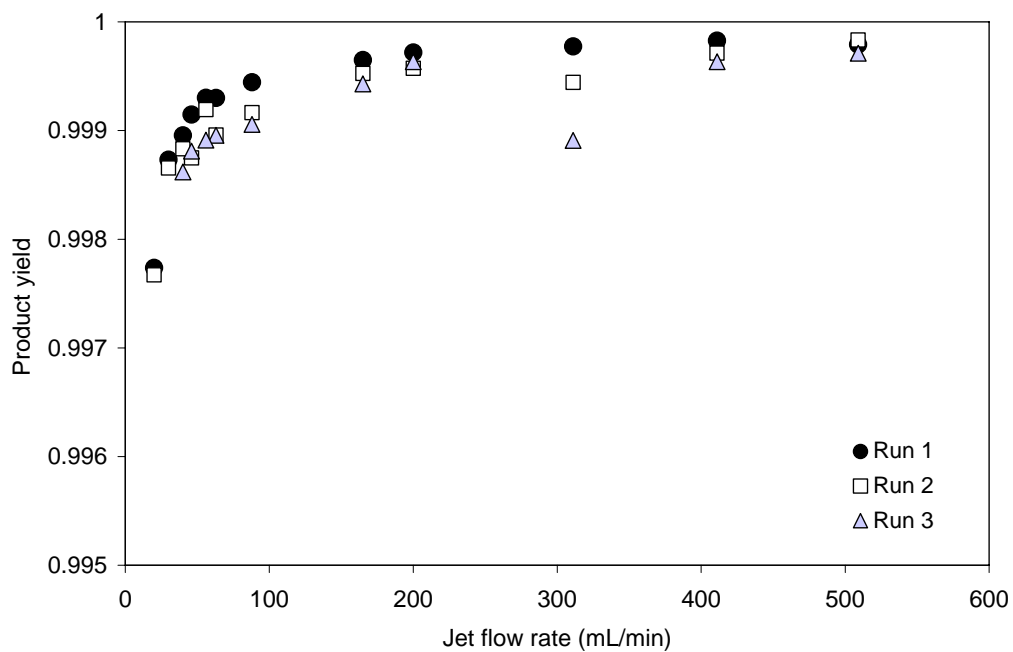
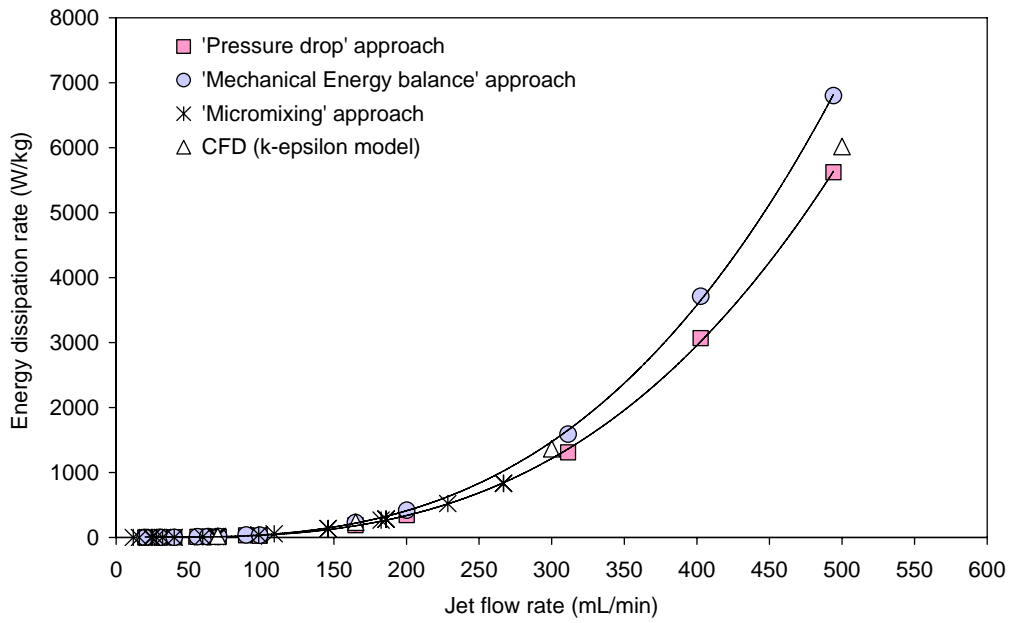
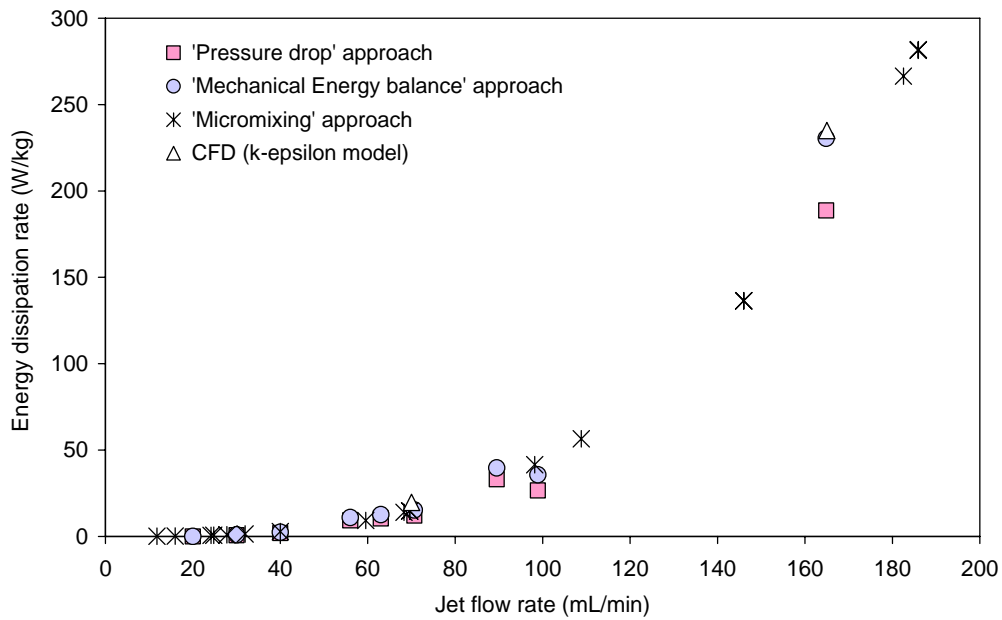


Figure 2-4: Effect of jet flow rate on reproducibility at $[H^+] = 0.0936$ M and buffer reagent $[H_2BO_3^-] = 0.1818$ M. Standard deviation $< 1.03 \times 10^{-4}$ for all flow rates.

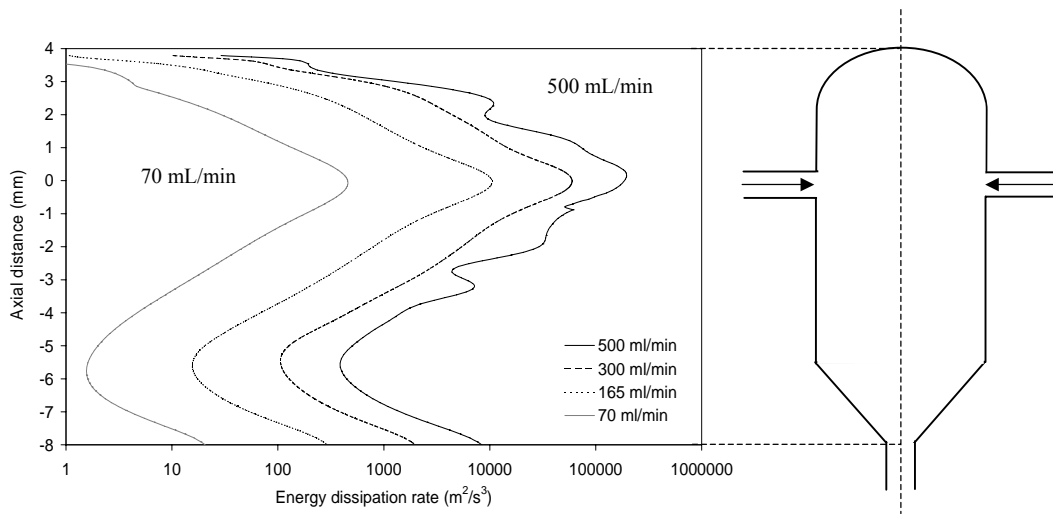


(a)

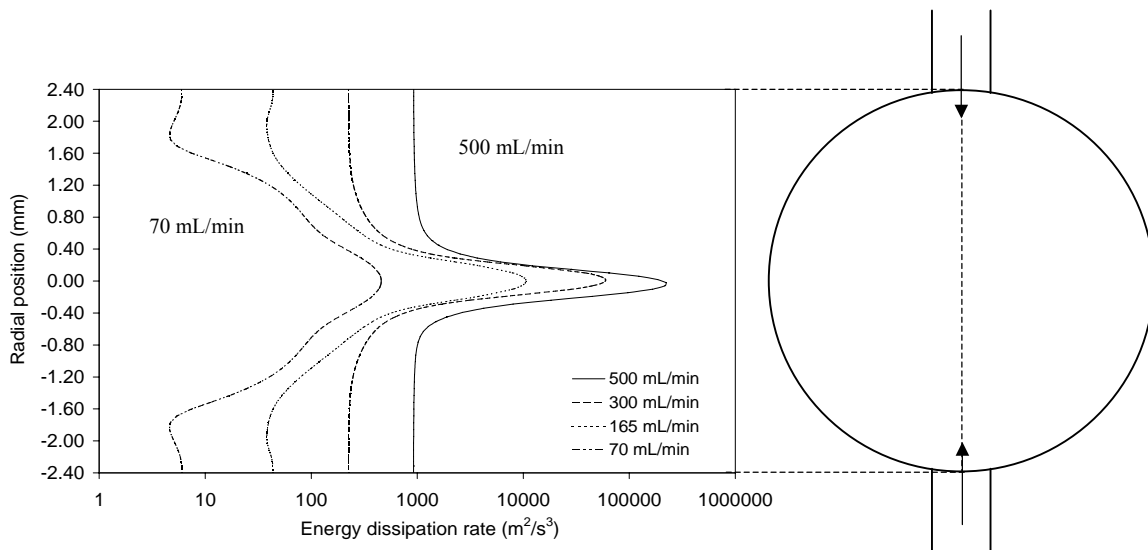


(b)

Figure 2-5: Effect of jet flow rate on energy dissipation rate at (a) all flow rates and (b) low flow rates. Pressure drop (eqn. 2-19), Mechanical Energy balance (eqn. 2-20), Micromixing (eqn. 2-14) and CFD approach based on the chamber volume.

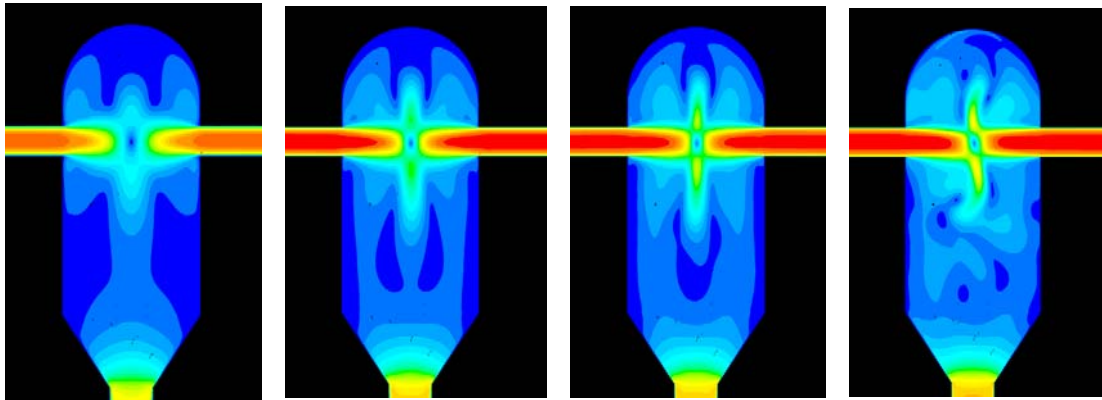


(a)



(b)

Figure 2-6: Variation of energy dissipation rate in (a) axial direction and (b) radial direction with varying jet flow rates. The origin is placed at the impingement point.



(a) 70 mL/min (b) 165 mL/min (c) 300 mL/min (d) 500 mL/min

Figure 2-7: Mean velocity contours in CIJR at one time step for flow rates increasing from 70 mL/min to 500 mL/min. The maximum velocity (red) is a) 2.17 m/s, b) 4.44 m/s, c) 7.72 m/s, d) 12.6 m/s. The dark blue regions approach zero mean velocity in all figures.

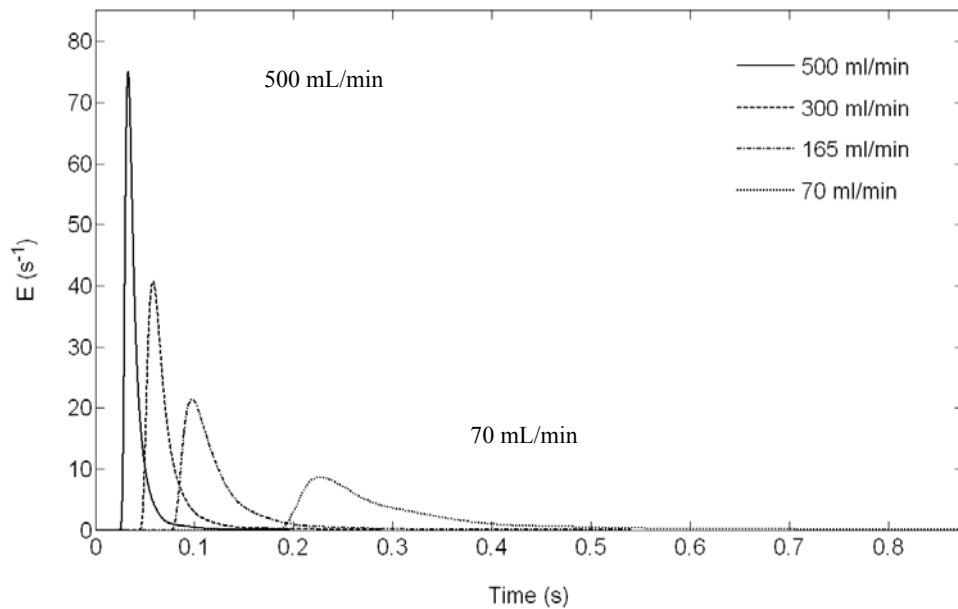


Figure 2-8: Residence time distribution in the CIJR computed from CFD simulations of tracer dispersion at four flow rates.

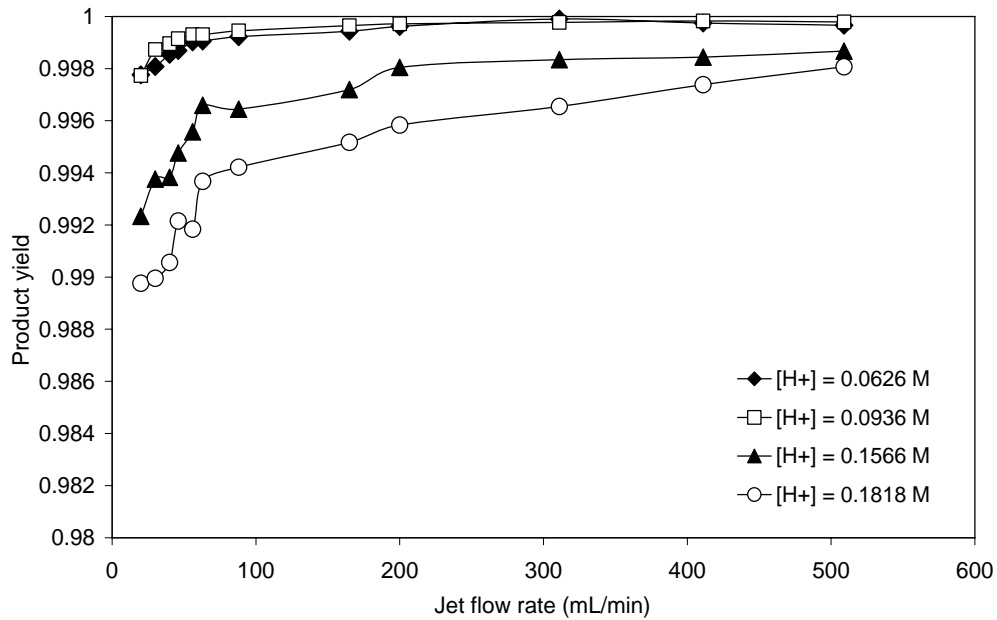


Figure 2-9: Effect of flow rate on product yield under varying limiting reagent concentration $[H^+]$ and for buffer reagent concentration $[H_2BO_3^-] = 0.1818 \text{ M}$

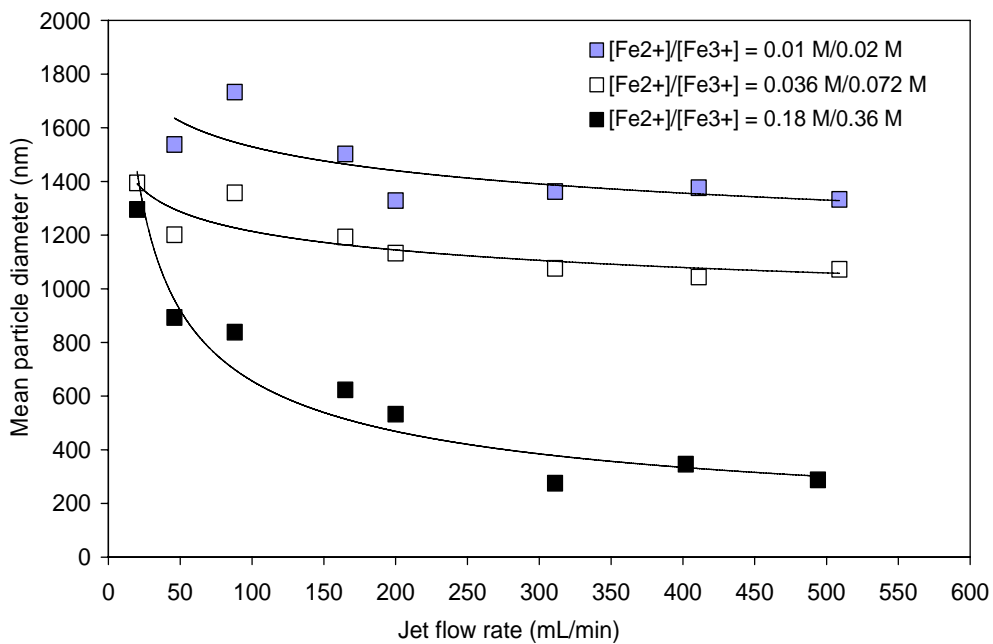
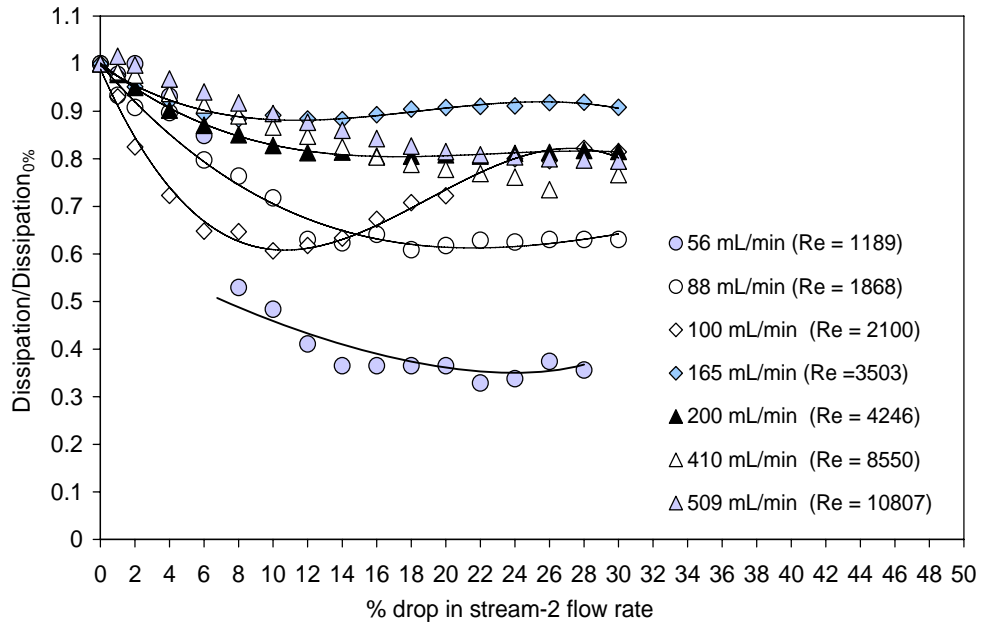
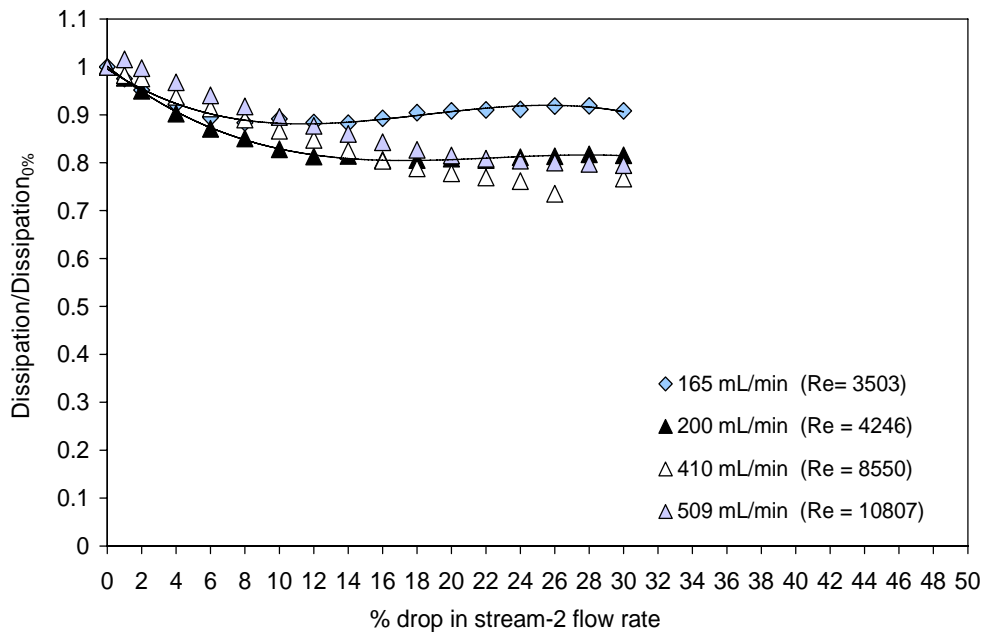


Figure 2-10: Effect of jet flow rate on iron oxide mean particle size (d_{65})

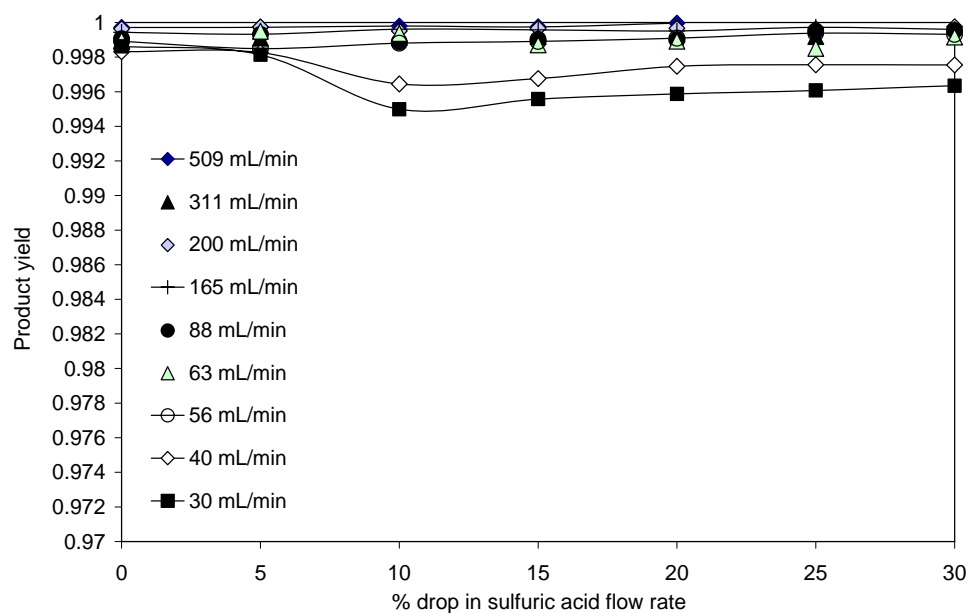


(a)

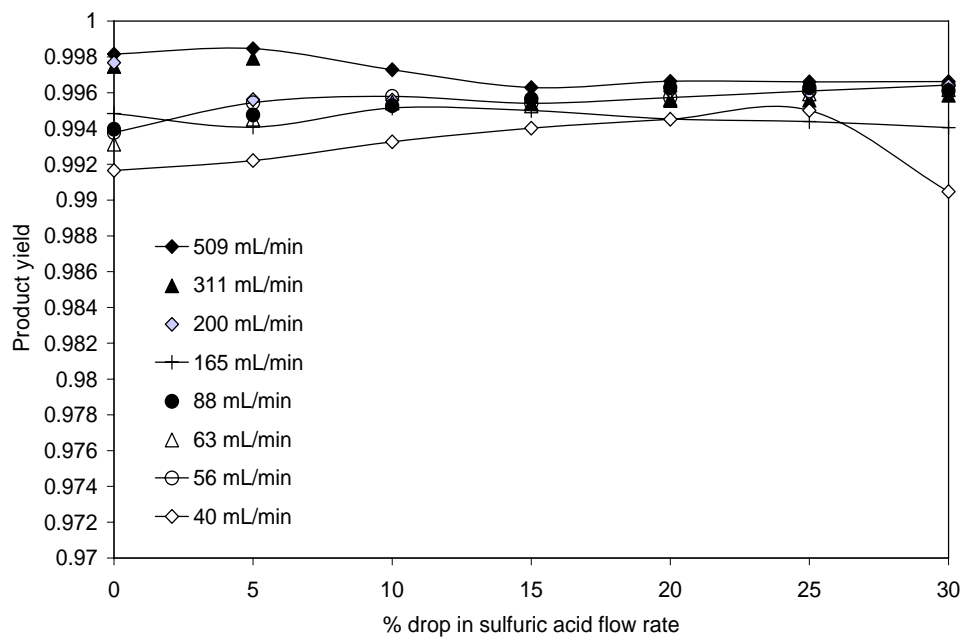


(b)

Figure 2-11: Effect of unequal flow on normalized energy dissipation rate at (a) all flow rates and (b) flow rates > 165 mL/min. The flow rate of stream 1 is held constant at the given value, while the flow rate of stream 2 is reduced.

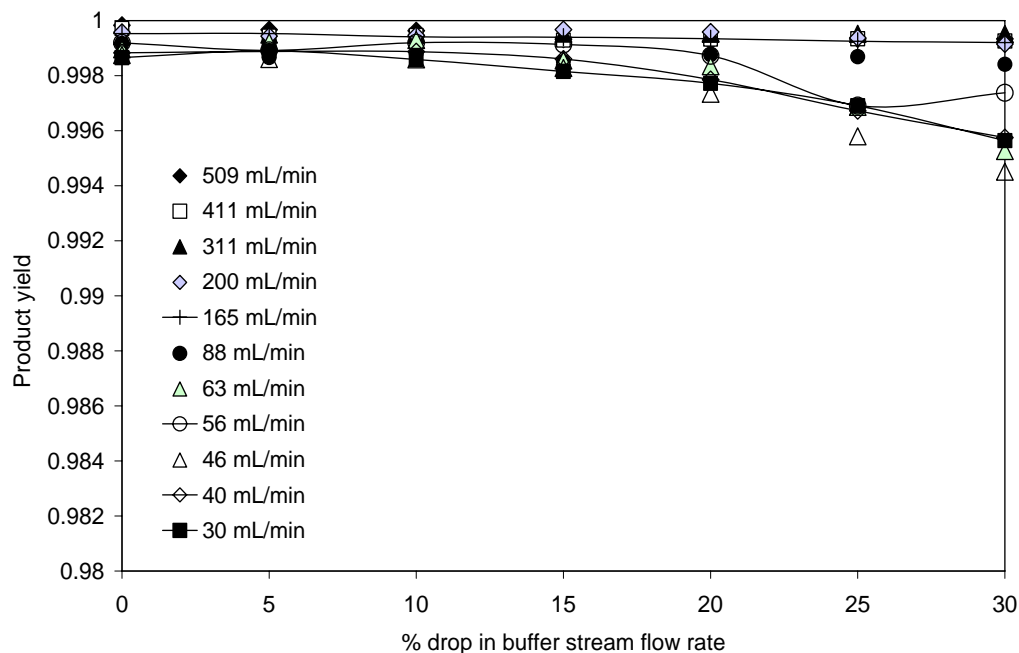


(a)

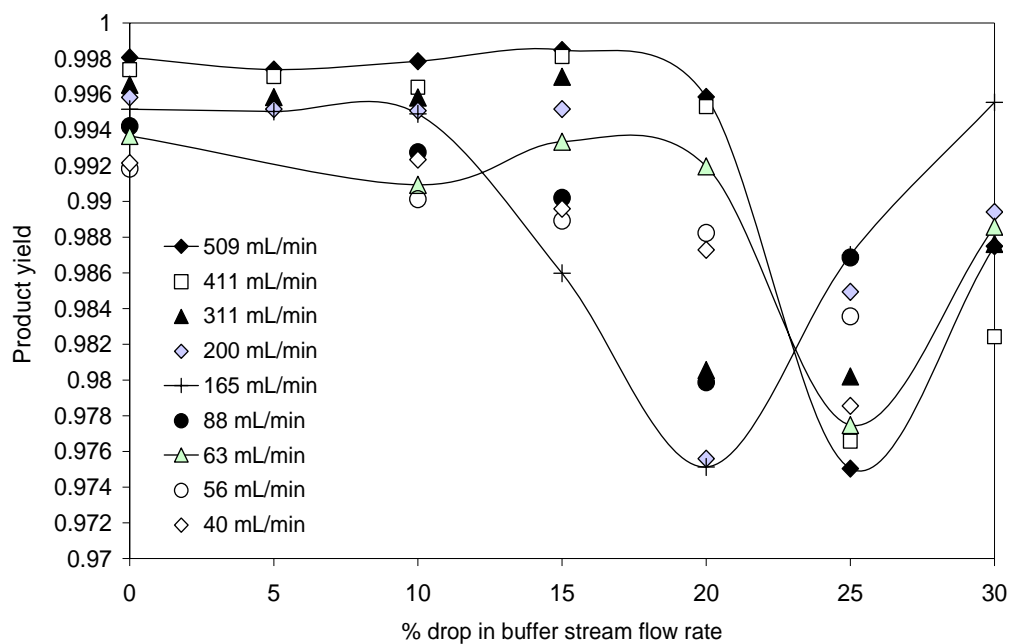


(b)

Figure 2-12: Effect of reduced sulfuric acid flow rate on product yield at (a) dilute: $[H^+] = 0.0936 M$ and (b) high concentration: $[H^+] = 0.1818 M$. $[H_2BO_3] = 0.1818 M$ for all experiments



(a)



(b)

Figure 2-13: Effect of reduced buffer flow rate on product yield at (a) dilute conditions $[H^+] = 0.0936$ M and b) high concentration, $[H^+] = 0.1818$ M. $[H_2BO_3^-] = 0.1818$ M for all experiments

Literature cited

- Abel, E. and F. Stadler, 1926, *Revision der Kinetik der HJO₃-HJ Reaktion*, Zeitschrift fuer Physikalische Chemie., **122**, 49-80.
- Abel, E. and K. Hilferding, 1928, *Revision der Kinetik der HJO₃-HJ Reaktion*, Zeitschrift fuer Physikalische Chemie A., **136**, 186-194.
- Assirelli, M., W. Bujalski, A. Eaglesham, A.W. Nienow, 2005, *Intensifying Micromixing in a semi-batch Reactor using a Rushton Turbine*, Chem. Eng. Sci., **60**, 2333-2339.
- Assirelli, M. E.J.W. Wynn, W. Bujalski, A. Eaglesham, A.W. Nienow, 2008, *An Extension to the Incorporation Model of Micromixing and its Use in Estimating Local Specific Energy Dissipation Rates*, Ind. Eng. Chem. Res., **47**, 3460-3469.
- Baldyga, J. and J.R. Bourne, 1983, *Distribution of Striation Thickness from Impingement Mixers in Reaction-Injection Molding*, Pol. Eng. Sci., **23**, 556-559.
- Barton, A.F.M., H.N. Cheong and R.E. Schmidt, 1975, *Kinetics of the Bromate-Iodide and Iodate-Iodide Reactions by pH-Stat Techniques*, J. Chem. Soc. Faraday Transactions, **1 (72)**, 568-574.
- Beattie, J.K., 1989, *Monodisperse Colloids of Transition Metal and Lanthanide Compounds*, Pure & Appl. Chem., **61 (5)**, 937-941.
- Bhattacharya, S. 2005, *Performance Improvement of Stirred Tank Reactors with Surface Feed*, PhD Thesis, University of Alberta, Canada.
- Bhattacharya, S. and S.M. Kresta, 2004, *Surface Feed with Minimum By-product Formation for Competitive Reactions*, Chem. Eng. Res. Des., **82**, 1153-1160.
- Bourne, J., 2008, *Comments on Iodide/Iodate Method for Characterizing Micromixing*, Chem. Eng. J., **140**, 638-641.
- Custer, J. J. and S. Natelson, 1949, *Spectrophotometric Determination of Micro Quantities of Iodine*, Analytical Chem., **21 (8)**, 1005-1009.

- Dong, W., 2002, *Use of Ethylene Oxide in the Sol-Gel Synthesis of α -Fe₂O₃ Nanoparticles from Fe(III) Salts*, J. Mater. Chem., **12**, 1676-1683.
- Ehrfeld, W., K. Golbig, V. Hessel, H. Lowe, T. Richter, 1999, *Characterization of Mixing in Micromixers by a Test Reaction: Single Mixing Units and Mixer Arrays*, Ind. Eng. Chem. Res., **38**, 1075-1082.
- Fournier, M.C., L. Falk, J. Villiermaux, 1996, *A New Parallel Competing Reaction System for Accessing Micromixing Efficiency: Experimental Approach*, Chem. Eng. Sci., **51 (23)**, 5053-5064.
- Gavi, E., D.L. Marchisio and A.A. Barresi, 2007, *CFD Modelling and Scale-up of Confined Impinging Jet Reactors*, Chem. Eng. Sci., **62**, 2228-2241.
- Goia, D.V., 2004, *Preparation and Formation Mechanisms of Uniform Metallic Particles in Homogeneous Solutions*, J. Mater. Chem., **14**, 451-458.
- Goia, D.V. and E. Matijević, 1998, *Preparation of Monodispersed Metal Particles*, New J. Chem., **11**, 1203-1215.
- Guichardon, P. and L. Falk, 2000, *Characterization of Micromixing Efficiency by the Iodide-Iodate Reaction System. Part I: Experimental Procedure*, Chem. Eng. Sci., **55**, 4233-4243.
- Guichardon, P., L. Falk and J. Villiermaux, 2000, *Characterization of Micromixing Efficiency by the Iodide-Iodate Reaction System. Part II: Kinetic Study*, Chem. Eng. Sci., **55**, 4245-4253.
- Herbo, C. and J. Sigallia, 1957, *Principles de L'iodimetric Absorptiometrique*, Analytica Chimica Acta., **17**, 199-207.
- Hirshfeld, D., 2006, *Study of Surface Feed in a Stirred Tank and CIJR using an Iodide-Iodate Competitive Reaction Scheme*, Technical Report, University of Alberta, Canada.
- Jain, T., M.A. Morales, S.K. Sahoo, D.L. Lelie-Pelecky and V. Labhasetwar, 2005, *Iron Oxide Nanoparticles for Sustained Delivery of Anticancer Agents*, Molecular Pharmaceutics, **2 (3)**, 194-205.

- Johnson, B. K., 2003, *Flash NanoPrecipitation of Organic Actives via Confined Micromixing and Block Copolymer Stabilization*, Ph.D. Thesis: Volume 1 and 2, Princeton University, USA.
- Johnson, B. K. and R.K. Prud'homme, 2003, *Chemical Processing and Micromixing in Confined Impinging Jets*, *AIChE Journal*, **49 (9)**, 2264-2282.
- Jolivet, J. P., E. Tronc and C. Chaneac, 2000, *Synthesis of Iron Oxide and Metal-Based Nanomaterials*, *Eur. Phys. J. AP*, **10**, 167-172.
- Jolivet, J. P., E. Tronc and C. Chaneac, 2002, *Synthesis of Iron Oxide Based Magnetic Nanoparticles and Composites*, *C. R. Chimie*, **5**, 659-664.
- Lee, L., J.M. Ottino, W.E. Ranz and C.W. Macosko, 1980, *Impingement Mixing in Reaction-Injection Molding*, *Polymer Eng. and Sci.*, **20**, 868-874.
- Lieser, K.H, 1969, *Steps in Precipitation Reactions*, *Angew. Chem. Internat. Edt.*, **8 (3)**, 188-202.
- Lin, C.L., C.F. Lee and W.Y. Chui, 2005, *Preparation and Properties of Poly(acrylic acid) Oligomer Stabilized Superparamagnetic Ferrofluid*, *J. Colloid and Interface Sci.*, **291**, 411-420.
- Liu, Y. and R. Fox, 2006, *CFD Predictions for Chemical Processing in a Confine Impinging-Jets Reactor*, *AIChE J.*, **52 (2)**, 731-744.
- Lu, A., E.L. Salabas and F. Schüth, 2007, *Magnetic Nanoparticles: Synthesis, Protection, Functionalization and Application*, *Angew. Chem. Internat. Edt.*, **46 (8)**, 1222-1244.
- Mahajan, A. J. and D.J. Kirwan, 1996, *Micromixing Effects in a Two-Impinging-Jets Precipitator*, *AIChE J.*, **42(7)**, 1801-1814.
- Maity, D. and D.C. Agrawal, 2007, *Synthesis of Iron Oxide Nanoparticles Under Oxidizing Environment and their Stabilization in Aqueous and Non-Aqueous Media*, *J. Magnetism and Magnetic Mat.*, **308**, 46-55.
- Malguarnera, S.C. and N.P. Suh, 1977, *Liquid Injection Molding I. An Investigation of Impingement Mixing*, *Polymer Eng. Sci.*, **17**, 111-115.

- Marchisio, D. L., L. Rivautella and A. Barreri, 2006, *Design and Scale-Up of Chemical Reactors for Nanoparticle Precipitation*, *AIChE J*, **52 (5)**, 1877-1887.
- Matijević, E., 1991, *Preparation and Properties of Well Defined Finely Dispersed Metals*, *Faraday Discussion*, **92**, 229-239.
- Mikhaylova, M., D.K. Kim, N. Bobrysheva, M. Osmolowsky, V. Semenov, T. Tsakalakos and M. Muhammed, 2004, *Superparamagnetism of Magnetite Nanoparticles: Dependence on Surface Modification*, *Langmuir*, **20**, 2472-2477.
- Monnier, H., A.M. Wilhelm and H. Delmas, 1999, *The Influence of Ultrasound on Micromixing in a Semi-batch Reactor*, *Chem. Eng. Sci.*, **54**, 2953-2961.
- Munoz, A. 2004, *Sensitivity Analysis of the CFD Approach to Predict the Performance of large UV Reactors*, MSc Thesis, University of Alberta, Canada.
- Nguyen, L.T. and N.P. Suh, 1985, *Effect of High Reynolds Number on the Degree of Mixing in RIM Processing*, *Polymer Process Eng.*, **3**, 37.
- Palmer, D.A., R.W. Ramette and R.E. Mesmer, 1984, *Triiodide Ion Formation Equilibrium and Activity Coefficients in Aqueous Solution*, *Journal of Solution Chemistry*, **13 (9)**, 673-683.
- Sandell, D.J., C.W. Macosko and E.W. Ranz, 1985, *Visualization Technique for Studying Impingement Mixing at Representative Reynolds Numbers*, *Polymer Process Eng.*, **3**, 57.
- Schildcrout, S.M. and F.A. Fortunato, 1975, *A Spectrophotometric Study of the Rate of the Aqueous Iodate-Iodide Reaction*, *J. Phys. Chem.*, **79 (1)**, 31-34.
- Schwarzer, H. and W. Peukert, 2004, *Combined Experimental/Numerical Study on the Precipitation of Nanoparticles*, *AIChE J*, **50 (12)**, 3234-3447.
- Siddiqui, S, 2009, *Use of the Confined Impinging Jet Reactor for Production of Nanoscale Iron Oxide Particles*, PhD Thesis, University of Alberta, Canada.

- Stark, A.J. and S.E. Pratsinis, 2002, *Aerosol Flame Reactors for Manufacture of Nanoparticles*, Powder Technology, 103-108.
- Tucker, C.L. and N.P. Suh, 1978, *Impingement Mixing – A Mechanical Approach*, Soc. of Plastic Engineers 36th Ann. Tech. Conf., Washington, USA.
- Wronska, M. and B. Banas, 1965, *Kinetics Investigations on the Oxidation of Iodide and Iodate*, Bulletin de l'Academi Polanaise de Sciences, Series des Sciences, Chemies, **13 (1)**, 5-7.
- Zhao, Y., 2007, *Characterizing CIJR using Iodide-Iodate Reaction*, Technical Report, University of Alberta, Canada.
- Zhou, G. and S.M. Kresta, 1996, *Distribution of Energy Between Convective and Turbulent Flow for Three Frequently Used Impellers*, Chem. Eng. Res. Des., **74A**, 379-389.
- Zhou, G. and S.M. Kresta, 1996, *Impact of Tank Geometry on the Maximum Turbulence Energy Dissipation Rate for Impellers*, AIChE J., **42 (9)**, 2276-2290.

Chapter 3

Nanoparticle Precipitation, Agglomeration and its Control in Confined Impinging Jet Reactor

Introduction

The purpose of this work is to develop a methodology for producing submicron iron oxide particles (model system) on a continuous basis using the Confined Impinging Jet Reactor (CIJR). In particular, this work investigates the role of flow rate (and mixing), reactant concentration, stabilizer concentration and type, stabilizer addition point (in situ vs. post-reaction) and sonication strategy (in situ vs. post-reaction) in successfully precipitating nanoparticles and controlling their subsequent agglomeration.

Nanoparticles (and submicron particles) have attracted significant research and industrial attention because of the tendency to exhibit different characteristic properties than the bulk material. Optical, magnetic, electric, adsorptive, and catalytic material properties depend on the particle size, morphology (Goia and Matijević, 1998), particle-size distribution (Schwarzer and Peukert, 2002), and aggregation (Jolivet et. al, 2002). Property changes are attributed to the increasing influence of surface properties over the bulk-material properties upon a substantial decrease in particle size (Schwarzer and Peukert, 2002).

Submicron particles can be obtained by setting suitable conditions for nanoparticles to form, arresting individual particle growth and limiting any interparticle growth and agglomeration. Techniques such as chemical reduction, and flame synthesis can be used, but chemical co-precipitation from homogenous solutions is a more promising synthesis route for making large amounts of material because of its fast kinetics. It also gives control over the particle size and product properties through control of reactant concentration, stabilizer concentration, pH etc. (Goia and Matijević, 1998). Whereas some metal particles can be directly obtained through a reduction reaction (Matijević, 1991 and Goia, 2004), metal hydroxides are obtained through precipitation reactions between an

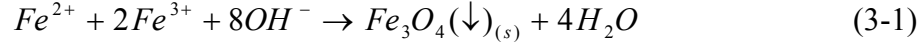
aqueous metal salt and a base solution under high supersaturation conditions, which dehydrolyses at room or higher temperature yielding metal oxides (Beattie, 1989).

The essential rapid mixing of reagents is brought about by high local energy dissipation in the CIJR (Siddiqui et al., 2009). Mixing facilitates build-up of local supersaturation which is discharged by rapid precipitate formation in a fast chemical precipitation reaction. The faster the mixing is, the smaller the particles (Mersmann et al., 1994; Siddiqui et al., 2009). Post nucleation, the remaining supersaturation is consumed in particle growth and subsequent agglomeration of the precipitated nanoparticles (Siddiqui et al., 2009). This aggregational growth transforms nanoparticles into submicron particles.

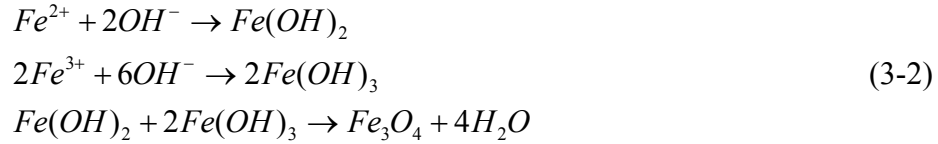
Though precipitation reactions traditionally have been carried out in stirred tanks, impinging jets have caught attention in recent years. Impinging jets offer a better choice over stirred tanks due to their fast, efficient, intense and continuous mixing characteristics (Siddiqui et al., 2009). The local energy dissipation rate (indicator of the mixing intensity) in the CIJR is several orders of magnitude higher than in a stirred tank. Energy dissipation varies between 20W/kg to 6800W/kg for the range of flowrates investigated (Siddiqui et al., 2009). Confined impinging jets have been used in both organic (Johnson et al., 2003) and inorganic nanoparticle (Marchisio et al., 2006) synthesis.

In this work, iron (II, III) oxide (magnetite Fe_3O_4) is studied as a model system as it is easily synthesized via co-precipitation of Fe(II) and Fe(III) salts by addition of a base at ambient conditions. Iron oxide is obtained from co-precipitation of ferrous-ferric hydroxides and removal of water molecules from the amorphous hydroxides. Jolivet et al. (2002) report that precipitation in aqueous phase is an easy and economical synthesis route for metal oxides e.g. iron oxides (magnetite Fe_3O_4 and maghemite $\gamma\text{-Fe}_2\text{O}_3$) and substituted magnetites (MFe_2O_4 , M = Fe, Co and Ni) can be easily precipitated. Gupta and Gupta (2005) argued that the chemical precipitation route for making magnetic nanoparticles was a simpler and more efficient route with a good control over the particle size, composition and ‘sometimes’ the shape of the nanoparticles. They reported that

the size, shape and composition of the nanoparticles were dependent on pH, ferrous-ferric ratio, ionic strength and the anion type. These particles find numerous applications in ceramics, pigments, high-density magnetic storage, catalysts and controlled pharmaceuticals-drug release (Goia et al., 1998; Lin et al., 2005; Gupta and Gupta, 2005). Iron oxide precipitates according to the following overall reaction scheme (Lin et al., 2005; Maity and Agrawal, 2007).



The intermediate steps are simplified as:



Of the intermediate hydroxide precipitation steps, ferrous hydroxide is found to be the rate-limiting step (Tronc et al., 1992 and Faivere et al., 2004). Gupta and Gupta (2005) report that complete precipitation of Fe_3O_4 was expected between pH of 9 and 14 with Fe^{2+}/Fe^{3+} of 1:2 in a non-oxidizing environment to prevent oxidation of Fe_3O_4 to ferric hydroxide. Kang et al. (1996) reported that homogeneous and uniform sized iron oxide particles could be obtained at a pH of 11-12 with Fe^{2+}/Fe^{3+} ratio of 1:2. This has been confirmed by running a series of precipitation reaction at varying Fe^{2+} , Fe^{3+} and OH^{-} concentrations. Though no significant effect of pH on agglomerate size was seen, primary particle size decreased with increase in pH. Small primary particles (8-9 nm) are obtained at high pH (10-12.5) conditions. On increasing or decreasing the reaction mixture pH, the electrostatic charge on the particle surface is altered and so is the chemical composition of the particle-solution interface, which alters the interfacial tension. Interfacial tension varies according to the following equation:

$$d\gamma = -\Gamma d\mu \quad (3-3)$$

where γ = interfacial tension, Γ = density of the absorbed species and μ = chemical potential.

It was argued that smaller magnetite nanoparticles could be prepared at low reaction temperature (Gupta and Gupta, 2005) and in the presence of N_2 that prevented oxidation of magnetite and helped in reducing particle size (Maity and

Agrawal, 2007). Jolivet et al. (2002) report that due to high electron mobility magnetite nanoparticles are highly susceptible to oxidation to maghemite (γ - Fe_2O_3) and that the mean particle size depends on reaction pH and ionic strength of the reaction systems. They showed that particle size decreased with an increase in pH and ionic strength. A 2-fold decrease in particle size (12.5nm to 6.5nm) was observed for a pH increase from 9 to 12 and likewise a 4-fold decrease in particle size (6.5nm to 1.6nm) was seen for a 6-fold increase in ionic strength (0.5M to 3M). Maity and Agrawal (2007) reported that Fe_3O_4 synthesis under oxidizing environment would change the Fe^{2+} to Fe^{3+} ratio, resulting in maghemite (γ - Fe_2O_3) and very little magnetite (Fe_3O_4). They used various $\text{Fe}^{2+}/\text{Fe}^{3+}$ ratio (≤ 0.5) and concluded that predominantly maghemite was obtained despite the variation in Fe^{2+} and Fe^{3+} ratio. They argued that various phases (magnetite and maghemite) were difficult to identify because of the similar X-ray diffraction patterns (Maity and Agrawal, 2007), d-spacing and SAED diffraction patterns (Teng and Yang, 2004), however; the core electron lines of ferrous and ferric state from XPS could be used to determine the oxidation states of iron (Teng and Yang, 2004).

To facilitate the formation of nanoparticles at low energy input (low mixing rates), additives need to be used along with the precipitating system to stabilize the particles. Polymers and surfactants are both used for the purpose. Surfactant molecules with their hydrophobic and hydrophilic ends orient themselves at the particle interface such that the interfacial tension decreases, leading to a decrease in the energy required to create a new interface. If the polymer chain is sufficiently large it may also serve as an active stabilizing agent through steric means. The stabilizer chains would compress upon particle contact, generating osmotic pressure, which would push the particles away. Thus successful control of aggregation or agglomeration of primary particles calls for the use of stabilizers in nanoparticle manufacture. Stabilizer molecules adsorb over the particle surface, decreasing the number of active sites to reduce particle-particle surface-contact area and thus further crystal growth (Maity and Agrawal, 2007). Less surface-contact implies fewer hard bridges between particles, which form

when precipitation occurs between the interparticle spaces of particles in contact, or under diffusive growth on a particle surface.

If a stabilizer is added post-precipitation then hard (crystalline) bridges have already formed and the only benefit that could be achieved is the reduction of soft agglomerates by stabilization of hard agglomerates. Soft agglomerates form via assembly of several hard agglomerates under attractive Van der Waals and magnetic forces. On the other hand, hard agglomerates are aggregates of nanoparticles that have undergone interparticle growth or material bridge formation between the particles. Thus, if stabilizer is added to the reactant stream it can adsorb on the nanoparticles at the very onset of formation and reduce the number of active sites available for further chemical bonds. Larger additive molecules may provide better particle-surface coverage upon adsorption and may also prevent approach through steric hindrance. The efficiency of a stabilizer thus depends on: (i) the functional group, (ii) additive quantity, (iii) effective reaction-mixture pH, (iv) strength of ionic species in the reaction mixture, (v) adsorption time and (vi) chain length and structure.

Some previous works are reviewed below to understand the working of the common stabilizers with metal and metal oxides.

Unwin et al. (2008) studied the effect of sec. butylamine and propylamine on aggregation of copper particles (< 2 microns). They proposed that shorter chain secondary amines could prevent agglomeration of copper particles as they could provide sufficient charge to the particle surface to encourage electrostatic interparticle repulsion, prevent the solvent from reaching the particle surface and thus prevent oxidation and oxide bridge formation.

Hong et al. (2008) synthesized dextran stabilized magnetic nanoparticles through a reduction-precipitation reaction. Dextran was added in situ and observed to reduce particle size and improve particle dispersion. Steric stabilization was the stabilizing mechanism and was understood to increase with molecular weight of dextran wherein its coating efficiency increased with dextran to particle (wt.) ratio. The suspension stability increases with increase in dextran to particle (wt.) ratio.

Xu and Gu (2001) synthesized magnetic nanoparticles for bio-separation through co-precipitation technique using dextran as the stabilizing agent. Magnetic iron oxide particles in the average particle size range of 150-200 nm (smallest size ~ 30 nm) were produced by post-precipitation stabilization with excellent stability. Dutz et al. (2007) synthesized magnetic iron oxide particles through precipitation route with dextran. Dextran however offered low uptake by the particles and poor stability against particle sedimentation.

Hong et al. (2006) synthesized magnetic particles through co-precipitation reaction with Fe^{3+} to Fe^{2+} ratio of 1.75 and under Ar protection. Magnetic particles were dual-coated with sodium oleate and polyethylene glycol to improve the stability. TEM images showed that the primary particles were about 10nm in size with average agglomerate size between 30-40nm.

Matijevic and Cimaš (1987) synthesized ferric oxide by hydrolysis of acidified ferric chloride in ethylene glycol/water solutions of varying composition. It was noted that ethylene glycol prevented precipitation when its concentration exceeded 40% (by vol.). pH was also found to be an important variable (controlled by concentrations of FeCl_3 and HCl) wherein if $\text{pH} > 1$ shorter rods or needles were obtained, whereas if $\text{pH} < 1$ particles were either elongated in size or of entirely different shapes.

McGuire et al. (2006) used polyacrylamide to synthesize stabilized iron oxide particles. They found that the interactions between the anionic polyacrylamide-Na and iron oxide were electrostatic in nature. Jones et al. (1998) reported that at $\text{pH} = 7$, the polyacrylate group was bound to the hematite surface through the hydrogen bonding between the carboxylate group of the polymer and the hydroxyl group on the hematite surface.

Bajpai and Bajpai (1995) studied adsorption of polyacrylamide at the iron oxide interface (hematite) and found that the adsorption of PAM (a non-ionic polymer) decreased with an increase in pH of the adsorption medium. The presence of anions (like chloride, sulphate and phosphate) caused a decrease in adsorption rate of PAM over the surface. Amides were understood to bond strongly to the surface due to resonance-stabilized structures and the formation of

hydrogen bond between the particle and CO group of the amide. They noted that the adsorption rate of PAM decreased with the molecular weight which was likely due to higher frictional resistance or smaller diffusivity in the fluid environment.

Furusawa et al. (1992) studied PAM adsorption on iron oxide (hematite) particles and found that adsorption decreased with an increase in particle concentration. At low pH the hematite particles were highly charged and stable under strong electrostatic repulsive forces. They found that PAM adsorption decreased with increase in pH. They argued that in highly concentrated particle systems, not all the particle surfaces could be available for PAM adsorption and thus the particle size increased with increasing particle concentration. They concluded that in a colloidal system, mixing of particle-polymer molecule was significant for facilitating polymer adsorption onto particles.

In addition to using surfactant or stabilizer to facilitate nanoparticle formation and limiting their agglomeration, ultrasonication is used to disperse the colloids and nano-suspension. In the present study it has been used in two different ways: first during particle formation and growth stage (in-situ), and secondly: after the reaction has gone to completion (post-reaction). In situ sonication is understood to promote surface uptake of stabilizer molecules by dispersing the precipitated primary particles into stabilizer, and was expected to disrupt the formation of agglomerates.

Banert et al. (2006) studied production of magnetic iron oxide particles using 3 different configurations of continuously operated sono-chemical reactors. It was assumed that almost 85%-90% of the electrical energy input was transformed to mechanical energy that was used for mixing. Monnier et al. (1999), however; assumed that almost 50% of the electrical energy input to the system was used as sonic energy in studying micromixing effects in stirred tank with the iodide-iodate reaction. Banert et al. (2006) noted that ultrasonication contributed to a further drop in particle size, further to hydrodynamic effect. Banert concluded that the effect of ultrasonication on the particle formation process depended on macromixing, which was brought about by hydrodynamics

within the reactor. Xu and Gu (2001) synthesized magnetic nanoparticles for bio-separation through co-precipitation reaction. They used the ultrasonication technique to micromix the reagents and found that the smallest particles were obtained at a $\text{Fe}^{3+}/\text{Fe}^{2+}$ ratio of 2. They obtained an average particle size of 150 to 200 nm with insitu sonication at a reaction pH of 12.05. Smaller particles were obtained with an increase in sonication intensity but levelled off at an intensity of 30% of the full scale. Ultrasonication was understood to limit the particle agglomeration, mechanically.

The objective of this work was to successfully control agglomeration during intense mixing conditions by identifying suitable stabilizer functional group, stabilizer concentration, stabilizer point of addition and sonication strategy (in-situ or post-reaction) for large-scale submicron iron oxide particle manufacture. A homogeneous mixing sensitive iodide-iodate reaction is also used to study mixing effects and support the observed energy dissipation trends in CIJR as reported by us (Siddiqui et al., 2009). CFD simulations have been used to identify changes in dissipation associated with the CIJR geometry on sonic probe addition.

Experimental

Experimental setup

Figure 3-1 (a), (b) and (c) give an isometric view and dimensions of the CIJR. Constant pulse-free flows to the CIJR were provided by micropump-head (Series GB, external gear pump, max flow rate 4L/min) installed on pump drives (MCP-Z standard, IDEX corporation). The pumps were calibrated by mass and volumetric flow methods for the whole range of flow rates under study. A flow visualization technique was also used to monitor flow stability under balanced flow conditions.

A modified CIJR geometry was used to incorporate a sonic probe into the mix-head for in situ sonication experiments as shown in Figure 3-1 (b). A sonicator (Dismembrator, Fisher Scientific, Model 500) was used for in-situ sonication which runs on a frequency of 20KHz and an output power of 400W.

The input energy was varied between 0 to 160W of which approximately 50% is assumed to be available as sonic energy for dissipation purpose. The CIJR geometry is modified such that the flat tip of the probe replaces the top of the hemispherical portion of the geometry.

Iron oxide reaction

Reagent solutions for the iron oxide reaction were prepared using Reverse-Osmosis treated water and certified quality ferrous chloride, ferric chloride and sodium hydroxide (Siddiqui et al., 2009). The solution concentrations are listed in Table 3-1.

The product solution collected from the CIJR was a suspension of precipitate, excess reagents and reaction products. It was washed multiple times with Reverse-Osmosis water and decanted. The sediment was further diluted with RO water to $\leq 1\%$ v/v (particle sizer specific recommendation) and sonicated for 15 minutes for particle size measurements in Brookhaven ZetaPlus particle size analyzer. The sample in the vial was re-sonicated for a minute before each size measurement to disperse any loose agglomerates. Brookhaven ZetaPlus measures the effective diameter (d_{65}) of the particles in suspension. d_{65} is the intensity weighted average diameter or the hydrodynamic diameter. Small polydispersity values (~ 0.005) were obtained i.e. the particles were monodisperse. For monodisperse spheres $d_{10} = d_{32} = d_{43} = d_{65}$. Particle sizing for each sample was repeated five times to ensure consistency in particle size and polydispersity measurements. The standard deviation varied between 120 nm and 15 nm over particle size measurements ranging from 1.5 micron to 200 nm over the range of flow rates investigated. Zeta potential measurements on the particles in suspension are often reported, but haven't been considered in this study.

Following the results of El-Khoury et al. (2007), the samples were not demagnetized before particle size measurements. El-Khoury et al. (2007) obtained stabilized magnetite nanoparticles with polyallylamine and found that though the particles were magnetic, the demagnetized nanoparticles did not show significant dispersion compared to those produced otherwise.

TEM (JEOL 2010, Japan) imaging was carried out on the sample after particle size measurements. The particle suspension was dropped onto 200-mesh carbon coated Cu grids (Pelco, USA) and allowed to dry before TEM images of the precipitate particles were collected. TEM images were used to measure primary particle sizes analysed using TEM imaging software from Advanced Microscopy Techniques (USA). Other techniques like X-ray diffraction and specific surface area measurements are often used to estimate primary particles in agglomerates, but are not employed in this work.

Surfactants and polymers used in this study to control agglomeration include Dextran (MW ~ 40,000); poly-acrylamide, PAM (MW ~ 10,000, (CH₂-CH-CONH₂)_n); sec. butylamine, BA (C₄H₉-NH₂); diethylene glycol, DEG (OH-C₂H₄-O-C₂H₄-OH) and triethylene glycol, TEG (OH-C₂H₄-O-C₂H₄-O-C₂H₄-OH).

Iodide-Iodate reaction

The three-step competitive-parallel iodide-iodate model reaction system has been extensively used as a micromixing probe for comparing various mixing geometries and varying mixing conditions in CIJR (Siddiqui et al., 2009), wherein the neutralization reaction is the fast and the product-forming reaction.



H₂BO₃⁻ ions are obtained from the coexisting H₃BO₃ and NaOH in the reaction mixture, which is a buffer solution. The slower reaction (Dushman reaction) proceeds by reaction of iodide, iodate and hydrogen ions, forming byproduct (I₂):



The byproduct iodine (I₂) further reacts with iodide ions to form the byproduct triiodide ions (I₃⁻).



Iodine (I₂) and triiodide (I₃⁻) are the byproducts and while the triiodide concentration is estimated from the measured absorbance (using a spectrophotometer) of the product solution, the iodine concentration is determined by mole balance. Under imperfect mixing conditions, local high

concentrations of H^+ occur in the reaction mixture facilitating byproduct formation. The product selectivity is thus determined by the ratio of the rate constants.

The product yield of the reaction depends on the number of moles of the limiting reagent (H^+) consumed in byproduct formation and is estimated as:

$$Y = 1 - \frac{\text{moles of } H^+ \text{ consumed in byproducts}}{\text{total moles of } H^+ \text{ added to the system}} \quad (3-7)$$

Reagent solutions for the product yield experiments were prepared in RO water using potassium iodate, potassium iodide, sodium hydroxide, boric acid powder and 10N sulfuric acid solution. Potassium iodide and iodate solutions were prepared in deoxygenated water to prevent any oxidation of iodide ions to iodine prior to reaction. A detailed solution preparation methodology was described elsewhere (Siddiqui et al., 2009). Table 3-2 gives the solution concentrations, corresponding to the inlet jet streams. Under equal flow rate conditions, the mean reagent concentrations in the reactor are half of that at the inlets.

Post reaction, the collected product samples were put to light absorbance measurements at a wavelength of 352 nm using an optical probe (7mm path length). The extinction coefficient was obtained by running a series of absorbance measurements with standard triiodide solutions and was estimated to be 1914.8 m^2/mol . The extinction coefficient was found to be sensitive to the fiber optic and the water source used for making standard solutions. Details are discussed elsewhere by the author (Siddiqui et al., 2009). Error bars have not been plotted on the yield results because they were roughly of the same size as the symbols.

Results

The results are divided in 3 parts. The first part explores the effect of feed reagent concentration, flow rate and post-precipitation sonication on hard agglomerate and primary particle size. In second part we investigate the effects of stabilizer types and their concentration on primary particle and hard agglomerate size. The third and final part investigates mixing effects induced by

modification of CIJR mixing volume due to insertion of the sonic probe for in situ sonication. Mixing effects are tracked via iodide-iodate product yield measurements and variation in primary particle and hard agglomerate size in the presence and absence of stabilizing agent.

Flow rate, post-precipitation sonication and feed concentration

Figure 3-2 shows the effect of flow rate on soft and hard agglomerate sizes and the effect of post-reaction sonication in dispersing soft aggregates. Whereas the soft agglomerate sizes vary between 1 micron and 2 microns, hard agglomerate size is seen to decrease gradually (1 micron to 200nm) with an increase in flow rate from 20 mL/min to 500 mL/min. As the supersaturation generation rate increases with more intense mixing, the supersaturation needs to be released in a shorter period. This leads to precipitation of a larger number of smaller hard agglomerates. Hard agglomerates are comprised of primary particles bound together through hard material bridges. The hard agglomerates size was seen to decrease with an increase in primary particle size under varying mixing conditions (Siddiqui, 2009).

Figure 3-3 shows the effect of post-precipitation sonication on the PSD. Soft agglomerates are dispersed by sonication and the mean agglomerate size decreases with sonication. The shift in PSD indicates that the loosely held soft agglomerates are dispersed and ill-formed crystalline bridges between the hard agglomerates may also be broken. A 50% decrease in agglomerate size is seen upon post-precipitation sonication. Well-formed hard agglomerates are however resistant to both shear and sonication.

Figure 3-4 shows the effect of flow rate and feed (iron and hydroxide) concentrations on iron oxide hard agglomerate size. The agglomerate size decreases with flow rate at all reactant concentrations, although influence of flow rate is most pronounced at high $\text{Fe}^{2+}/\text{Fe}^{3+}$ concentration where for a 3-fold increase in flow rate (80 ml/min to 300 mL/min), the agglomerate size drops by 4-folds (800 nm to 200 nm). At high reactant concentration, reaction rates are high but are limited by mixing rate and hence the effect of an increase in mixing

rate (flow rate) is more evident at a high reagent concentration. At low flow rates (< 100 mL/min),; when mixing is slow however, local reactant concentrations are higher making precipitation reaction faster and thus forming denser agglomerates. Similar observations are made with increase in hydroxyl concentration for a constant Fe^{2+}/Fe^{3+} concentration.

Stabilizer addition

Figure 3-5(a) shows that in situ addition of sec.butylamine limit the hard agglomerate size. Sec.butylamine (basic in nature) if pre-mixed with iron stream may react with ferrous-ferric salts prior to neutralization reaction with NaOH. To avoid this possibility, it is premixed with NaOH stream. In situ addition of sec. butylamine allows adsorption of additive molecules on the particle surface during the precipitation process, leading to effective stabilization. Agglomerate size decreases with an increase in additive quantity. Figure 3-5(b) shows the effectiveness of various stabilizers and additive concentrations on hard agglomerate size. For all stabilizers, an increase in concentration leads to a decrease in hard agglomerate size. TEG was found to be most effective in limiting agglomerate size. Glycols form complexes with iron ions and affect the formation and release rate of hydroxide, which slows down supersaturation generation and limits agglomeration. Glycols may also prevent particle agglomeration by covering the particle surface and preventing any close contact between the particles to form material bridges. A 5% (v/v) addition of TEG gives a mean hard agglomerate of 200 nm. No significant improvement in agglomerate size is observed with a further increase in TEG quantity. This indicates that the particle surface is saturated with TEG molecules and any further addition of the stabilizer does not help. A significant change in mixing rate may affect the precipitation reaction and hence hard agglomerate size. Additives other than TEG need to be added in significant quantities before their effect on hard agglomerate size is seen. TEG is expected to perform better than DEG due to longer carbon chain which adds to the steric hindrance when adsorbed over the oxide surface. Under high pH conditions the particles are negatively charged

decreasing the possibility of hydrogen bond formation between the surface and the CO group of the amide, limiting PAM adsorption on particle surface and therefore limiting its stabilization performance. The interaction of sec-butyl with oxide surface is electrostatic in nature. At high pH when oxide surfaces are negatively charged, amine (group) that is positively charged successfully interacts and adsorbs on to the particle surface.

Figure 3-6 shows the effect of TEG concentration on hard agglomerate size for precipitation occurring at varying iron concentrations. No significant effect of TEG quantity is seen on agglomerate size at both low and high flow rate conditions over low iron concentrations (0.01 M and 0.036 M). It is understood that fewer iron oxide particles would need less TEG to stabilize. However, as the iron concentration increases, the number of precipitate particles increase and hence more TEG is required to stabilize them. At a high flow rate (509 mL/min) and high iron concentration (0.18 M), the agglomerate size is seen to increase (2.5 folds) with TEG addition. This could be due to an increase in the collision rate of particles (due to greater turbulence) and insufficient adsorption of the stabilizer molecules on the particle surface due to short mixing time in the reactor.

Figure 3-7 (a) and (b) show the extent of agglomeration with varying TEG additive concentrations at flow rate of 165 mL/min. The primary particles appear less agglomerated at high stabilizer concentration indicating that the stabilizer works at the particle interface. Figure 3-7 (c) and (d) show the effect of TEG additive concentration on hard agglomerate size, primary particle size and PSD at a flow rate of 165 mL/min. Agglomerate size decreases with an increase in additive concentration. A 2-fold decrease in hard agglomerate size is observed for a 10-fold increase in stabilizer concentration. Table 3-3 shows that despite a 10-fold increase (5% v/v to 50% v/v) in stabilizer addition, the primary particle size remains almost constant. This indicates that the particle surface is saturated at 5% (v/v) additive concentration and any further increase in additive quantity has an insignificant effect on both the hard agglomerate and the primary particle size.

Table 3-3 gives a comparison of hard agglomerate size and primary particle sizes obtained with various stabilizers. Dextran has the largest molecular weight, while BA has the smallest. Being a long chain, dextran can cover primary particles limiting their growth but at the same time may also promote flocculation of bigger particles by intertwining them. Other additives have smaller molecular weights and work effectively once the hard agglomerate form, when they adsorb on the particle surface. Dextran gives the smallest primary particle size but largest hard agglomerate size. TEG stabilizes the particles better than PAM because it being a smaller molecule can adsorb faster on the particle surface. It also works better than DEG. TEG having a longer molecular chain than DEG, offers better coverage of the particle surface.

Figure 3-8 shows that in situ addition of dextran shows no decrease in hard agglomerate size at both low and high flow rates. This could be due to a balance between successful adsorption over the particle surface to stabilize the particles but an increase in collision rate promoting agglomeration of particles under high flow rate and turbulent conditions.

Figure 3-9 (a) shows a typical hard agglomerate obtained with dextran and (b) PSD of primary particles in an agglomerate. Comparison with

Table 3-3 shows that the smallest primary particles are obtained with dextran. TEG is observed to give the smallest hard agglomerates whereas the largest hard agglomerates were obtained with Dextran. TEG has a shorter chain structure, which prevents chain-interwining and consequent agglomeration. Increasingly bigger hard agglomerates with dextran could be due to intertwining of the elongated chain structures which may promote agglomeration. Clearer primary particle edges from TEM images indicate that dextran adsorbs on the particle surface.

In situ sonication and geometry modification

Figure 3-10 shows the variation of energy dissipation rate in both axial and radial direction in CIJR (original and modified) obtained using CFD. The mixing volume of the CIJR is slightly modified to accommodate the sonic probe. Energy

dissipation here is estimated in the modified geometry with sonicator switched off. The peak corresponds to the estimated energy dissipation at the impingement point and drops with distance away from it. Energy dissipation in the modified CIJR closely follows the trend for the unmodified geometry but with little variations. The dissipation values in the modified geometry are unchanged across the volume despite a $\sim 7\%$ reduction in mixing volume ($\sim 1.58 \times 10^{-7} \text{ m}^3$). The energy dissipation is observed to increase at the geometry exit due to a narrower outlet pipe and the associated increase in pressure.

Figure 3-11 shows the effect of flow rate and the modified geometry on product yield of the iodide-iodate reaction at varying hydrogen concentrations. At high flow rates and/or low hydrogen concentration, when mixing is efficient, local hydrogen concentration is low and thus a smaller byproduct yield is obtained. Lower yield values are obtained in modified geometry at low flow rates (40 to 165 mL/min) where mixing is slower and is likely to be affected by geometric modification which may affect local hydrodynamics. This indicates that the geometry modification does affect mixing at low flow rates. A negligible effect of geometry is seen on the product yield at flow rates greater than 165 mL/min. Figure 3-12 shows the product yield for the iodide-iodate reaction with varying input sonication power at varying flow rates. There is no significant increase in product yield with an increase in sonication energy, however; a slight increase in product yield is observed at low flow rates of 56 mL/min and 88 mL/min for an energy input of 40W. No appreciable increase in product yield is observed at high flow rates for any degree of sonic energy input. It is concluded that turbulence at high flow rates is sufficient to give high product yield and sonic energy addition does not help any further, despite the high dissipation associated with it (Table 3-4). The power available as sonic energy is dissipated over the mixing volume. Sonic energy, however, does enhance mixing and contributes to this effect at low flow rates. Figure 3-13 (a) shows the effect of post-reaction sonication and in situ sonication on sizes of soft and hard iron oxide agglomerates respectively in the modified geometry. Though soft agglomerate size varies insignificantly with change in geometry, hard

agglomerate obtained in modified geometry is 40% bigger in size than that produced in original mixing geometry. Though post-reaction sonication disperses soft agglomerates, in situ sonication does not help in reducing hard agglomeration. This could be due to an increase in breakage but a greater increase in particle collisions in in-situ sonic conditions that enhance agglomeration. Also a sharp increase in temperature locally in insitu sonic conditions may promote particle sintering and therefore increase in hard agglomerate size. Figure 3-13 (b) shows that in spite of the presence of TEG in situ, hard agglomerate size does not change appreciably with input in situ sonic power. This could be due to a balance between the greater induced breakage and increased collision of agglomerates by sonication. Agglomerate size increase in modified geometry (as compared to unmodified one), and indicates to an increase in collision rate. Also induced sintering due to local temperature (in sonication) may also enhance agglomeration. Figure 3-13 (c) shows that hard agglomerate size decrease insignificantly with in situ sonication in the presence of PAM stabilizer. In situ sonication may promote particle-PAM contact through rapid mixing through the second feed stream, thus reducing the stabilizer adsorption time. PAM is a longer chain molecule than TEG and so it may provide more particle-surface coverage and therefore reduce agglomeration. In situ sonication, however, did not have the expected effect on hard agglomerate size. Table 3-5 shows that though no significant change in primary particle size is observed with in situ sonication in the absence of stabilizer, primary particle size decreases with in situ sonication in the presence of PAM, and increases in the presence of TEG. The additional turbulence induced by sonication may enhance PAM adsorption on particle surface over TEG.

Figure 3-14 shows the primary PSD with and without in situ sonication in the absence of any stabilizer. There is no appreciable change in primary particle size with/out in situ sonication. It is concluded that sonication brings no significant improvement in mixing to that induced by increase in flow rate and that primary particle size (7.1nm and 7.3nm) is not significantly affected. In situ sonication, however may increase interparticle collision and sintering due to

increase in local temperature associated with sonication of fluids. This could lead to an increase in hard agglomerate size, which has been reported earlier.

Conclusions

Iron oxide nanoparticles are prepared through co-precipitation technique. The effect of reactant concentration, flow rate, stabilizer type and concentrations, in situ and post-reaction sonication on iron oxide hard agglomerate and primary particle size is studied.

The hard agglomerate size decreases with an increase in flow rate and small particle agglomerates are precipitated at high reagent concentrations. Soft agglomerates comprising of hard agglomerates are easily dispersed by sonication and see a shift in PSD with a smaller average size. The smallest hard agglomerates are obtained with TEG (5% v/v) added to the reactant stream. Smallest primary particles are however obtained with Dextran (2mM). Stabilizers are found to work best when present in situ and pre-mixed with the reactant stream.

Adsorption time of the stabilizers onto the particle surface is understood to be an important factor in successfully limiting agglomeration and apparently the short residence time at high flow rate (509 mL/min) is insufficient. TEG stabilizer successfully limits agglomeration at low flow rate conditions but fails to work at high flow rate. On the other hand, PAM fails to work at low flow rate or under in-situ sonic conditions (enhanced turbulence). This indicates that stabilizer performance is dependent on the stabilizer functional group and the corresponding adsorption time may also be important. The residence time of the reactor may limit stabilizer adsorption. The limited performance of in situ sonication could be due to a 'transient' balance between the breakage of ill-formed agglomerates and increase in the collision rate with the increase in turbulence. In situ sonication has an insignificant effect on primary particle size in the absence of stabilizer.

In situ sonication promotes micromixing (and higher product yield) at low flow rates, however; at high flow rates the influence is insignificant. Geometry

modification also affects micromixing (and therefore product yield) at low flow rates (< 70 mL/min), where as at high flow rates and in the limit of turbulent flow, insignificant effect on yield is seen. CFD simulations indicate that modified geometry has a similar energy dissipation field as the original geometry. Product yield is sensitive to local mixing conditions that may vary within the geometry.

Tables

Table 3-1: Effect of flow rates and reactant concentrations on iron oxide mean agglomerate and primary particle sizes.

Flow rate (mL/min)	[Fe ²⁺]/[Fe ³⁺] (M/M)	[OH ⁻] (M)	Hard agglomerate mean diameter (nm)	Primary particle mean diameter (median diameter) (nm)
63	0.18/0.36	1	907	9.75* (9.2)
165	0.18/0.36	1.45	623	7.1 (6.9)
509	0.18/0.36	1.45	298	12.4 [#] (10.6)
509	0.036/0.072	1.45	1072	7.6 (7.4)
509	0.01/0.02	1.45	1333	6 (5.8)
509	0.18/0.36	1	872	8.82 (8.84)

* standard deviation = 3.5, [#] standard deviation = 5.3 and others < 2

Table 3-2: Reagent concentrations for iodide-iodate reaction

Feed stream (inlet)	Reagent	Conc. 1 (M)	Conc. 2 (M)
1	I ⁻	0.0234	0.0234
1	IO ₃ ⁻	0.00466	0.00466
1	H ₂ BO ₃ ⁻	0.1818	0.1818
2	H ⁺	0.0936	0.1818

Table 3-3: Effect of stabilizers (added in situ) on iron oxide mean agglomerate and primary particle sizes. $[\text{Fe}^{2+}] = 0.18 \text{ M}$, $[\text{Fe}^{3+}] = 0.36 \text{ M}$ and $[\text{OH}^-] = 1.45 \text{ M}$ and flow rate = 165 mL/min for all experiments.

Stabilizer (added in situ)	Hard agglomerate mean diameter (nm)	Primary particle mean diameter (median diameter) (nm)
Triethylene glycol (5% v/v)	230	8.44 (7.95)
Triethylene glycol (11% v/v)	303	5.84 (5.64)
Triethylene glycol (50% v/v)	125	9.50 (7.35)
sec. Butylamine (5% v/v)	609	-
Dextran (2mM)	681	4.72 (4.4)
Diethylene glycol (10% v/v)	816	8.12 (7.92)
Polyacrylamide (2% v/v)	989	7.68 (7.35)
None	623	7.1 (6.91)

Table 3-4: Energy dissipation and Energy density in insitu sonication in CIJR

Input energy (W)	Power dissipated (W)	Energy dissipation (W/kg)
0	0	0
40	20	1.17×10^5
80	40	2.35×10^5
120	60	3.53×10^5
160	80	4.7×10^5

Table 3-5: Effect of in situ sonication on iron oxide agglomerate and primary particle size with/out in-situ added stabilizer. $[\text{Fe}^{2+}] = 0.18 \text{ M}$, $[\text{Fe}^{3+}] = 0.36 \text{ M}$, $[\text{OH}^-] = 1.45 \text{ M}$ and flow rate = 165 mL/min in all experiments.

	Hard agglomerate mean diameter (nm)		Primary particle mean (median) diameter (nm)	
	No in-situ sonication	160 W input in-situ sonic power	No in-situ sonication	160 W input in-situ sonic power
No stabilizer	1017	1145	7.1 (6.9)	7.3 (7.04)
5% (v/v) TEG	979	1232	8.44 (7.95)	9.5 (8.96)
5.6% (v/v) PAM	768	470	9.2 (8.8)	8.2 (8.05)

Figures

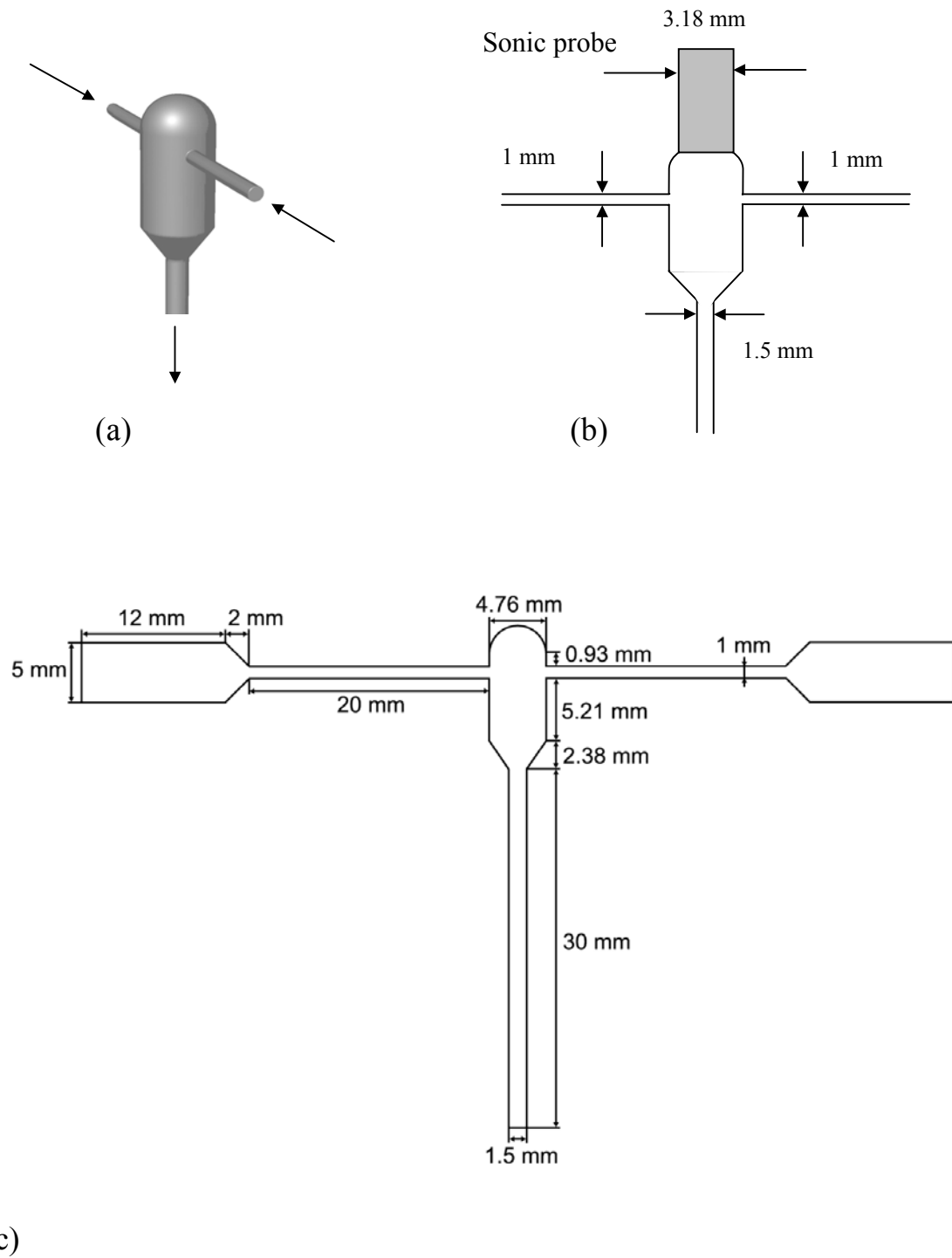


Figure 3-1: Isometric view of CIJR and its dimensions

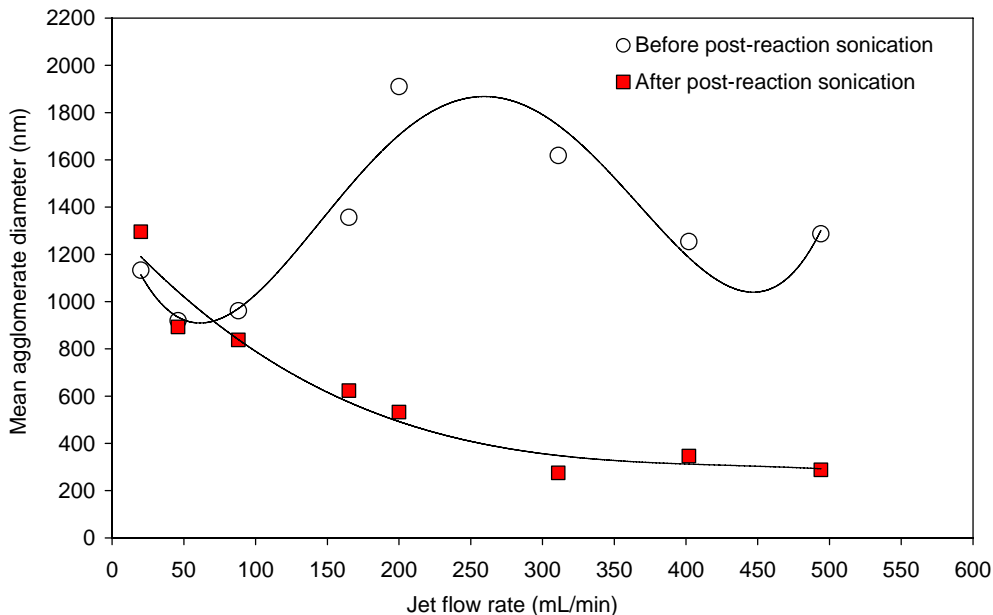


Figure 3-2: Effect of post-reaction sonication on iron oxide agglomerate size. $[\text{Fe}^{2+}] = 0.18 \text{ M}$, $[\text{Fe}^{3+}] = 0.36 \text{ M}$ and $[\text{OH}^-] = 1.45 \text{ M}$ in all experiments.

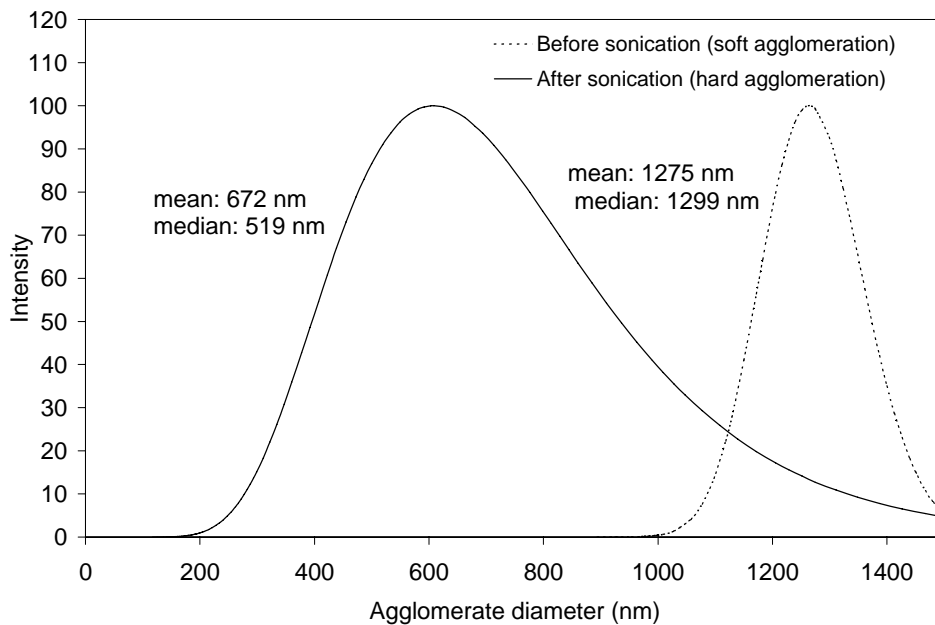
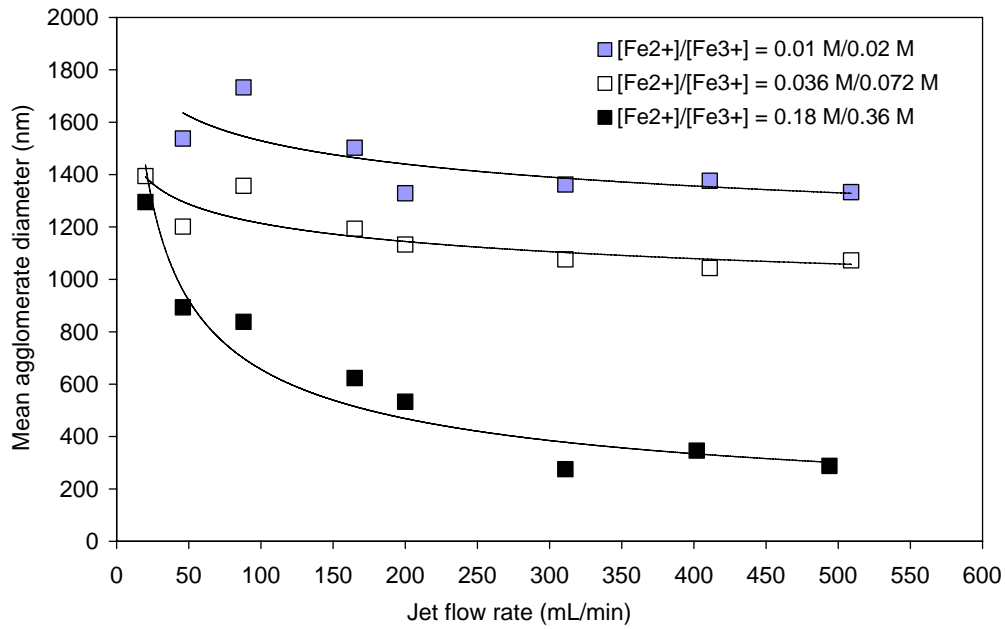
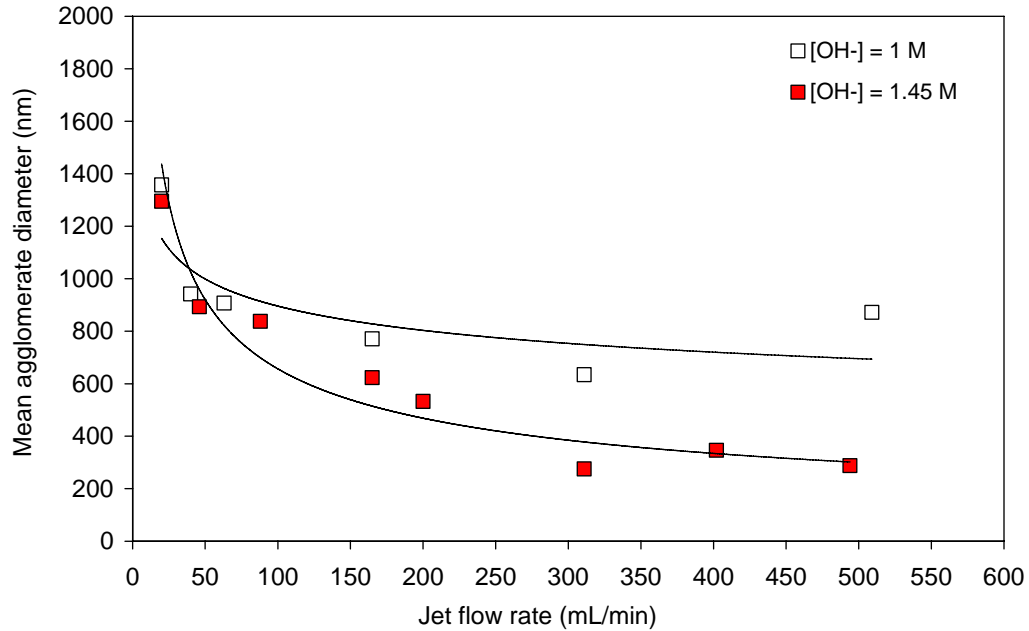


Figure 3-3: Effect of post-reaction sonication on iron oxide agglomerate PSD. $[\text{Fe}^{2+}] = 0.18 \text{ M}$, $[\text{Fe}^{3+}] = 0.36 \text{ M}$, $[\text{OH}^-] = 1.45 \text{ M}$ and flow rate = 165 mL/min in the experiment.

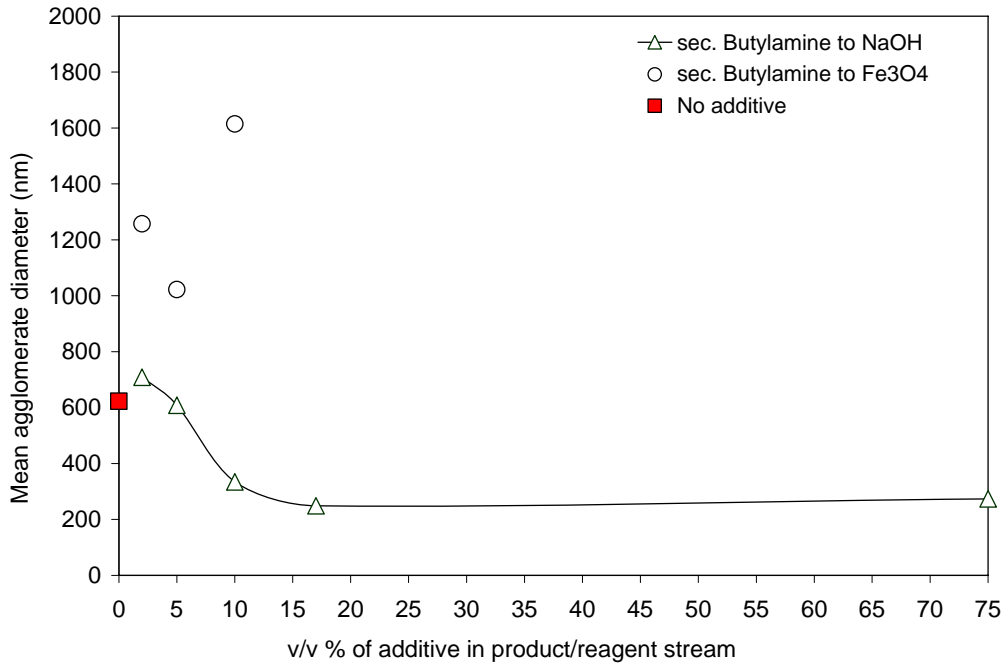


(a)

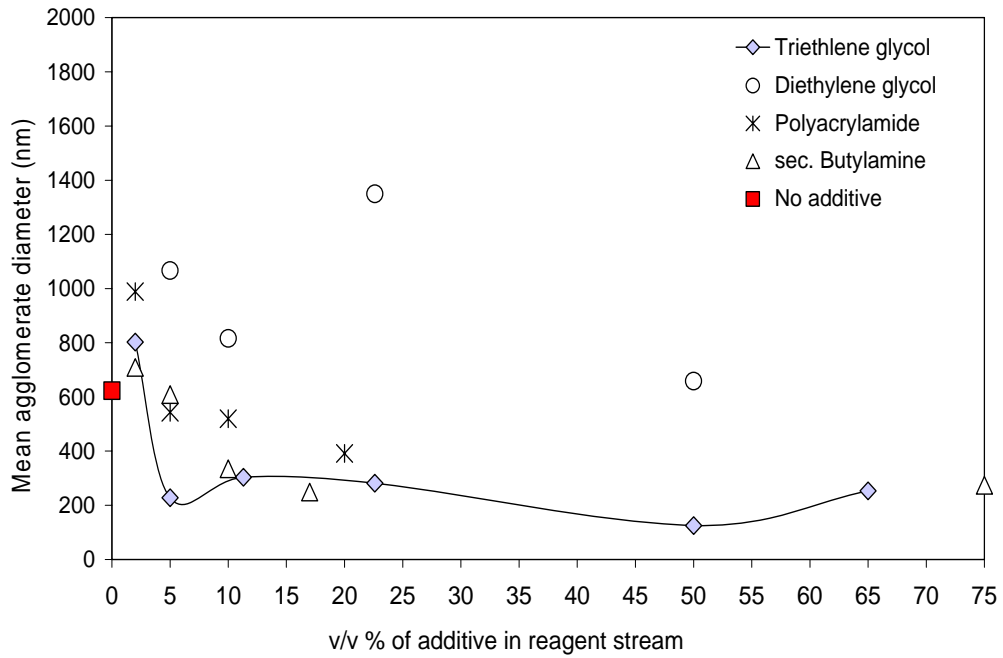


(b)

Figure 3-4: Effect of jet flow rate and reactant concentrations on iron oxide particle size at (a) varying $[\text{Fe}^{2+}]$ and $[\text{Fe}^{3+}]$ and (b) varying $[\text{OH}^-]$. $[\text{OH}^-] = 1.45 \text{ M}$ in (a) and $[\text{Fe}^{2+}] = 0.18 \text{ M}$ and $[\text{Fe}^{3+}] = 0.36 \text{ M}$ in (b).

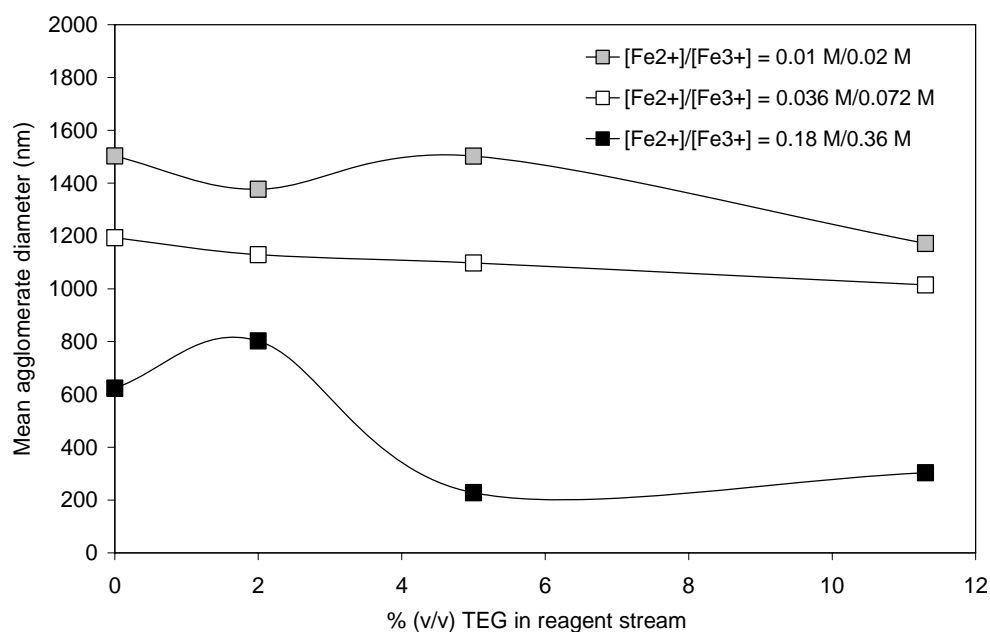


(a)

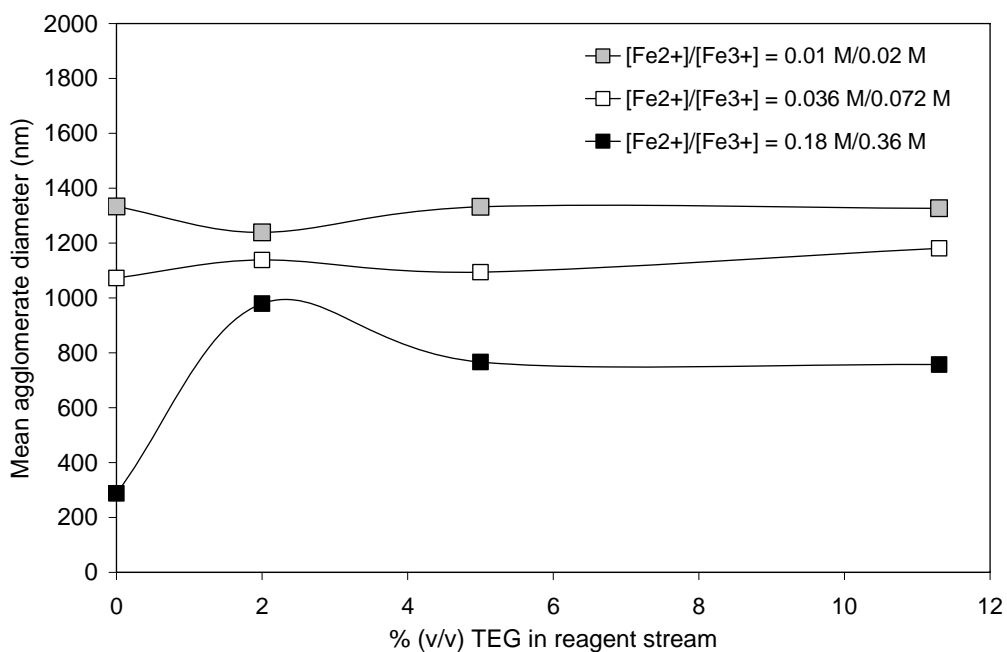


(b)

Figure 3-5: Effect of (a) point of stabilizer addition and (b) various stabilizers and concentrations added in situ (to NaOH stream) on iron oxide agglomerate size. $[\text{Fe}^{2+}] = 0.18 \text{ M}$, $[\text{Fe}^{3+}] = 0.36 \text{ M}$, $[\text{OH}^-] = 1.45 \text{ M}$ and flow rate = 165 mL/min in all experiments.

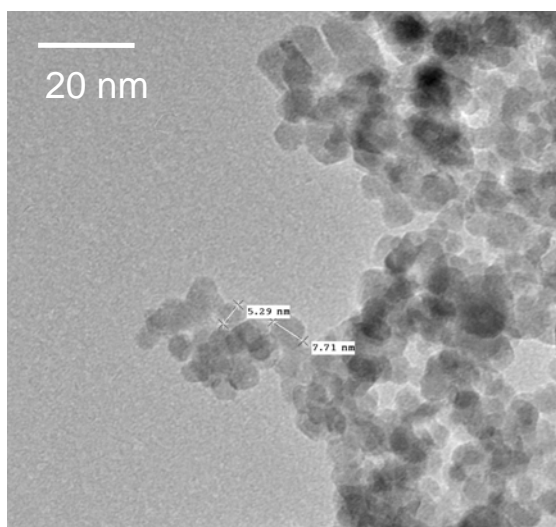


(a)

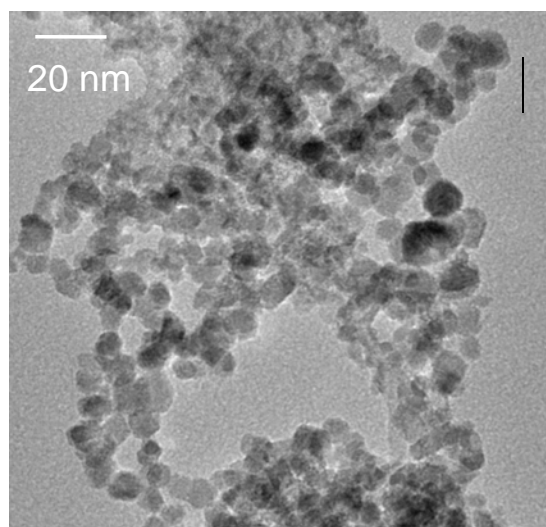


(b)

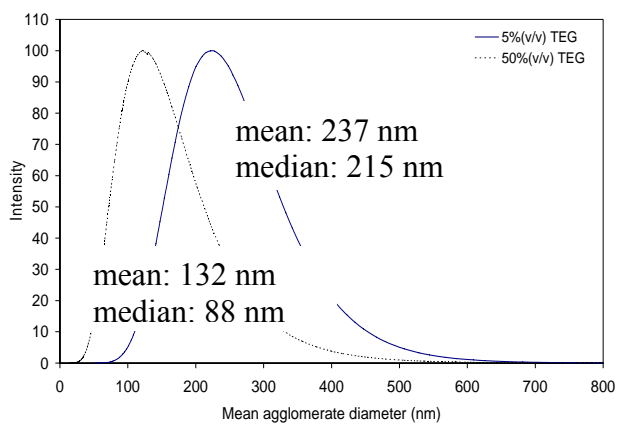
Figure 3-6: Effect of triethylene glycol v/v (added in situ) on iron oxide hard agglomerate size at (a) flow rate = 165 mL/min and (b) flow rate = 509 mL/min. $[OH^-] = 1.45 \text{ M}$ in all experiments.



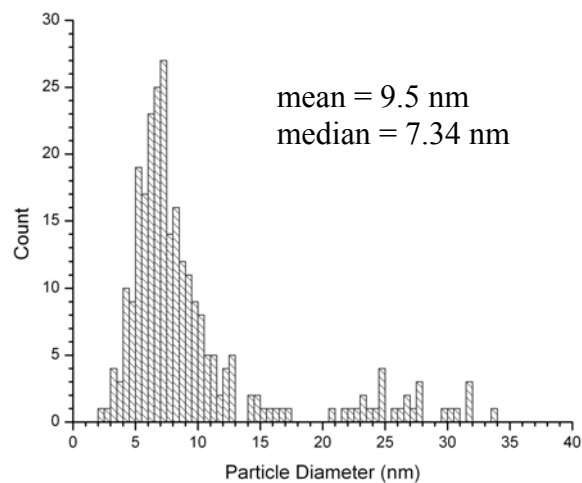
(a)



(b)



(c)



(d)

Figure 3-7: Effect of triethylene glycol (TEG) added in situ on iron oxide particle size and morphology: (a) TEM image at [TEG] = 5% (v/v), (b) TEM image at [TEG] = 50% (v/v), (c) agglomerate PSD for [TEG] = 5% and 50% (v/v) and (d) primary PSD for [TEG] = 50% (v/v). [Fe²⁺] = 0.18 M, [Fe³⁺] = 0.36 M, [OH⁻] = 1.45 M and flow rate = 165 mL/min in all experiments.

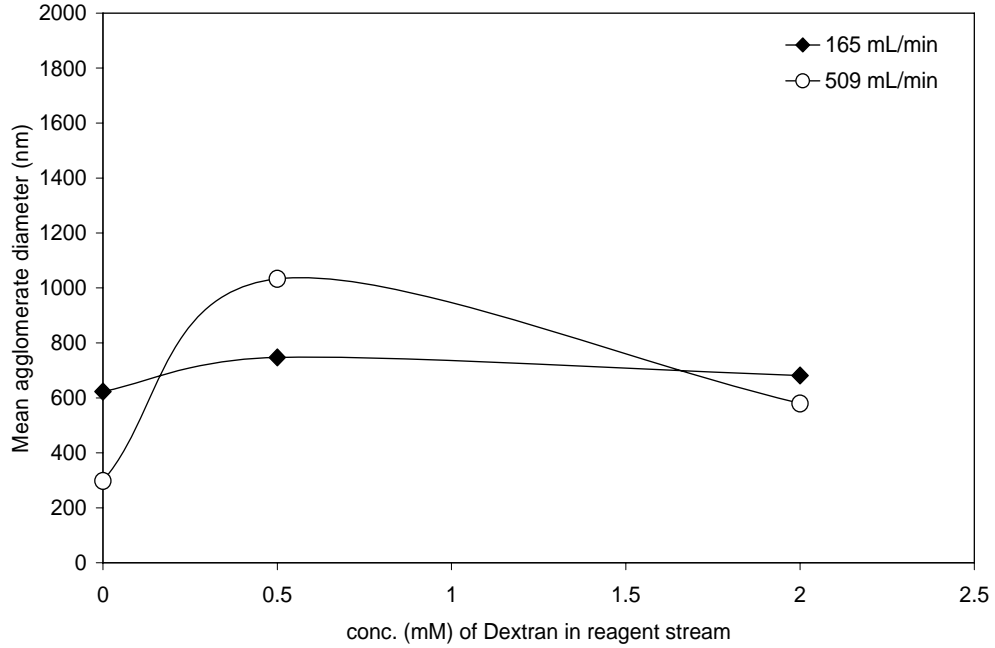
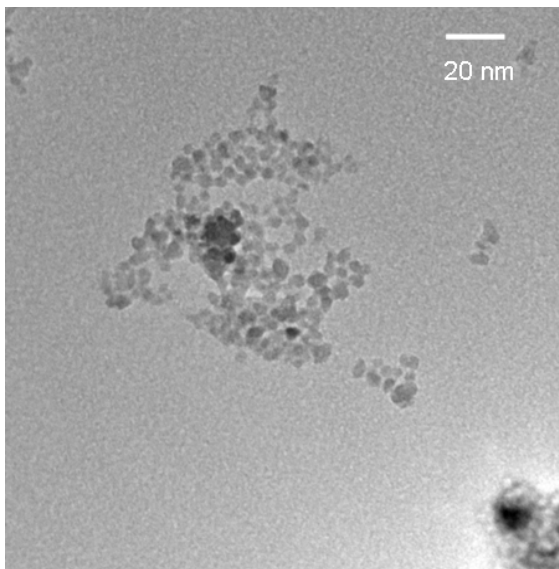
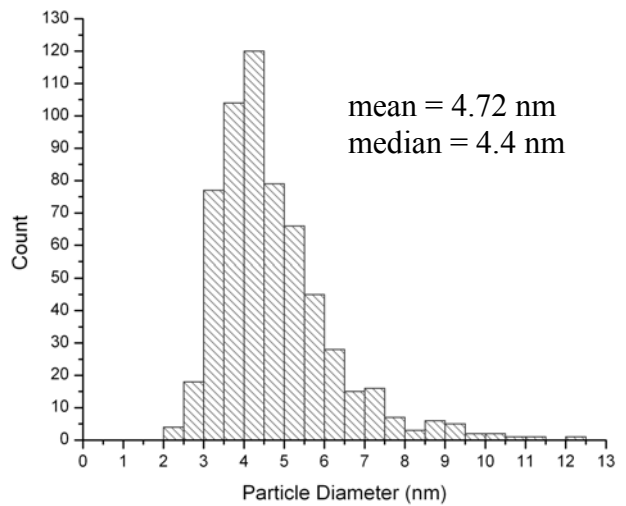


Figure 3-8: Effect of dextran added in situ on iron oxide agglomerate size at $[\text{Fe}^{2+}] = 0.18 \text{ M}$, $[\text{Fe}^{3+}] = 0.36 \text{ M}$ and $[\text{OH}^-] = 1.45 \text{ M}$ for all experiments.

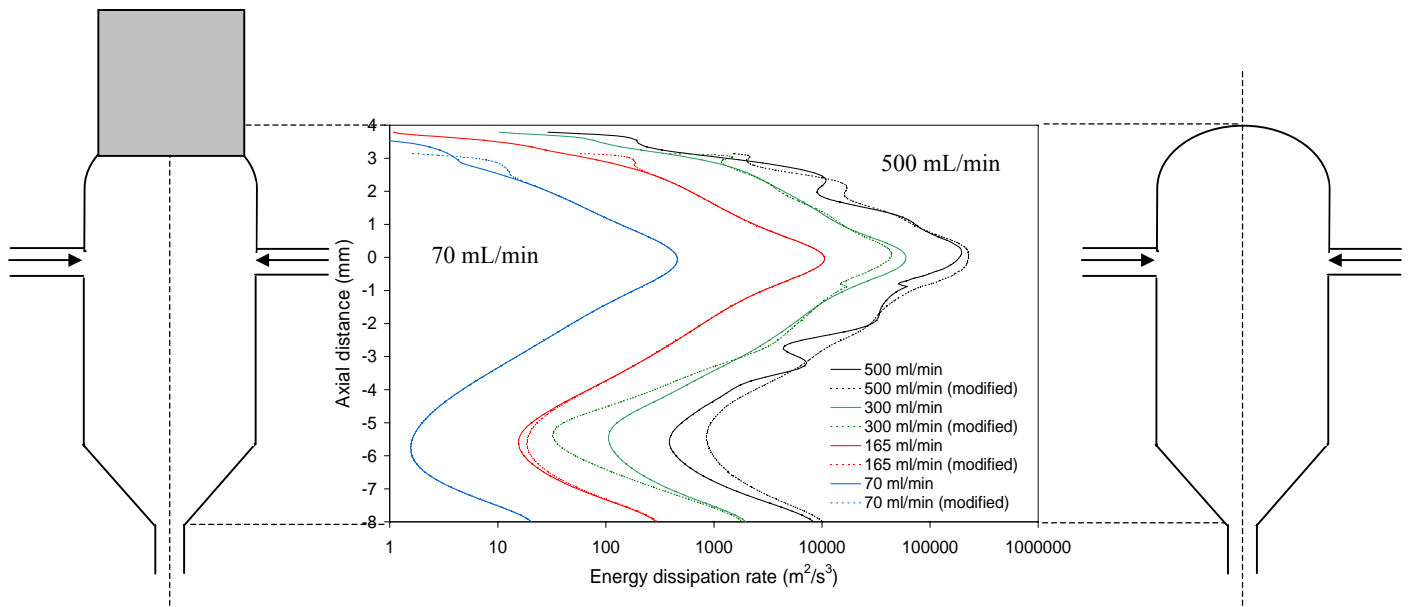


(a)

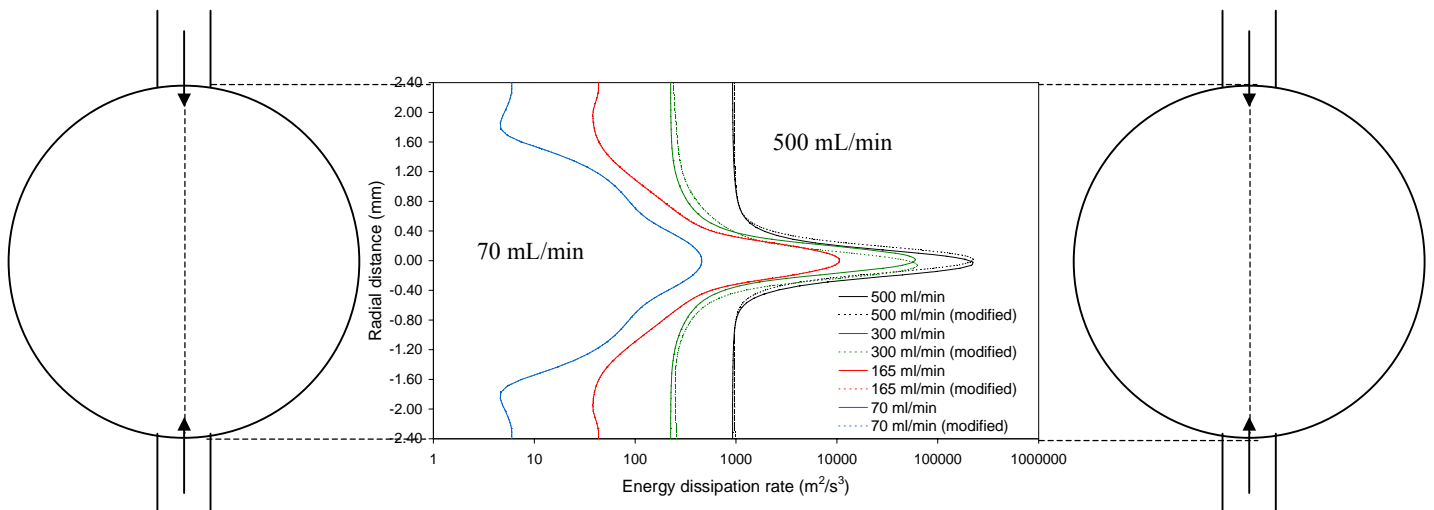


(b)

Figure 3-9: Effect of Dextran added in situ on iron oxide morphology and primary particle size: (a) TEM image and (b) primary PSD. $[\text{Dextran}] = 2 \text{ mM}$ and flow rate = 165 mL/min in all experiments.



(a)



(b)

Figure 3-10: Variation of energy dissipation rate in (a) axial direction and (b) radial direction at various jet flow rates. The origin is placed at the impingement point.

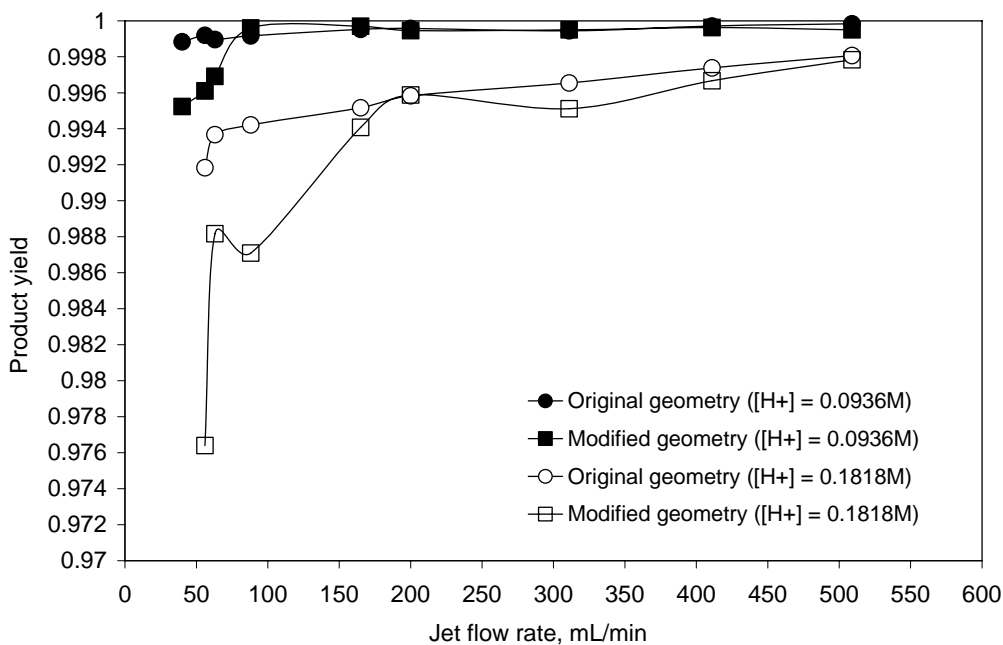


Figure 3-11: Effect of jet flow rate and modified geometry on product yield in iodide-iodate reaction. $[H_2BO_3^-] = 0.1818M$ in all experiments.

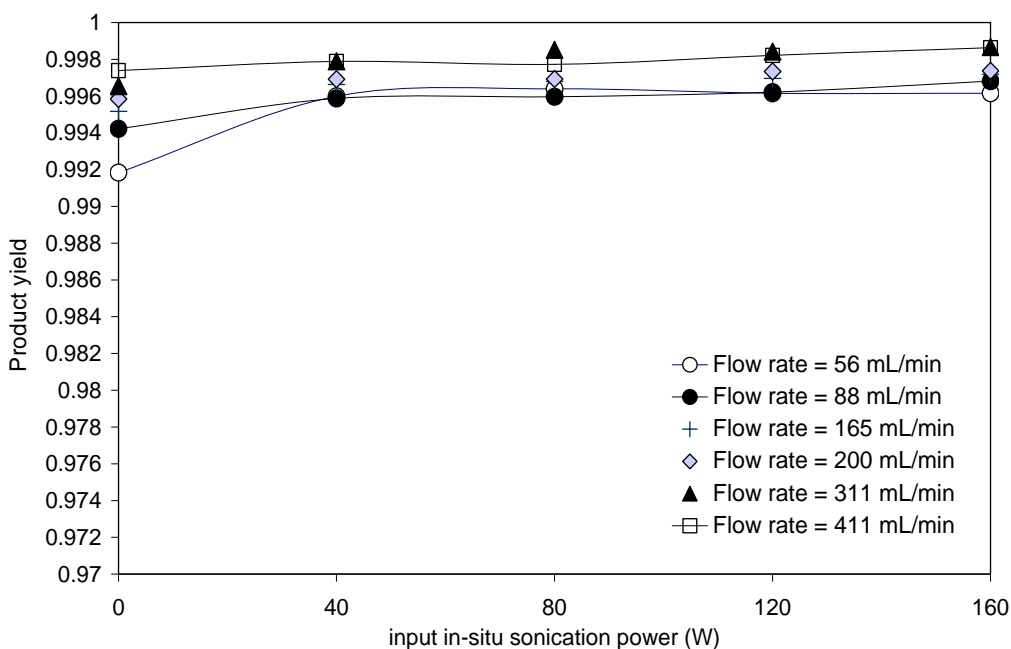
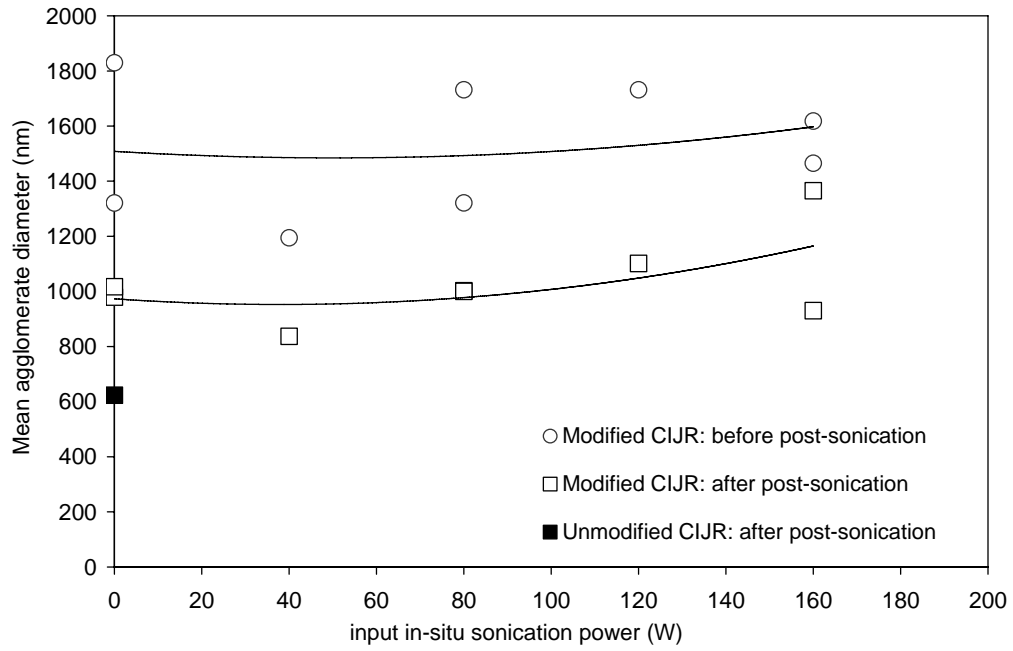
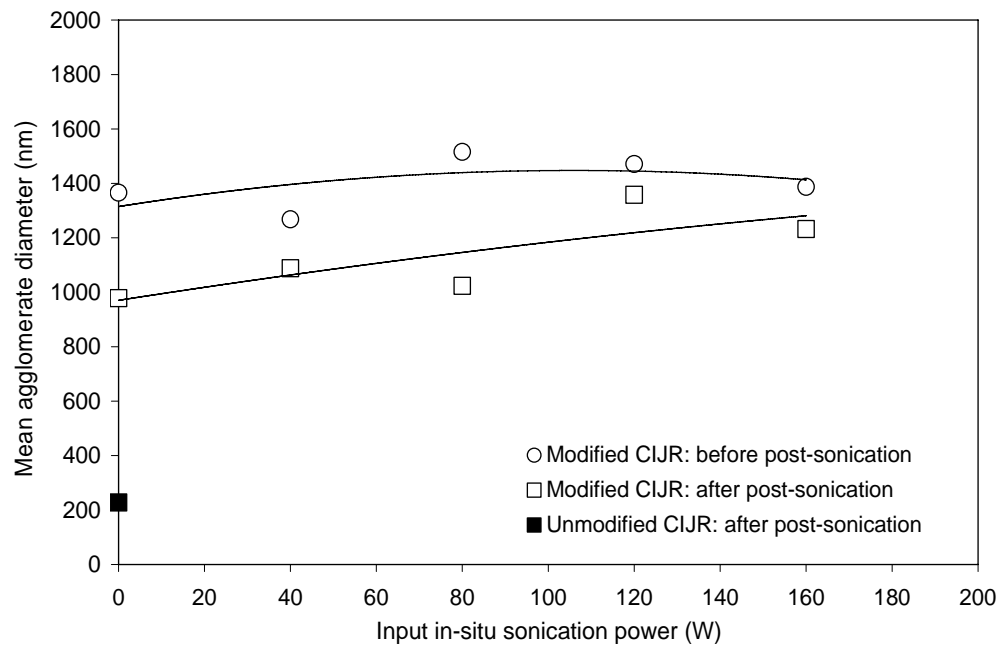


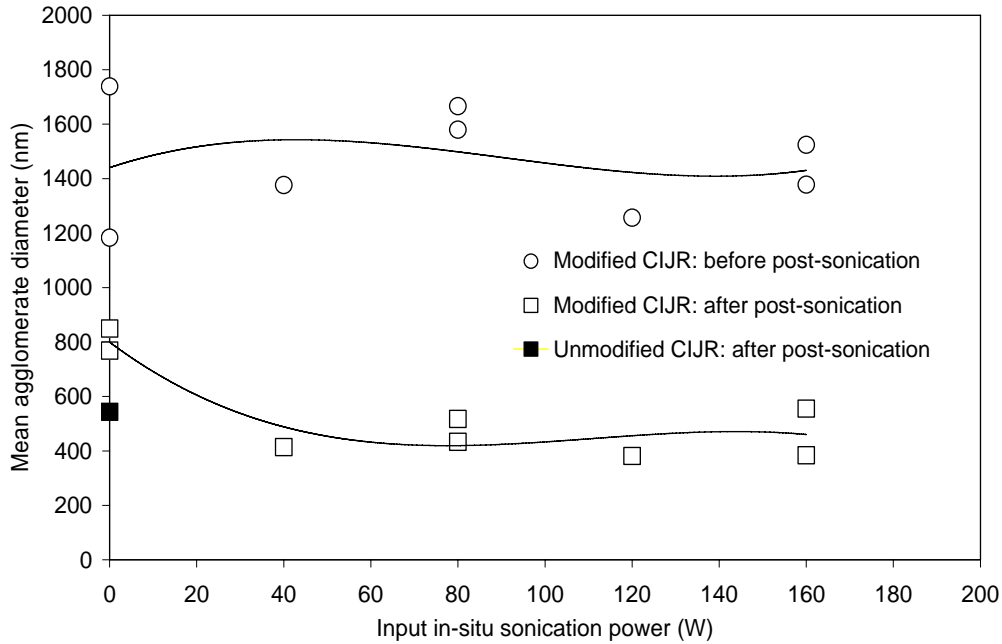
Figure 3-12: Effect of in situ sonication on product yield in iodide-iodate reaction. $[H^+] = 0.1818M$ and $[H_2BO_3^-] = 0.1818M$ in all experiments.



(a)

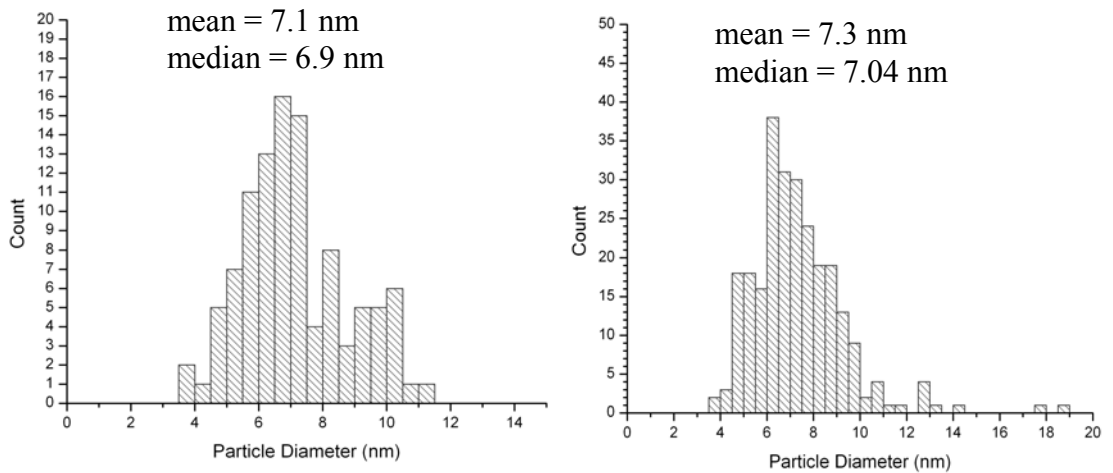


(b)



(c)

Figure 3-13: Effect of in-situ sonication and stabilizer (added in situ) (a) no stabilizer, (b) 5% v/v triethylene glycol (TEG) and (c) 5% v/v polyacrylamide (PAM) on iron oxide agglomerate size. $[\text{Fe}^{2+}] = 0.18 \text{ M}$, $[\text{Fe}^{3+}] = 0.36 \text{ M}$, $[\text{OH}^-] = 1.45 \text{ M}$ and flow rate = 165 mL/min in all experiments.



(a)

(b)

Figure 3-14: Primary PSD in a hard agglomerate (a) with no in situ sonication and (b) 160 W input in situ sonication. $[\text{Fe}^{2+}] = 0.18 \text{ M}$, $[\text{Fe}^{3+}] = 0.36 \text{ M}$, $[\text{OH}^-] = 1.45 \text{ M}$ and flow rate = 165 mL/min in all experiments.

Literature cited

- Bajpai, A.K. and S.K. Bajpai, 1995, *Kinetics of Polyacrylamide Adsorption at the Iron Oxide – Solution Interface*, Colloids and Surfaces A: Physicochemical and Engineering Aspects, **101**, 21-28.
- Banert, T., G. Brenner and U.A. Peuker, 2006, *Operating Parameters of a Continuous Sono-Chemical Precipitation Reactor*, AIChE Meeting, USA.
- Beattie, J.K., 1989, *Monodisperse Colloids of Transition Metal and Lanthanide Compounds*, Pure & Appl. Chem., **61 (5)**, 937-941.
- Dutz, S., W. Andrä, R. Hergt, R. Müller, C. Oestreich, C. Schmidt, J. Töpfer, M. Zeisberger and M. Bellemann, 2007, *Influence of Dextran Coating on the Magnetic Behaviour of Iron Oxide Nanoparticles*, Journal of Magnetism and Magnetic Materials, **311**, 51-54.
- El-Khoury, J.M., Caruntu, D., O'Connor, C.J., Jeong, K., Cheng, S.Z.D. and J. Hu, 2007, *Poly(allylamine) Stabilized Iron Oxide Magnetic Nanoparticles*, **9**, 959-964.
- Faivre, D., P. Agrinier, N. Menguy, P. Zuddas, K. Pachana, A. Gloter, J.Y. Laval and F. Guyot, 2004, *Mineralogical and Isotropic Properties of Inorganic Nanocrystalline Magnetites*, Geochimica et Cosmochimica, **68 (21)**, 4395-4403.
- Furusawa, K., Z. Shou and N. Nagahashi, 1992, *Polymer Adsorption on Fine Particles; the Effects of Particle Size and its Stability*, Colloid Polym Sci, **270**, 212-218.
- Goia, D.V., 2004, *Preparation and Formation Mechanisms of Uniform Metallic Particles in Homogeneous Solutions*, J. Mater. Chem., **14**, 451-458.
- Goia, D.V. and E. Matijević, 1998, *Preparation of Monodispersed Metal Particles*, New J. Chem., **11**, 1203-1215.
- Goia, D.V. and E. Matijević, 1998, *Preparation of Monodispersed Metal Particles*, New J. Chem., **11**, 1203-1215.

- Gupta, A.K. and M. Gupta, 2005, *Synthesis and Surface Engineering of Iron Oxide Nanoparticles for Biomedical Applications*, *Biomaterials*, **26**, 3995-4021.
- Hong, R.Y., S.Z. Zhang, Y.P. Han, H.Z. Li, J. Ding and Y. Zheng, 2006, *Preparation, Characterization and Application of Bilayer Surfactant-Stabilized Ferrofluids*, *Powder Technology*, **170**, 1-11.
- Hong, R.Y., B. Feng, L.L. Chen, G.H. Liu, H.Z. Li, Y. Zheng and W.D. Wei, 2008, *Synthesis, Characterization and MRI Application of Dextran-Coated Fe₃O₄ Magnetic Nanoparticles*, *Biochemical Engineering Journal*, **42**, 290-300.
- Johnson, B.K., 2003, *Flash NanoPrecipitation of Organic Actives via Confined Micromixing and Block Copolymer Stabilization*, Ph.D. Thesis, Princeton University, Volume 1 and 2.
- Johnson, B.K. and R.K. Prud'homme, 2003, *Chemical Processing and Micromixing in Confined Impinging Jets*, *AIChE Journal*, **49 (9)**, 2264-2282.
- Jolivet, J.P., Tronc, E. and C. Chanéac, 2002, *Synthesis of Iron Oxide Based Magnetic Nanoparticles and Composites*, *C. R. Chimie*, **5**, 659-664.
- Lin, C.L., C.F. Lee and W.Y. Chui, 2005, *Preparation and Properties of Poly(acrylic acid)Oligomer Stabilized Superparamagnetic Ferrofluid*, *Journal of Colloid and Interface Science*, **291**, 411-420.
- Maity, D. and D.C. Agrawal, 2007, *Synthesis of Iron Oxide Nanoparticles Under Oxidizing Environment and their Stabilization in Aqueous and Non-Aqueous Media*, *Journal of Magnetism and Magnetic Materials*, **308**, 46-55.
- Marchisio, D.L., L. Rivautella and A. Barreri, 2006, *Design and Scale-Up of Chemical Reactors for Nanoparticle Precipitation*, *AIChE J.*, **52 (5)**, 1877-1887.
- Matijević, E., 1991, *Preparation and Properties of Well Defined Finely Dispersed Metals*, *Faraday Discussion*, **92**, 229-239.

- Matijević, E. and Š. Cimaš, 1987, *Formation of Uniform Colloidal Iron (III) Oxide in Ethylene Glycol-Water Solutions*, *Colloid & Polymer Sci*, **265**, 155-163.
- McGuire, M.J., Addai-Mensah, J. and Bremmell, K.E., 2006, *Spectroscopic Investigation of the Adsorption Mechanisms of Polyacrylamide Polymers onto Iron Oxide Particles*, *Journal of Colloid and Interface Science*, **299**, 547-555.
- Mersmann, A., M. Angerhöfer and J. Franke, 1994, *Controlled Precipitation*, *Chem. Eng. Technology*, **17**, 1-9.
- Monnier, H., A.M. Wilhelm and H. Delmas, 1999, *The influence of ultrasound on micromixing in a semi-batch reactor*, *Chemical Engineering Science*, **54**, 2953-2961.
- Schwarzer, H.C., and W. Peukert, 2002, *Experimental Investigation into the Influence of Mixing on Nanoparticle Precipitation*, *Chem. Eng. Technol*, **25** (6), 657-661.
- Siddiqui, S.W., 2009, *Use of the Confined Impinging Jet Reactor for Production of Nanoscale Iron Oxide Particles*, PhD Thesis, University of Alberta, Canada.
- Siddiqui, S.W., Y. Zhao, A. Kukukova and S.M. Kresta, 2009, *Mixing Characteristics of a Confined Impinging Jet Reactor: Dissipation Rate, Homogeneous and Heterogeneous Reactions, and Effect of Unequal Flowrates on Performance*, *Ind. Eng. Chem. Res.* (Article in Press)
- Teng, X. and H. Yang, 2004, *Effects of Surfactants and Synthetic Conditions on the Sizes and Self-Assembly of Monodisperse Iron Oxide Nanoparticles*, *J. Mater. Chem.*, **14**, 774-779.
- Tronc, E., P. Belleville, J.P. Jolivet and J. Livage, 1992, *Transformation of Ferric Hydroxide into Spinel by Fe^{II} Adsorption*, *Langmuir*, **8**, 313-319.
- Unwin, P. J., M.E. Rusnacik, S.M. Kresta and A.E. Nelson, 2008, *Effect of Amine and Thiol Addition on the Surface Chemistry and Agglomeration of*

Fine Cu Powders, Colloids and Surfaces A: Physicochem. Eng. Aspects,
325, 72-80.

Xu, Z. and G. Yunli,, 2001, Magnetic Nanoparticles for Bioseparation
Application and Methods for Producing Same, US Patent filed.

Chapter 4

Nucleation, Particle Growth and Agglomeration Mechanisms of Nanoparticles in a Fast Precipitation Reaction in Confined Impinging Jet Reactor

Introduction

Due to the ever-growing interest in inorganic nanoparticles, synthesis methods like thermal decomposition, chemical reduction and flame synthesis have been proposed, but these methods require high temperatures and controlled-atmospheric conditions. Chemical precipitation; however, proceeds at ambient conditions of temperature and pressure.

The purpose of this work is to develop an understanding of the interactions between mixing, nucleation, particle growth, and agglomeration of nanoparticles in a fast precipitation reaction. Iron oxide (Fe_3O_4) has been chosen as a model system, with the aim of designing a fast and efficient synthesis process for nanoparticle manufacture.

In a precipitation reaction, nanoparticles form as a result of aggregation of atoms into clusters, called embryos (Goia, et al., 1998). These embryos associate and dissociate until they reach a thermodynamically favored (stable) state and a critical size when they separate from the solution as solid particles, the nuclei. Here the change in enthalpy from solution to the equilibrium phase is balanced by the energy required to produce new surface area as a result of nucleation. These nuclei then grow to primary particles under the effect of supersaturation in the reactor and as these primary particles have a large surface free energy, they tend to agglomerate.

A hard agglomerate consists of many discrete primary particles bound together by hard bridges. A typical primary particle size (d_p) is a few nanometers in size ($\sim 7\text{nm}$), while the hard agglomerate size could range from 200-2000nm. The primary particle size, local reactant concentration and the mixing conditions affect the hard agglomerate size (d_{HA}) which in turn is a more complex function

of collision frequency, the agglomeration efficiency of primary particles, agglomerate breakage under intense mixing conditions and shear. The morphology of the hard agglomerates is somewhat random, whereas the primary particles are polyhedral in shape. Hard agglomerates often form loose structures, known as soft agglomerates that can be broken under shearing or sonication. Hard agglomerates, however; are resistant to both shearing and sonication. Particle agglomeration is a complex phenomenon where the agglomeration phenomena can be explained using three models: Brownian, laminar, and turbulent shear, all of which operate at various length scales. These models are discussed later.

Precipitation processes such as reactive crystallization have been studied by many researchers including Marcant and David (1991), Mersmann (1995) and Schwarzer et al. (2004). Reactive precipitation is a complex process which involves several intermediate steps: mixing, reaction and crystallization (primary and secondary nucleation, particle growth, Oswald ripening), agglomeration and agglomerate-breakage. Mixing may have an effect on both reaction and crystallization rates if they are of the same order of magnitude as the mixing time (Mersmann, 1995). Schwarzer et al. (2002, 2004) reported that the competition between these processes during the precipitation reaction may have profound effects on particle size, particle size distribution, particle morphology (Goia and Matijević, 1998) and aggregation (Jolivet et. al, 2002); and may influence optical, magnetic, electric, adsorptive, and catalytic properties. These property changes tend to be due to the increasing influence of surface properties over the bulk properties with a decrease in particle size.

Nucleation occurs under high supersaturation conditions. This condition is brought about by efficient micromixing. Lieser (1969) reported that supersaturation is strongly dependent on local reactant concentration: higher numbers of fine particles were obtained with concentrated reactive solutions. Nielsen (1964) reported that under complete mixing conditions, reactant concentrations would be uniform throughout the mixing volume and the nucleation rate would be the same everywhere, however; if mixing were slower

than the reaction rate, inhomogeneity in local reactant concentration would occur and cause variation in local nucleation rate and the number of nuclei. When the molar concentration of the precipitate particles become significant heterogeneous nucleation follows homogeneous nucleation (Marcant and David, 1991). Marcant and David (1991) argued that primary (homogeneous) nucleation varied strongly with local mixing conditions; whereas growth, secondary (heterogeneous) nucleation and agglomeration were dependent on the average conditions in the vessel.

The nucleation time is very short and is followed by particle growth and subsequent agglomeration (bridge formation) under lower supersaturation conditions. Both nucleation and particle-growth are strongly dependent on the build-up and discharge of local supersaturation in a given mixing time (Schwarzer et al., 2002 and 2004). Nuclei continue to grow as long as supersaturation remains (Marcant and David, 1991). Marcant and David (1991) state that nucleation consumes a small amount of solute and hypothesized that most of the solute is consumed in the subsequent particle growth, which is largely diffusional and influenced by mixing (Nyvlt et al., 1985). However, as mixing promotes nucleation, efficient mixing would lead to higher nucleation rates and therefore less reactant available for particle growth and agglomeration, limiting both primary particle size and hard agglomerate size under low to medium supersaturation conditions. Fluid mixing brings about buildup of local supersaturation and thus may make the nucleation step dominant over growth, particularly under low supersaturation conditions. Under very high supersaturation, as is the case in this work nucleation, particle growth and agglomeration may compete together at similar rates. Mixing affects the spatial distribution of supersaturation, which in turn determines local nucleation rates and affects particle growth and agglomeration processes (Baldyga and Jasińska, 2004).

Although precipitation reactions have traditionally been carried out in stirred tanks, impinging jets have caught attention over the last decade due to their fast mixing and high mixing intensity characteristics. Paul et al. (2004) reviewed

early work on impinging jets for industrial (Midler et al., 1994) and laboratory scale (Mahajan and Kirwan, 1996; Benet et al., 1999 and Condon, 2001) applications. Confined impinging jets have recently been used in organic (Johnson et al. 2003) and inorganic nanoparticle synthesis (Marchisio et al., 2006). Figure 4-1 shows the geometry of the CIJR. The local energy dissipation rate (indicative of mixing intensity) in the CIJR is several orders of magnitude higher than in a stirred tank (Siddiqui et al., 2009). The shorter residence time and large energy dissipation in the CIJR are expected to limit particle growth and support a narrower PSD. Given the complexity of a precipitation reaction with the growth and agglomeration processes which follow, it is important to develop a good understanding of the degree of interaction of the various mechanisms (mixing, nucleation, particle growth and agglomeration), and to identify the factors that influence the final hard agglomerate size. A hard agglomerate shown in Figure 4-2 is made up of primary particles. Figure 4-3 depicts a proposed model of the nucleation, growth and agglomeration process with intermediate steps discussed in detail in the sections below.

Theory

The production of nanoparticle agglomerate by reactive precipitation can be simplified to the supersaturation generation process initiated by mixing, which feeds nucleation and growth of primary particles in parallel with interparticle growth and particle agglomeration. These events, although simplified to a step-by-step process here, occur simultaneously. The concepts of classical precipitation theory were developed for batch crystallization processes occurring under low to moderate supersaturation. They are extended in this work to the iron oxide precipitation system under high supersaturation conditions.

- (i) Mixing and its influence on supersaturation and nucleation.
- (ii) Growth of nuclei to primary particles.
- (iii) Agglomeration of primary particles to form hard agglomerates.

Mixing, supersaturation and nucleation

To obtain nanoparticles through a fast precipitation reaction, high supersaturation is necessary. Fast mixing in a fast precipitation reaction generates high local supersaturation, inducing rapid nucleation and facilitating small particle precipitation (Mersmann, 1995; Schwarzer and Peukert, 2004; Roelands et al., 2003 and Gavi et al., 2007a). Supersaturation is created by mixing controlled chemical reaction and is reduced by precipitation (Baldyga and Jasińska, 2004). Mixing also determines the spatial distribution of supersaturation and it therefore influences the precipitate PSD (Schwarzer et al., 2004). At high local supersaturation, primary (homogenous) nucleation dominates the nucleation mechanism (Schwarzer et al., 2002 and 2004). Supersaturation drops with nucleation and is subsequently discharged through particle growth. The driving force for particle nucleation and growth is, thus, the build-up and discharge of local supersaturation in a given mixing time. The rise in supersaturation is determined by the mixing intensity. Energy dissipation is a measure of the mixing intensity and is much larger in the CIJR (Siddiqui et al., 2009). Smaller particles are therefore expected in the CIJR.

Nucleation is strongly dependent on the interfacial energy as well as on supersaturation. An increase of the interfacial energy can decrease the nucleation rate substantially (Schwarzer et al., 2004), however; in the present study interfacial energy is assumed to be constant, and the change is neglected.

Gavi et al. (2007a) modeled barium sulfate precipitation in CIJR and observed that high local-supersaturation occurred in regions with higher turbulence, and that the volume-averaged supersaturation increased with mixing. It was also observed that nucleation was more strongly influenced by supersaturation than growth, and thus high supersaturation conditions favored nucleation over growth and facilitated smaller particle precipitation. Gavi et al. (2007b) showed that a 1.25 fold increase in local-supersaturation (at the impingement point) increased nucleation by 9-fold, and a 25-fold increase in jet Reynolds number (100 to 2500) caused a drop in average particle (aggregate) size from 1 micron to 100 nm in the CIJR.

In this work we assume that complete mixing precedes nucleation and that nucleation occurs at a constant supersaturation level. However this assumption may not hold in reality because according to Roelands et al. (2003), precipitation of insoluble compounds at high supersaturation sets in even before mixing is complete. Mixing and precipitation kinetics interact strongly under such conditions (Mersmann, 1995).

The intermediate step in the model precipitation reaction of iron oxide is the formation of the ferrous-ferric hydroxide complex which subsequently decomposes to give iron oxide. Tronc et al. (1992) and Faivere et al. (2004) have reported that as ferric-hydroxide precipitates faster than ferrous-hydroxide and thus precipitation of the latter hydroxide is the rate-limiting step in the process. The precipitation of ferrous hydroxide limits the critical nucleus size of the precipitate. The solubility product ($K_{sp} = 4.8 \times 10^{-17}$) of ferrous hydroxide is used to determine the supersaturation (S):

$$S = \sqrt{\frac{[Fe^{2+}][OH^-]^2}{K_{sp}}} \quad (4-1)$$

According to classical nucleation theory, the stable nucleus size (d_p^*) is strongly and inversely dependent on supersaturation. The nucleus size varies with changes in supersaturation; at high supersaturation, the effect is smaller. Lieser (1969) observed that a nucleus could only form when the energy barrier (ΔG^*) was overcome. This could occur as a result of random free energy variations in smaller volumes of solution. The energy change associated with the nucleation process (at constant T and P with spherical nuclei) is ΔG and is the sum of the energy associated with generation of new volume and extension in the surface area of the particles.

$$\begin{aligned}\Delta G &= \frac{4\pi r^3 \Delta G_v / v_m}{3} + 4\pi r^2 \gamma \\ &= \frac{4\pi r^3 (\mu_{eq} - \mu_i)}{3v_m} + 4\pi r^2 \gamma\end{aligned}\quad (4-2)$$

at a metastable equilibrium state: $\frac{d\Delta G}{dr} = 0$ and $r = r^*$

$$\Rightarrow r^* = \frac{-2\gamma v_m}{(\mu_{eq} - \mu_i)} \quad (4-3)$$

$$\text{and } \mu_{eq} - \mu_i = -k_B T \ln\left(\frac{a_i}{a_{eq}}\right) \quad (4-4)$$

Activity coefficients (a) are assumed to be equal to unity, thus a_i and a_{eq} become the concentrations C_i and C_{eq} .

$$\text{thus, } \mu_{eq} - \mu_i = -k_B T \ln\left(\frac{C_i}{C_{eq}}\right) \quad (4-5)$$

$$\text{and as } S = \frac{C_i}{C_{eq}} \quad (4-6)$$

$$\Rightarrow \mu_{eq} - \mu_i = -k_B T \ln(S) \quad (4-7)$$

back substituting equation (4-7) in equation (4-3), we get:

$$r^* = \frac{-2\gamma v_m}{-k_B T \ln(S)} = \frac{2\gamma v_m}{k_B T \ln(S)} \quad (4-8)$$

$$\Rightarrow d_p^* = \frac{4\gamma v_m}{k_B T \ln(S)} \quad (4-9)$$

Substituting interfacial tension ($\gamma = 0.8$ N/m) for the magnetite-water system (Jolivet et al., 2004), molecular volume ($v_m = 4.475 \times 10^{-29}$ m³/molecule), Boltzmann constant ($k_B = 1.38 \times 10^{-23}$ J/K) and absolute temperature ($T = 298$ K) in equation 4-9 gives equation 4-10 which is subsequently used to determine a stable nucleus size (d_p^*) for the given reaction conditions. C is the ‘actual’ substance concentration in the solution and C_{eq} is the equilibrium (saturation) concentration at a given temperature, pressure and system composition. C_{eq} is

usually estimated experimentally. In this work, supersaturation (S) was calculated using equation 4-1.

$$d_p^* = \frac{3.48 \cdot 10^{-8}}{\ln(S)} \quad (4-10)$$

It is important to note that the $\mu_{eq} - \mu_i$ is negative. This implies that energy is released and that the product state is stable with respect to reactants, therefore favoring precipitation.

The iron oxide precipitation is very fast, and very little literature is available in terms of its reaction kinetics. The precipitation time (τ_R) for the iron oxide reaction has been estimated from the rate data obtained by Faivre et al. (2004). It varies from 10^{-4} to 10^{-26} seconds under varying molecularity (2 to 8) of hydroxyl ions. Molecularity is 2 when enough hydroxyl ions are present in the reaction mixture to precipitate ferrous ions. Molecularity is 8 when enough hydroxyl ions are present to precipitate both ferrous and ferric ions. Since τ_R is very small, the precipitation of nuclei is assumed to be ‘almost’ instantaneous.

Diffusional growth of nuclei to primary particles

Both local nucleation rates and nucleic growth depend on local reactant concentration, and increase with an increase in concentration. The reagent concentration corresponding to the critical supersaturation, S_{crit} (minimum required for nucleation) and above is released via nucleation while the remaining supersaturation ($1 < S < S_{crit}$) is used for growth (Schwarzer and Peukert, 2002). Beattie (1989) reports that the growth of nuclei causes the concentration to fall below S_{crit} after which no new particles are created. The particles continue to grow until the concentration falls to the saturation concentration ($S = 1$).

Mersmann (1995) and Bramley et al. (1996) have argued that under supersaturation conditions particles grow before they agglomerate. Mersmann (2001) reports that particle growth can be considered to be diffusion-controlled at high supersaturation. Schwarzer et al. (2004), however, reported that particle growth could be considered to be transport-controlled at high supersaturation, though it may not be purely diffusional due to electrostatic attraction/repulsion

and the transport of the ionic species through particle charging. Schwarzer et al. (2005), following his earlier work worked out the following differential growth-rate expression with the assumptions that the surface charges change instantaneously, and the surface is at equilibrium (i.e. $S_{\text{surface}} = 1$).

$$G = \frac{\partial x}{\partial t} = 2 \frac{Sh D_{AB} \sqrt{K_{sp}} M (S - 1)}{\rho_c x} \quad (4-11)$$

In the above expression G is the growth rate, Sh is the Sherwood number, S is supersaturation, M is molecular weight, D_{AB} is diffusivity and ρ_c is the particle density. Marchisio et al. (2002) report nucleation and growth rate expressions for barium sulfate precipitation based on earlier investigation by Baldyga et al. (1995) and Nielsen and Toft (1984). For this reaction, the nucleation rate has a much higher order dependence on supersaturation (order 15) than the growth rate (order 2).

To investigate particle growth in the iron oxide model system, an expression for the growth rate is derived for spherical particles based on diffusive-transport through the solution surrounding the nuclei. The PDE (equation 4-12) was obtained by mole balance over a spherical control-volume. Diffusional growth was assumed to follow the nucleation process (nucleus size = d_p^*) and which continued until saturation limit was reached ($S = 1$) giving primary particle size d_p .

$$D_{AB} \frac{\partial^2 C}{\partial r^2} + \frac{2D_{AB}}{r} \frac{\partial C}{\partial r} = \frac{\partial C}{\partial t} \quad (4-12)$$

The PDE was solved with the following initial (I), final (F) and boundary (B) conditions:

I.C. $C = C^*$ (critical concentration) at $t = 0$ and all r

B.C. $C = C_{\text{eq}}$ (saturation concentration) at $t = t_o$ and $r = r_o (= d_p^*/2)$

F.C. $C = C_{\text{eq}}$ (saturation concentration) at $t = \tau_g$ and $r = r_f (= d_p/2)$

Where d_p^* is the precipitated nucleus size and d_p is the primary particle size which has grown from the nucleus under supersaturated conditions. Integrating equation (4-12) and substituting the IC, BC and FC, we obtain:

$$\tau_g = \left| \frac{d_p^2 - d_p^{*2}}{48 D_{AB} \ln\left(\frac{d_p}{d_p^*}\right)} \right| \quad (4-13)$$

Here D_{AB} is diffusivity and the calculated growth time (τ_g) is of the order of 10^{-10} seconds.

Particle growth can also manifest itself as conjoining (bridging) of the primary particles if they are in close vicinity. Two or more primary particles in close vicinity may diffusively grow, simultaneously, until they touch each other, whereon any further particle growth would fill the interparticle voids forming hard bridges between them. It is understood that supersaturation is also used up in bridge formation between the colliding particles. This bridging of primary particles lead to particle agglomeration and is discussed in the next section.

Agglomeration of primary particles

Agglomeration of particles in a precipitative environment is a complex phenomenon which is not as well understood as the aggregation of colloidal particles in ionic solutions. Nevertheless, a good understanding of agglomeration is needed due to its wide occurrence in many industrial processes including powder manufacture (Bramley et al., 1996). Bramley et al. (1996) and Mersmann (1995) have reported that agglomeration during a precipitation reaction in a supersaturated environment involves particle growth and bridge formation which occur simultaneously. Schwarzer and Peukert (2005) stated that agglomeration occurs after solid formation. Due to the rapid rate of these processes, control of agglomeration is a challenge and needs to be better understood before it can be prevented.

Depending on the hydrodynamic conditions and the physical properties of the suspending particles and fluid, collision and agglomeration of particles is driven either by Brownian motion, laminar shear or turbulent motion.

Mersmann (1995) has argued that for agglomeration of particles, particles need to be brought close together by diffusion and/or convection, collide, stay

together for a sufficiently long time (contact time) and then successfully stick together. It is hypothesized that iron oxide nuclei under net attractive forces (Van der Waals, magnetic and repulsive electrostatic force and local hydrodynamic force) diffusively grow, come-together, and bind together through material bridge (interparticle growth) formation. It is to be noted that growth and bridging may be extremely fast processes and may be happening simultaneously. Both rates are dictated by supersaturation level and significant particle agglomeration has been observed by Baldyga et al. (2002) at large reactant concentration. In a turbulent flow, turbulence brings about collisions, with fluid viscosity, particle-number density, particle size, and supersaturation determining the time of contact and successful 'sticking' of particles. Under turbulent flow conditions, where the shear forces are very high, the weaker or incompletely bridged particles/aggregates may break giving smaller agglomerates (Mersmann, 2001). Particles would agglomerate if they were in contact for a time longer than the time required to form material bridges. At low shear rates (mixing rates) particles have a greater probability of staying together than at high shear rates. Though very small particles usually agglomerate because of Brownian motion, they may also perceive turbulent fluctuations which induce collisions and agglomeration.

Bridge formation may occur in the crevice between two colliding particles (d_1 and d_2). Bridge formation time is estimated by growth rate (G), bridge volume (V_b) and contact surface area (SA) that the bridge shares with the particles in contact. The analysis has been reported by David et al. (1991) for predicting sticking (agglomeration) probability of two colliding particles during crystallization. The analysis has been used to understand agglomeration in our model system. For simplicity purpose it is assumed that bridging follows particle growth leading to particle agglomeration and that the bridge formation is repeated between other colliding primary particles and agglomerates as precipitation proceeds. It is to be noted that under very high supersaturation levels nucleation, particle growth and bridge formation may compete together. The growth rate used in bridge formation time expression here is assumed to be

equal to the diffusional growth rate. The bridge formation time (τ_b) is then given by the following expression and is estimated to vary between 10^{-11} s and 10^{-9} s. It is approximated as the minimum contact time required to build material bridges between the colliding particles. Marchisio et al. (2003) report another expression of the contact time. They incorporated a shape function (f) and diameter of a stable material bridge (D_b) to estimate the average contact time between the colliding particles that are smaller or larger than Kolmogorov eddy size.

$$\text{Bridging time: } \tau_b = \frac{V_b}{G \cdot SA} \quad (4-14)$$

$$\text{Where } V_b = \frac{\pi}{4} d_2^2 \left(\frac{d_2}{2} + x \right) - \frac{\pi}{12} d_2^3 - \pi x^2 \left(\frac{d_1}{2} - \frac{x}{3} \right) \quad (4-15)$$

$$SA = \frac{\pi}{2} d_2^2 + \frac{\pi}{2} d_1^2 - \frac{\pi}{2} d_1 \sqrt{d_1^2 - d_2^2} \quad (4-16)$$

$$x = \frac{d_1 - \sqrt{d_1^2 - d_2^2}}{2} \quad (4-17)$$

Diffusive sintering is another phenomena that has been reported with metal particles in a vacuum (Zhu and Averbach, 1996) and in an aqueous environment (Unwin et al, 2008) at both room and elevated temperatures. Diffusive sintering of titanium oxide particles has been studied in a vacuum (Koparde and Cummings, 2005) and the sintering time has been estimated to be of the order of 10^{-9} seconds. Diffusive sintering hasn't been reported for the iron oxide system but may be occurring to a limited extent.

Though the available literature refers to agglomeration of primary particles in turbulent field and its absence, the discussion is rather unclear. A more systematic approach is required to track agglomeration of nanoparticles and the dominant mechanisms (Brownian vs. laminar vs. turbulent) at various length scales and turbulence levels as the agglomerate size gets bigger in the fluid system upon particle collision. Due to variations in local energy dissipation in the CIJR, where dissipation at the impingement point is several orders of magnitude higher than the volume average dissipation, lengths scales vary within the mixing volume and therefore the dominant particle collision mechanism may be different

in different regions in the reactor. Variation in particle number density and the dissipation rate (turbulence) may together determine the controlling agglomeration mechanisms in different reactor regions.

Brownian aggregation occurs between small primary particles. It is usually the dominant agglomeration mechanism for particles smaller than the Batchelor length scale (η_B), which are caught within a Kolmogorov length scale eddy (λ_k).

$$\text{Batchelor length scale: } \eta_B = \left(\frac{\nu D_{AB}^2}{\varepsilon} \right)^{1/4} \quad (4-18)$$

Brownian collision (agglomeration) kernel (Masliyah and Bhattacharjee, 2006) is expressed as:

$$\beta = \frac{2k_B T}{3\mu} \frac{(d_1 + d_2)^2}{d_1 d_2} \quad (d_i < \eta_B) \quad (4-19)$$

Laminar and micro-shearing agglomeration is understood to occur when particles/agglomerates collide due to velocity difference between the particles in viscous sub-range (below Kolmogorov length scale). This occurs when the particles follow the streamlines and a velocity gradient causes them to approach each other.

$$\text{Kolmogorov length scale: } \lambda_k = \left(\frac{\nu^3}{\varepsilon} \right)^{1/4} \quad (4-20)$$

Laminar collision (agglomeration) kernel (Masliyah and Bhattacharjee, 2006; Kusters et al., 1997) is expressed as:

$$\beta = \frac{(d_1 + d_2)^3}{6} \dot{\gamma} \quad (d_i < \lambda_k) \quad (4-21)$$

The turbulent aggregation model is less sensitive to the absolute particle/agglomerate size than laminar aggregation (David et al., 2003). Both laminar and turbulent agglomeration mechanisms depend on the mixing conditions whereas the Brownian aggregation doesn't (David et al., 2003). The collision/agglomeration models are based on volume-average properties, are derived in the absence of any attractive or repulsive forces and are for a 2-particle system. Table 4-1 lists various turbulence collision kernels. All of these model assume uniform shear rates and the corresponding volume averaged

energy dissipation rate. Marchisio et al. (2003) and Hollander (2001) however stress that for a detailed modeling of aggregation processes spatial heterogeneity of the shear in the mixing system needs to be considered.

The agglomeration rate of the colliding particles depends on the collision kernel, the number concentration of the species and the agglomeration efficiency. The collision frequency per unit volume (J_{ij}) is expressed as:

$$J_{ij} = \beta n_i n_j \quad (4-22)$$

The agglomeration efficiency ($= \exp(-\tau_c/\tau_i)$) has been given by Marchisio et al. (2003) and Baldyga et al. (2001) and is dependent on the contact time (τ_c) and the interaction time (τ_i). Contact time can be interpreted as the bridge formation time (τ_b) while interaction time (τ_i) can be approximated to the eddy lifetime or Kolmogorov time scale ($= (\nu/\epsilon)^{1/2}$). In this work, agglomeration efficiency varies between 99.8% and 99.99 % for colliding particle sizes of 5nm to 200nm.

Figure 4-4 shows the effect of colliding particle size on the Brownian, laminar and turbulent collision frequency. Shear agglomeration frequency estimations are based on mean and maximum dissipation rate in the mixing volume. The primary particle size is d_{pi} while d_{HA} is the hard agglomerate size. Figure 4-4(a) shows the beginning of the agglomeration process, when only primary particles are present. Primary particles and smaller agglomerates in the range of 5 ~100 nm follow Brownian motion. Agglomeration at this length scale is clearly dominated by Brownian effects. From Figure 4-4 (b) it is evident that the collision frequency between large and small particles is high. This condition occurs towards the later part of the precipitation and agglomeration process. Collision frequency is seen to increase with particle size and is high when both of the colliding particles are large in size. The Brownian effect dominates until the second-particle (agglomerate) size reaches a size where shear-induced agglomeration begins to be important. The Brownian collision frequency decreases as the colliding particles get bigger in size. The turbulent agglomeration (collision) frequency increases with particle sizes and is significantly large for micron size or bigger particles. It is evident from the figure that agglomeration is largely turbulence-induced at the scale of the hard

agglomerates. Laminar induced agglomeration (shear rate = 5 s^{-1}) is much smaller than either Brownian ($5 \sim 10 \text{ nm}$) or turbulent ($100 \text{ nm} - 1 \mu\text{m}$), agglomeration rates for all particle sizes.

Table 4-2 compares Batchelor length scale, Brownian length limit and the estimated particle spacing inside the reactor. Smaller Batchelor length scales are obtained from the maximum energy dissipation in the reactor. The Batchelor length scale is smaller than the Brownian length scale and the inter particle spacing falls in the mid range. This indicates that the particles can both diffuse towards each other in the lifetime of an eddy and agglomerate under Brownian influence. As the smallest Batchelor length scale is smaller than the particle spacing in the reactor, turbulence can affect movement of primary particles and can cause collision between them.

Mumtaz (1997) found that with increasing shear, the effective agglomeration decreased. The drop in agglomeration indicated an efficiency component in the collision process. Mumtaz et al. (1997) thus developed an efficiency model to correlate agglomeration kernel and collision rate as a function of particle size, shear rate and material deposition rate at the contact of the two particles under supersaturated conditions. Hollander (2001) used the agglomeration model developed by Mumtaz (1997) to numerically study the 'local' agglomeration rate in a stirred tank through a Lattice-Boltzmann algorithm with LES for modeling turbulence and a Monte-Carlo scheme to track the local PSD in time. Hollander (2001) observed that when the viscous forces acting on the agglomerate were larger than the strength of the chemical bond formed between the particles, the agglomerate wouldn't survive and the collision was ineffective. There was however a disadvantage to the approaches adopted by Mumtaz (1997) and Hollander (2001) - the formation and destruction steps in the agglomerate formation were not treated separately. Braun (2003) experimentally studied aggregation and breakup steps in aggregation process separately. Schuetz and Piesche (2002) studied PSD in a stirred tank by modeling aggregation, breakage and erosion steps in primary particle aggregation. They assumed aggregation efficiency as unity. Bähler (2008) developed a collision efficiency model for

porous fractal aggregates including hydrodynamic and colloidal interactions between the aggregates under simple-shear conditions. Bäbler (2008) noted that hydrodynamic interactions caused a deflection in the relative trajectories and thus a decrease in collision efficiency; whereas the attractive interparticle forces lead to an increase in collision efficiency. He concluded that the collision efficiency could be either small or larger than unity depending on the magnitude of the two types of interactions and that the highest collision efficiency was observed for agglomerates with equal mass. He also noted the shortcoming of his approach – when the two agglomerates widely varied in size, the smaller one entered the bigger (porous) one without undergoing any physical contact. Bäbler et al. (2008) modeled breakage of solid aggregates suspended in a stirred tank through a population balance approach. It was concluded that the aggregate size increased with an increase in solid volume fraction and thus flow field heterogeneity in stirred tanks needed to be included in the model. Kusters et al. (1997) studied collision efficiency of porous aggregates smaller than Kolmogorov length scale with polystyrene particles (diameter $\sim 1\ \mu\text{m}$) considering hydrodynamic interactions through a ‘shell-core’ model. Collision efficiency was estimated from the aggregates relative trajectories and point of contact of the two porous flocs. Higher collision efficiency for equal sized flocs which were able to approach each other closely, was observed.

Ehrl et al. (2008) studied aggregation of polystyrene particles in stirred tank and Taylor-Couette devices with distinctly different shear-rate distributions. They reported that both Brownian motion and shear caused aggregation and when the aggregate size was large enough, breakage would set in and the aggregate ceased to grow any further. They concluded that the steady-state aggregate size couldn't be defined by the volume average shear rate (even for dilute conditions) and it depended on the shear rate distribution in the vessel. Ehrl et al. (2007) studied the effect of primary particle size on the steady-state aggregate size and structure for varying shear rate and solid-volume fraction under turbulent conditions in stirred tank. They concluded that agglomerate sizes with similar solid volume fraction and hydrodynamic conditions were

independent of primary particle diameter because of the surface roughness which provided bonding forces of similar order. Zeidan et al. (2007) reported that agglomerate morphology in a shear flow was strongly dependent on the dominating aggregate breakup mechanism: (1) erosion (breakup of primary particles or small-aggregates from the surface of a larger aggregate, or (2) rupture (breakup of similar sized aggregates from a large aggregate). Zeidan et al. (2007) cited Parker et al. (1972) who reported that the shear forces caused both aggregate formations (by promoting collisions) and their destruction. It was suggested that the aggregation and breakup of the aggregates under shear forces was strongly dependent on interparticle forces. Aggregate deformation and breakage steps were simulated and it was concluded that rupturing was the dominant breakup mechanism for weak agglomerates and that for strong agglomerates, high shear was needed to break them up. Erosion dominated at low shear rates. It was concluded that the final aggregate size was a function of the shear rate.

Zeidan et al. (2007) reviewed works by Gregory (1989), Yeung and Pelton (1998), Selomulya (2001), Adler and Mills (1979) and Sonntag and Russel (1987). Gregory (1989) observed that aggregates bigger than Kolmogorov length scale ruptured, whereas those smaller than Kolmogorov could be either ruptured or eroded. Yeung and Pelton (1996) suggested that erosion was more likely to occur in compact structures, whereas rupture would occur in less-compact (open) structures. Selomulya (2001) noted that the interplay between the interparticle and hydrodynamic forces determined the dominant breakup mechanism. Adler and Mills (1997) and Sonntag and Russel (1987) suggested that flow distribution near the outer surface of the aggregate determined whether erosion or rupture dominated as the breakup mechanism.

From an understanding of mixing, nucleation theory, diffusional growth of particles and its effect on supersaturation, one can infer that both mixing and reactant concentration will have a significant effect on the agglomeration of primary particles which in turn depends on their size and that a close inter-relationship exists between the various steps in the process. Also from the above

literature review it is understood that shear-induced rupture, erosion or breakage also play an important role in determining final agglomerate size, whose effect is in turn dependent on primary particle-surface roughness, interparticle forces, size ratio of colliding particles, aggregate size (before shear effects begin to act), agglomerate-porosity, shear rate and its distribution in space, material deposition rate between the particles and chemical-bond (bridge) strength. According to the existing theory, turbulent-shear come into effect only above the Kolmogorov length limit, below which collision and thus agglomeration is either Brownian or Laminar induced. Though agglomeration rupture or breakage occurs only under high-shear conditions like in turbulent field; Laminar shear can cause both agglomeration and erosion, effect of which is influenced by process time scale (residence time) i.e. primary particles remain in the reactor for sufficiently long time to see agglomeration or erosion effects.

Analysis

To understand the nucleation, growth and agglomeration process in the iron oxide system under fast mixing conditions in CIJR, the results are analyzed in terms of nucleus size (d_p^*), primary particle size (d_p), hard agglomerate size (d_{HA}) and several other intermediate variables derived from material balances over the precipitation system. All of these variables need to be understood to gain insight into the complex combination of mechanisms and their relative rates, and to determine the final (steady-state) hard-agglomerate size. The steps in the analysis are summarized below.

d_p^* estimation:

The stable nucleus size is estimated from classical nucleation theory (equation 4-10).

d_p estimation:

TEM images of hard agglomerates (e.g. Figure 4-2) corresponding to varying reaction and mixing conditions are analyzed using propriety image processing software (Advanced Microscopy Techniques, USA). A random hard

agglomerate sample comprising primary-particles is identified and the longest diameter of the near spherical particles measured with the length scale marker. The measurements were repeated for a data set of 50-150 primary particles and the mean, median and the PSD are reported for further analysis.

d_{HA} estimation:

The hard agglomerate size of the particles in suspension collected from the CIJR exit was measured using a Brookhaven zeta plus DLS analyzer. A total of 5 consecutive readings were taken and their mean reported for further analysis. The following intermediate variables were estimated from the above size measurements.

- 1) τ_R, τ_g, τ_b Precipitation time (Faivre et al., 2004), growth time (equation 4-13) and bridge formation time (equation 4-14)
- 2) n_{pp} Number of primary particles formed (= number of nuclei) per second given the total iron fed and d_p , the mass of each primary particle, m_{pp} , n_{pp} (equation 4-24) is calculated.

$$\dot{M}_{product} = \dot{n}_{Fe_3O_4} MW \quad (4-23)$$

$$\dot{n}_{pp} = \frac{\dot{M}_{product}}{m_{pp}} \quad (4-24)$$

- 3) m_g Product mass available for growth (equation 4-25).

$$\dot{m}_g = \dot{M}_{product} - m_p^* \dot{n}_{pp} \quad (4-25)$$

Here m_p^* is the mass of a single precipitated nuclei, $\dot{M}_{product}$ is the mass flowrate of product

- 4) N_g Number of moles available (per nuclei) for growth. Given d_p^* and n_{pp} , it is assumed that each primary particle arises from one nucleus. Subtracting the mass of n_{pp} nuclei from the total mass and dividing by n_{pp} gives N_g for each nucleus (equation 4-26).

$$N_g = \frac{\dot{m}_g / MW}{\dot{n}_{pp}} = \frac{\dot{n}_g}{\dot{n}_{pp}} \quad (4-26)$$

- 6) C_g The number of moles available for growth per volume.

$$C_g = \frac{\dot{n}_g}{V_{CIJR}} \quad (4-27)$$

7) %N_g Percent of reagent that is consumed by growth (equation 4-28).

$$\%N_g = \frac{n_g}{n_{Fe_3O_4}} \quad (4-28)$$

8) n_{HA} Number of primary particles per hard agglomerate (HA); estimated as (d³_{HA}/d³_{pp}). The packing factor is assumed to be one, so the number estimated is significantly larger than the actual number of primary particles. Since all hard agglomerates have a similar shape, the relative trend is understood to be accurate.

9) η_{HA} The ratio of the number of primary particles in a hard agglomerate to the number of primary particles for agglomeration during a residence time. It represents sticking efficiency.

10) N_{HA} (s⁻¹) Rate of generation of hard agglomerates (n_{pp}/n_{HA})

11) d (nm) Interparticle spacing between primary particles in the CIJR. The number of primary particles existing in the CIJR at any instant, n_{pp}, is calculated from equation 4-30. n_{pp} is then used in equation 4-31 to compute volume of a fluid cloud associated with each primary particle. The distance between the neighboring primary particles in CIJR is the difference between the diameter of the fluid cloud and the primary particle diameter.

$$m_{product} = n_{Fe_3O_4} MW \quad (4-29)$$

$$n_{pp} = \frac{m_{iron\ oxide}}{m_{pp}} \quad (4-30)$$

$$V_{CIJR} = V_{pp} n_{pp} \quad (4-31)$$

$$d_{fp} = \sqrt[3]{\frac{6V_{pp}}{\pi}} \quad (4-32)$$

$$d = d_{fp} - d_p \quad (4-33)$$

Experimental

Experimental setup

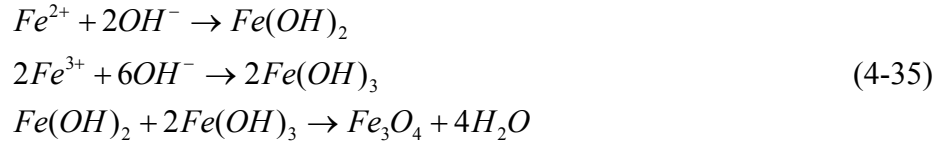
The confined impinging jet reactor (CIJR) consists of a closed mixing volume (diameter 4.7 mm) fed by two fluid jet streams (each of diameter 1 mm). The mixing-volume has a hemispherical top while the downspout is conical with a 1.5 mm exit pipe diameter. Constant pulse-free flows to the CIJR were provided by micropump-heads (Series GB, external gear pump, max flow rate 4L/min), which were fitted onto pump drives (MCP-Z standard, IDEX corporation). Each of the micropumps was calibrated by volumetric and mass flow methods for a range of flow rates from 20 mL/min to 509 mL/min. A dye flow visualization technique was used to monitor the stability of the flow in the CIJR. All experiments were conducted under balanced and equal flow conditions in both inlet pipes.

Iron oxide reaction

Co-precipitation experiments with iron oxide were carried out at ambient conditions. As the residence time of the reactor is milliseconds, any temperature change in the product mass due to the input energy (to mix the reactants) or the precipitation reaction is neglected. The crystalline iron oxide is obtained from co-precipitation of ferrous-ferric hydroxides and removal of water molecules from the amorphous hydroxides. Iron oxide precipitates according to the following overall reaction scheme (Lin et al., 2005 and Maity and Agrawal, 2007):



Mixing between ferrous chloride and ferric chloride and NaOH initiates the complex process of crystal precipitation. Oxide formation is a complex reaction step during which the hydroxides react and lose water, followed by a condensation reaction within newly formed solid phase at high pH ~12-13 (Lieser, 1969). The intermediate steps are simplified as:



Reagent solutions were prepared using Reverse-Osmosis treated water and certified quality ferrous chloride, ferric chloride and sodium hydroxide (Siddiqui et al., 2009). The solution concentrations are listed in Table 4-3.

The product solution collected from the CIJR was a suspension of precipitate, excess reagents and reaction products. It was washed multiple times with reverse-osmosis (R.O.) water and decanted prior to particle sizing measurements. The decanted sample was sonicated for 15 minutes and diluted by RO water to $\leq 1\%$ v/v (particle sizer specific recommendation) prior to particle size measurements in Brookhaven ZetaPlus particle size analyzer. The sample in the vial was re-sonicated for a minute before each size measurement to re-disperse any loose aggregate formations. The Brookhaven ZetaPlus measures the effective diameter (d_{65}) of the particles in suspension. d_{65} is the intensity weighted average diameter or the hydrodynamic diameter. Small polydispersity values (~ 0.005) were obtained i.e. the particles were monodisperse. Particle sizing on each sample was repeated five times to ensure consistency in the particle size and polydispersity measurements. The standard deviation varied between 120 nm and 15 nm over particle size measurements ranging from 1.5 micron to 200 nm over the range of flow rates investigated. Zeta potential measurements on the particles in suspension are often reported, but haven't been considered in this study.

TEM (JEOL 2010, Japan) imaging was carried out on the sample after particle size measurements. The particle suspension was dropped onto 200-mesh carbon coated Cu grids (Pelco, USA) and allowed to dry before TEM images of the precipitate particles were collected and used to measure primary particle sizes using software Origin. Other techniques like X-ray diffraction and specific surface area measurements are often used to estimate primary particles in agglomerates, but are not employed in this work.

Gupta and Gupta (2005) report that complete precipitation of Fe_3O_4 is expected between pH of 9 and 14. Kang et al. (1996) reported that homogeneous and uniform sized iron oxide particles could be obtained at a pH of 11-12 with $\text{Fe}^{2+}/\text{Fe}^{3+}$ ratio of 1:2. To confirm the earlier observations, a series of precipitation reaction were run at varying Fe^{2+} , Fe^{3+} and OH^- concentrations to vary the reaction pH and confirm the above observations.

Figure 4-5 shows the effect of pH on hard agglomerate and primary particle size, respectively. The reaction pH is varied by varying sodium hydroxide concentration. Though there is only a small effect of pH on agglomerate size, the primary particle size decreases with an increase in pH up to 7, and then levels off. Nucleation rates are higher at higher pH due to the higher supersaturation associated with an increase in hydroxyl concentration, which may limit the particle growth. The particles are similarly (negatively) charged and thus mutual electrostatic repulsion may also prevent them from agglomerating. Local hydrodynamic forces (local pressure increase) generated on close approach of the particles may also push them apart limiting agglomeration.

Results

The results show the influence of changes in feed concentration and mixing conditions on nucleus size (d_p^*), primary particle size (d_p) and, thus, hard agglomerate size (d_{HA}). Hard agglomerate size is observed to vary with the size of the primary particles i.e. larger primary particles give smaller agglomerates. Agglomeration efficiency is thus understood to depend on the size of the colliding particles. The results are divided in two parts. In the first part, the effect of feed concentration (supersaturation) is analyzed while the second part deals with the flow rate (mixing) effects. The feed concentration (iron and hydroxide) are varied separately. The effect of the feed concentration and flow rate on primary particle size and hard agglomerate formation is explained through calculated particle growth rate (G), number of primary particles per hard agglomerate (n_{HA}) and other intermediate variables.

Figure 4-6 shows the effect of flow rate and feed concentration on hard agglomerate size (d_{HA}). Two important observations are made: 1) d_{HA} decreases with an increase in flow rate at all feed concentrations. The effect is most pronounced at high feed concentrations; and 2) d_{HA} decreases with an increase in feed concentration at all flow rates.

Table 4-4 illustrates the effect of feed concentration and flow rate on the size of stable nuclei (d_p^*) and primary particles (d_p). The nucleus size is seen to be weakly dependent on the range of supersaturation studied and varies from 1.9 nm to 2.1 nm for a 4-fold increase in supersaturation. It is independent of flow rate. It is evident that nuclei are able to grow to the primary particle size during the very short residence time (10^{-1} to 10^{-2} seconds) in the CIJR as all the growth times are of the order of 10^{-10} s. Growth is thus an active mechanism. Also the hard agglomerate size (d_{HA}) decreases with an increase in primary particle size.

Table 4-5 gives the bridge formation time for different 2-particle colliding systems. For bigger particles, the bridge formation time is an order of magnitude longer than the growth time (10^{-10} s). For the smaller primary particles, the bridge formation time is the same as the growth time (10^{-10} s). Smallest bridging time (10^{-11} s) is estimated for dissimilar particles while the biggest time (10^{-9} s) is observed for bigger and similar sized particles. Less material needs to be deposited between the particles to bind them in the former case, while more material must be deposited in the later case. The bridging time is always much shorter than the residence time. It is to be noted that agglomeration in precipitation systems is strongly dependent on the local supersaturation conditions.

As both the growth time ($\sim 10^{-10}$ seconds) and the bridge formation time ($\sim 10^{-9} - 10^{-11}$ seconds) are very short for a wide range of reactant concentrations, the particles can easily grow and agglomerate together within the residence time of the reactor ($\sim 10^{-2}$ seconds). Also at the beginning of the precipitation process when collisions and subsequent agglomeration occur between the primary particles, collision frequency is high due to large particle number density,

however; as agglomeration picks up the number of particles decrease.

Agglomeration thus leads to fewer but bigger particles.

Focusing on points 1,2 and 3 in Table 4-6 and Figure 4-6 where the flow rate is kept constant at 500 mL/min, it is seen that similar size nuclei (d_p^*) grow to increasingly larger primary particles (d_p) with an increase in feed concentration and the associated supersaturation. Since the primary particles are smaller than the Batchelor length limit, they grow through diffusion process which is dependent on the concentration gradient surrounding the particle. This concentration gradient increases with an increase in feed concentration, promoting diffusional flux. Also at lower supersaturation levels and high mixing rates, there are smaller spatial gradients in supersaturation than at high supersaturation. This leads to decrease in growth rates (function of local supersaturation). A 2-fold increase in primary particle diameter is measured for a 18-fold increase in ferrous-ferric concentrations. If mixing intensity is increased by 3X at high supersaturation, the primary particle size increases from 6.9nm to 10.6nm. Figure 4-7 shows the PSD of primary particles. Mean particle size and the distribution in primary particle size increase with increase in iron concentration.

For points 1 to 3 the hard agglomerate size (d_{HA}) is observed to decrease with an increase in iron concentration. At identical mixing conditions, the nucleation rate increases with supersaturation. The bridge formation time is dependent on local supersaturation condition and it successfully competes with nucleation rate which leads to formation of larger agglomerates. Under high supersaturation condition though bridge formation kinetics are fast, but the nucleation rate is much faster, resulting in limited bridge formation and smaller hard agglomerates. The hard agglomerate size obtained varies with primary particle size and depends on agglomeration efficiency, collision frequency, shear induced breakage and breakage due to hard particle collisions. This is due to variation in local supersaturation condition (and therefore growth) under high feed concentrations.

Nucleation rate (n_{pp}) is calculated from the total mass balance given the total reactants fed into the system and the measured primary particle size from TEM imaging. A 3-fold increase in the generation rate of nuclei (n_{pp}) is observed for a 18-fold increase in feed concentration. Given the hard agglomerate size, primary particle size and the number of primary particles in a hard agglomerate (n_{HA}) and hard agglomerate generation rate (N_{HA}) are estimated. The nucleation rate (n_{pp}) and agglomerate production rate (N_{HA}) also increase with an increase in iron concentration given that higher supersaturation needs to be released in a given mixing time. n_{HA} is seen to decrease with a decrease in d_{HA} and an increase in primary particle size. Point 3 corresponds to the highest concentration and the largest primary particle size (d_p) with hard agglomerates that are made up of 10^4 primary particles. For the lowest feed concentration and the smallest d_p (at point 1), each hard agglomerate contains 1000x more primary particles (10^7). Since the mixing conditions are identical (flow rate = 509 mL/min), the number of primary particles in a hard agglomerate indicates a decrease in agglomeration efficiency (η_{HA}) with increasing primary particle size. η_{HA} decreases by 1800X as d_p increases from 5.8 nm to 10.6 nm. The production rate of hard agglomerates (N_{HA}) increases by 1800X for an increase in feed concentration of 18X. Also the reactant concentration for growth (C_g) and the number of reactant moles available for growth (N_g) increases with an increase in feed concentration. It is estimated that only 2% of the total feed concentration (or supersaturation) is consumed by nucleation while the remaining 98% ($\%N_g$) is used in growth and bridging between particles.

Points 3 and 4 in Table 4-6 and Figure 4-6 show that the primary particle size increases with an increase in flow rate. Under very high reactant concentration, nucleation and particle growth may compete together for the available supersaturation, growth may overcome nucleation effects due to high-level of supersaturation due to non-uniformity in spatial distribution of supersaturation. This tendency is indicated from nucleation rate and particle growth estimates between point 3 and 4. A 40-fold decrease in the number of primary particles agglomerating together (n_{HA}) is seen for a flow rate increase

from 165 mL/min to 509 mL/min. A 30-fold increase in agglomerate production rate (N_{HA}) is seen for a 4-fold increase in flow rate. A 10X decrease in η_{HA} (for 165 mL/min to 509 mL/min) indicates that the agglomeration tendency decreases with mixing rate. Particles agglomerate successfully if their contact time is similar to the bridge formation time. Contact time between the particles decreases with shear rate (i.e. mixing rate).

Similar observations were made for points 5 and 6 in Figure 4-8 and Table 4-6 that show that at low hydroxyl concentration, an increase in flow rate leads to an increase in nucleation rate (n_{pp}) with no significant difference in primary particle size. This indicates that under low feed (low-supersaturation) conditions, less supersaturation is available for primary particle growth leading to limited growth of particles, than under high feed (high supersaturation) conditions. There is a minimal drop in hard agglomerate size with flow rate with similar sized primary particles.

Conclusions

The effect of flow rate and reactant concentration on nucleus size, primary particle size and hard agglomerate size has been investigated. A detailed analysis was carried out on particle size data to understand particle growth, nucleation and hard agglomerate formation. Nucleation, primary particle size and hard agglomerate size are dependent on supersaturation and flow rate conditions. The nucleation rate (n_{pp}) increases with reactant concentration and flow rate. Smallest hard agglomerates and biggest primary particles are obtained at the highest flow rate and highest reactant concentration.

Diffusional growth of particles is very fast and so is the bridge formation and they both occur within the residence time of the reactor. The pH does not have any appreciable effect on hard agglomerate size but smaller primary particles (~ 8 nm) are obtained at the highest pH values.

The hard agglomerates obtained are smaller than the Kolmogorov length scale. As evident from various collision and agglomeration models extremely small particles (~ 100 nm) may see shear effects due to velocity fluctuations in

turbulent flows. In such a limit there is a likeliness of shear-induced breakage occurring. Erosion may also be occurring. Size reduction due to hard agglomerate collisions may also be occurring but would be limited. Again according to the theory, Brownian agglomeration would dominate at the nano length scales encountered in this precipitation system.

It is concluded that both mixing and feed concentration conditions affect primary particle size and that its size influences the final hard agglomerate size. The primary particles are expected to agglomerate under Brownian motion and when they get bigger their size is further increased by turbulent-agglomeration or decreased by turbulence-induced breakage or erosion. All of the hard agglomerates in this work were smaller than the Kolmogorov scale.

Tables

Table 4-1: Turbulence collision (agglomeration) kernel

Expression	Restrictions	Reference
$\beta = \frac{(d_1 + d_2)^3}{6.18} \sqrt{\frac{\varepsilon}{\nu}}$	$d_i \leq \lambda_k$	Saffman and Turner, 1956; Kusters et al., 1997; Marchisio et al., 2003
$\beta = \frac{(d_1 + d_2)^{7/3}}{1.74} \varepsilon^{1/3}$	$d_i \geq \lambda_k$	Mersmann, 2001; Marchisio et al., 2003
$\beta = 1.253(d_1 + d_2)^2 (\bar{U}_1^2 + \bar{U}_2^2)^{1/2}$	$d_i \gg \lambda_k$	Mersmann, 2001

Table 4-2: Batchelor length scale based on particle diffusivity and the mean or maximum energy dissipation.

Flow rate (mL/min)	Batchelor Length Scale		Brownian Length Scale	Particle Spacing
	η_B (min) (nm)	η_B (max) (nm)		
165	75	12	110 - 270	37
300	48	8	70 - 190	45
500	33	5	50 - 130	57

Table 4-3: Effect of flow rate and reactant concentration on iron oxide mean agglomerate and primary particle sizes.

Flow rate (mL/min)	[Fe ²⁺]/[Fe ³⁺] (M/M)	[OH ⁻] (M)	Hard agglomerate mean diameter (nm)	Primary particle mean diameter (median diameter) (nm)
63	0.18/0.36	1	907	9.75* (9.2)
165	0.18/0.36	1.45	623	7.1 (6.9)
509	0.18/0.36	1.45	494	12.4# (10.6)
509	0.036/0.072	1.45	1072	7.6 (7.4)
509	0.01/0.02	1.45	1333	6 (5.8)
509	0.18/0.36	1	872	8.82 (8.84)

* standard deviation = 3.5, # standard deviation = 5.3 and others < 2

Table 4-4: Mass transfer limited growth. Time required to grow nuclei to the observed primary particle size. [Fe³⁺] = 2[Fe²⁺]

Flow rate (mL/min)	[Fe ²⁺] (M)	[OH ⁻] (M)	Supersaturation	d _p [*] (nm)	d _p (nm)	τ _g (s)
63	0.18	1.00	3.75 x 10 ⁷	1.94	9.2	4.87 x 10 ⁻¹⁰
165	0.18	1.45	8.9 x 10 ⁷	1.9	6.9	3.24 x 10 ⁻¹⁰
509	0.18	1.00	3.75 x 10 ⁷	1.94	8.84	4.59 x 10 ⁻¹⁰
509	0.01	1.45	2.1 x 10 ⁷	2.1	5.8	2.72 x 10 ⁻¹⁰
509	0.036	1.45	4 x 10 ⁷	2.0	7.4	3.67 x 10 ⁻¹⁰
509	0.18	1.45	8.9 x 10 ⁷	1.9	10.6	5.99 x 10 ⁻¹⁰

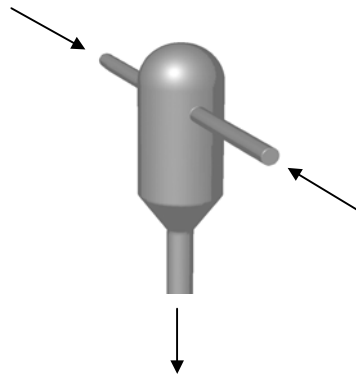
Table 4-5: Time required to form a material bridge between colliding particles

d₁ (nm)	d₂ (nm)	d₂/d₁	τ_b (s)
10	10	1	1.2 x 10 ⁻¹⁰
20	10	0.5	1.1 x 10 ⁻¹⁰
40	10	0.25	9.4 x 10 ⁻¹¹
200	10	0.05	8.2 x 10 ⁻¹¹
200	20	0.1	1.7 x 10 ⁻¹⁰
200	200	1	2.4 x 10 ⁻⁹

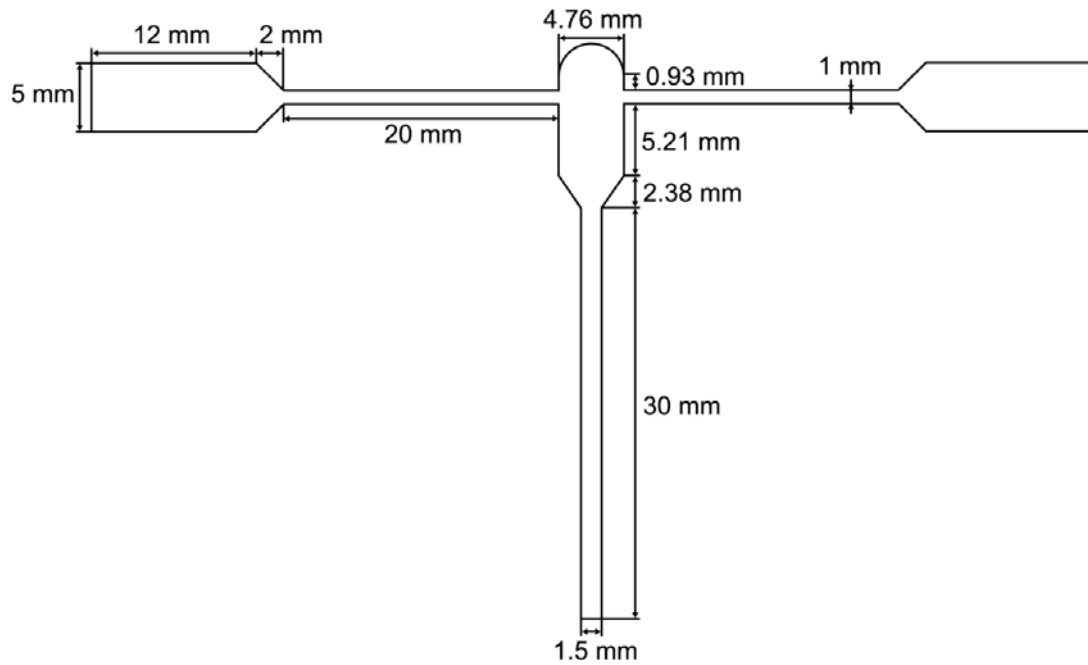
Table 4-6: Effect of reactant concentration and jet flow rate on hard agglomerate size, estimated nucleus size, generation rate of nuclei, reactant concentration available for nucleic growth, number of moles available per nucleus for growth, fraction of available reactant used for diffusional growth, size of primary particle, number of primary particles sintered together in a hard agglomerate and generation rate of hard agglomerates.

	Point 1	Point 2	Point 3	Point 4	Point 5	Point 6
[Fe ²⁺] (M)	0.01	0.036	0.18	0.18	0.18	0.18
[OH ⁻] (M)	1.45	1.45	1.45	1.45	1.00	1.00
Flow rate (mL/min)	509	509	509	165	509	63
d _p [*] (nm)	2.1	2	1.9	1.9	1.94	1.94
n _{pp} (s ⁻¹)	3.73 x 10 ¹⁶	6.46 x 10 ¹⁶	11 x 10 ¹⁶	12.9 x 10 ¹⁶	19 x 10 ¹⁶	2.08 x 10 ¹⁶
C _g (M)	0.0004836	0.017746	0.08962	0.088637	0.089308	0.089386
N _g (moles)	2.2 x 10 ⁻²¹	4.66 x 10 ⁻²¹	1.38 x 10 ⁻²⁰	3.79 x 10 ⁻²¹	7.99 x 10 ⁻²¹	9.02 x 10 ⁻²¹
%N _g	96.7	98.6	99.6	98.5	99.2	99.3
d _p (nm)	5.8	7.4	10.6	6.9	8.84	9.2
d _{HA} (nm)	1333	1072	288	623	872	907
n _{HA}	1200 x 10 ⁴	300 x 10 ⁴	2 x 10 ⁴	73 x 10 ⁴	96 x 10 ⁴	96 x 10 ⁴
η _{HA}	3.23 x 10 ⁻⁸	4.66 x 10 ⁻⁹	1.82 x 10 ⁻¹¹	1.85 x 10 ⁻¹⁰	5.08 x 10 ⁻¹⁰	5.74 x 10 ⁻¹⁰
N _{HA} (s ⁻¹)	3.1 x 10 ⁹	21 x 10 ⁹	5500 x 10 ⁹	180 x 10 ⁹	200 x 10 ⁹	22 x 10 ⁹

Figures

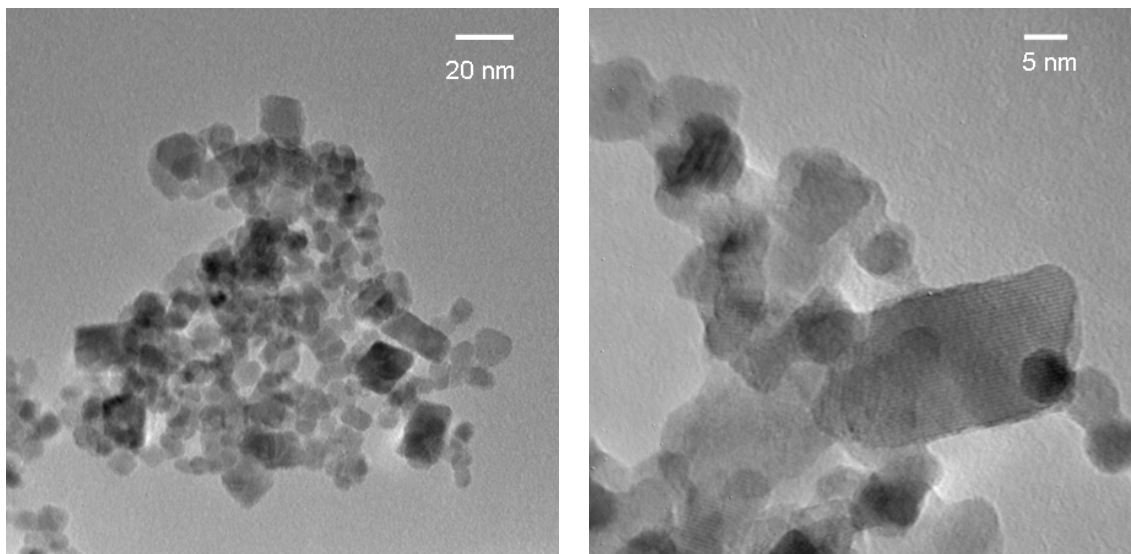


(a)



(b)

Figure 4-1: Isometric view (a) of CIJR and (b) its dimensions



(a)

(b)

Figure 4-2: (a) TEM image of iron oxide hard agglomerate at magnification of (a) 500,000x and (b) 800,000x. $[\text{Fe}^{2+}] = 0.18 \text{ M}$, $[\text{Fe}^{3+}] = 0.36 \text{ M}$, $[\text{OH}^-] = 1.45 \text{ M}$ and flow rate = 509 mL/min.

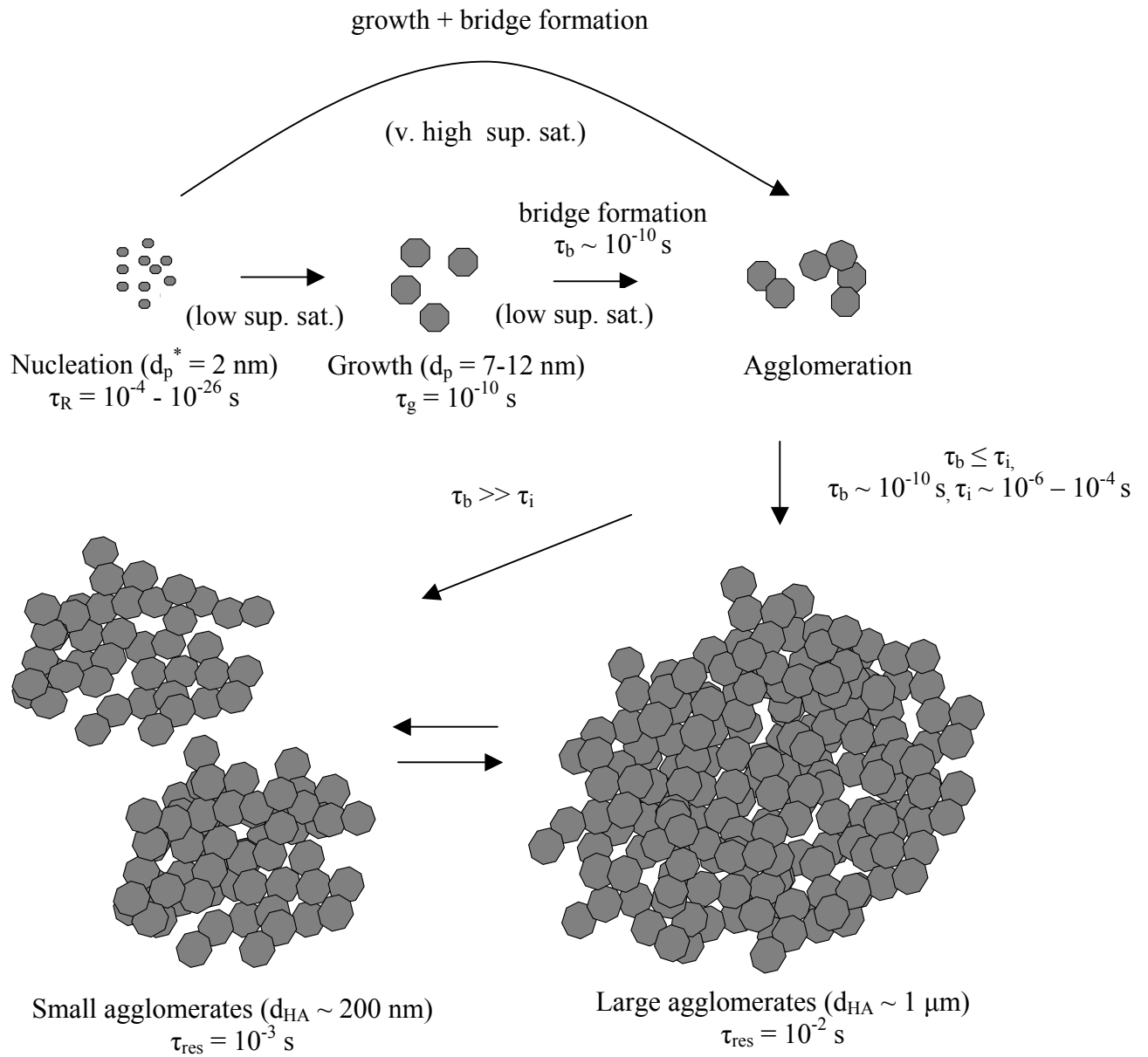
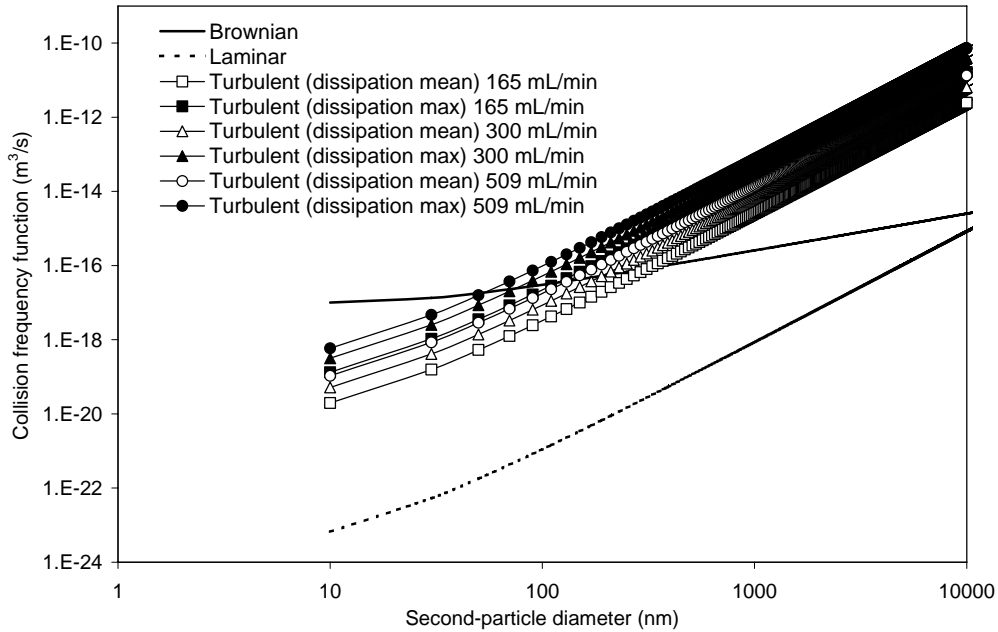
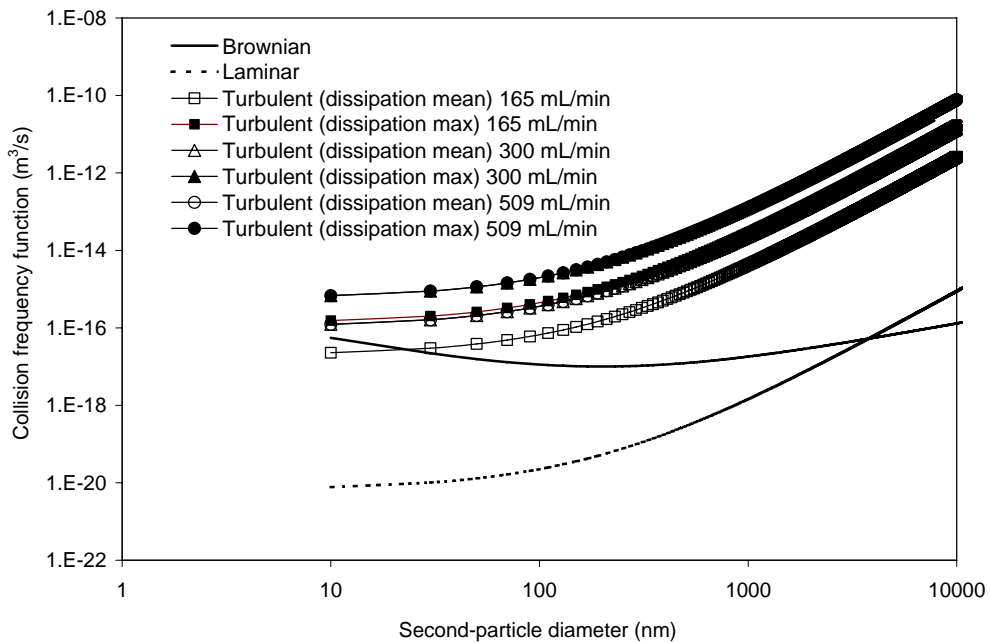


Figure 4-3: A schematic of the possible pathways for hard agglomerate formation

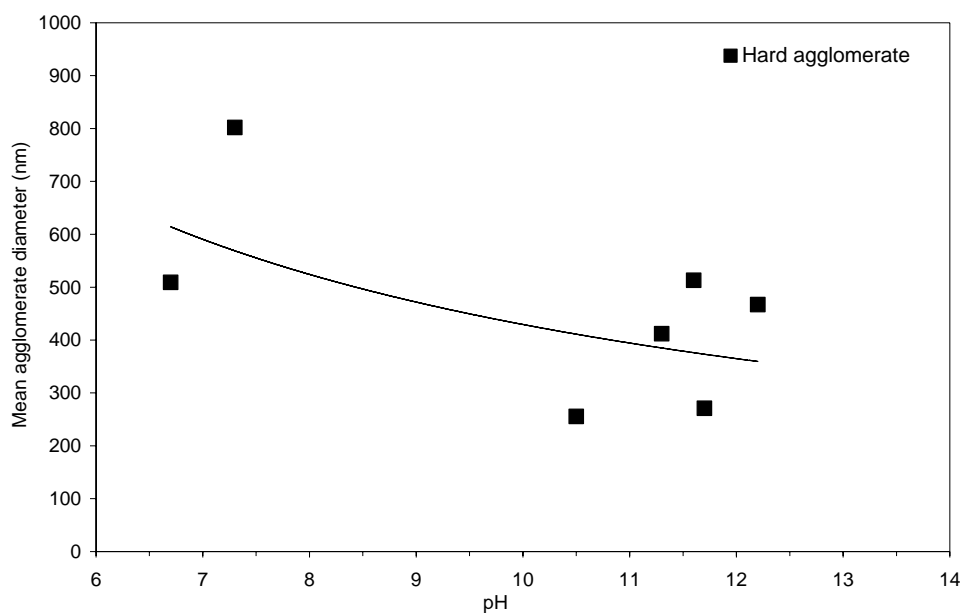


(a)

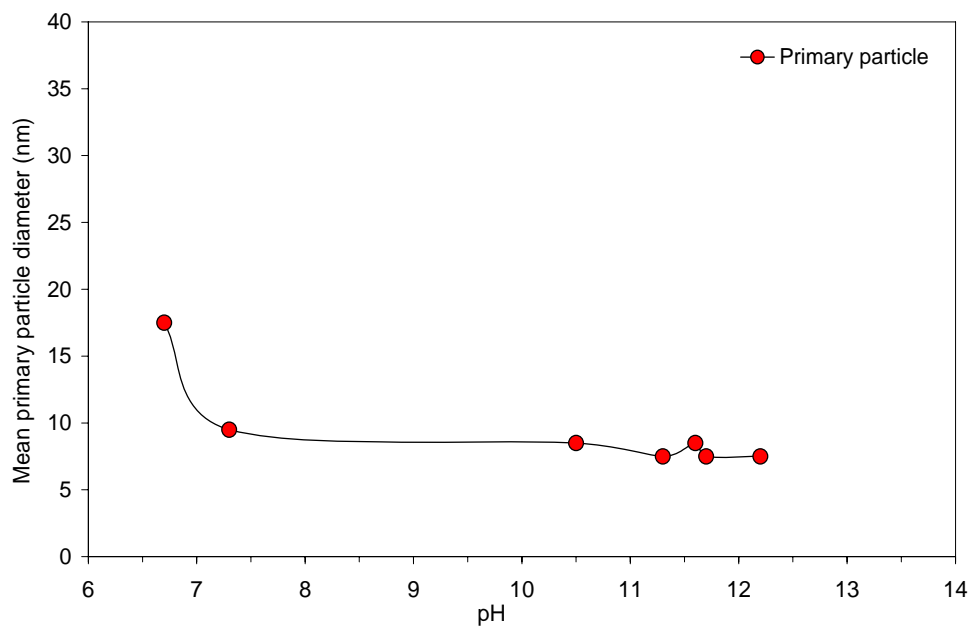


(b)

Figure 4-4: Effects of colliding particle size on collision frequency function in Brownian, laminar and turbulent agglomeration models (a) nominal primary particle size, d_{p1} , = 10nm and (b) nominal primary particle size, d_{p2} , = 200nm.

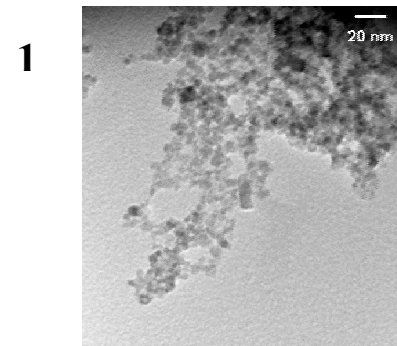
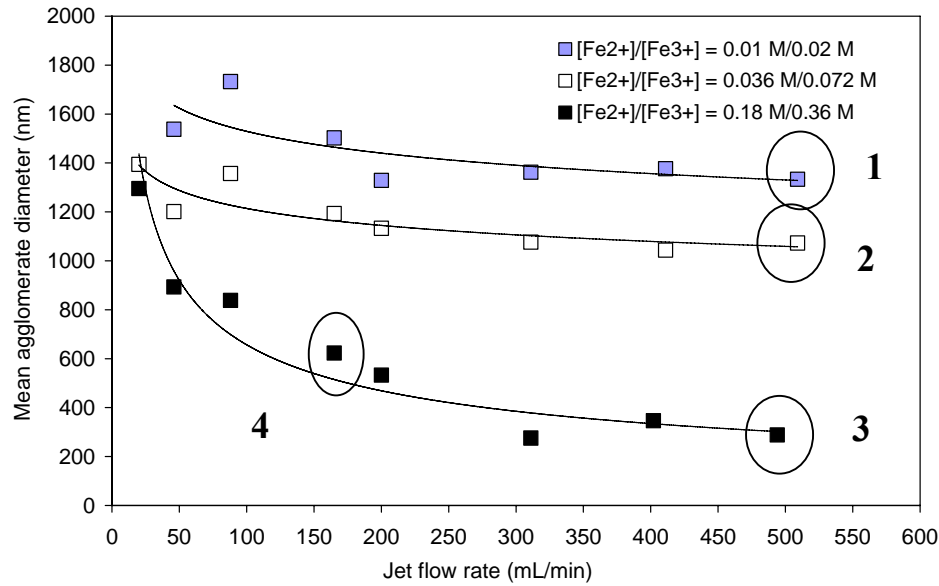


(a)

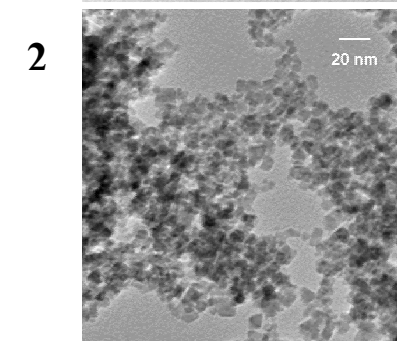


(b)

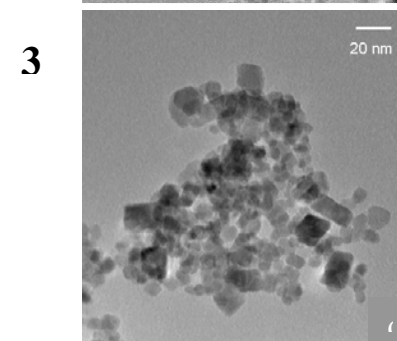
Figure 4-5: Effect of pH on iron oxide (a) agglomerate size and (b) primary particle size at flow rate = 500 mL/min. $[\text{Fe}^{2+}] = 0.05 \text{ M}$, $[\text{Fe}^{3+}] = 0.10 \text{ M}$ and $[\text{OH}^-]$ is varied between 0.39 M to 0.42 M in the experiments.



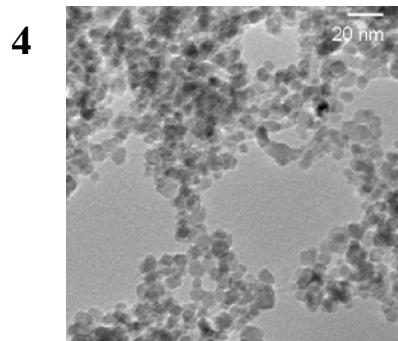
$d_p^* = 2.1 \text{ nm}$
 $d_p = 5.8 \text{ nm}$
 $d_{HA} = 1333 \text{ nm}$
 $n_{pp} = 3.7 \times 10^{16} \text{ s}^{-1}$
 $n_{HA} \approx 1200 \times 10^4$
 $N_{HA} \approx 3.1 \times 10^9 \text{ s}^{-1}$
 $N_g = 2.2 \times 10^{-21} \text{ moles/pp}$



$d_p^* = 2 \text{ nm}$
 $d_p = 7.4 \text{ nm}$
 $d_{HA} = 1072 \text{ nm}$
 $n_{pp} = 6.46 \times 10^{16} \text{ s}^{-1}$
 $n_{HA} \approx 300 \times 10^4$
 $N_{HA} \approx 21 \times 10^9 \text{ s}^{-1}$
 $N_g = 4.66 \times 10^{-21} \text{ moles/pp}$

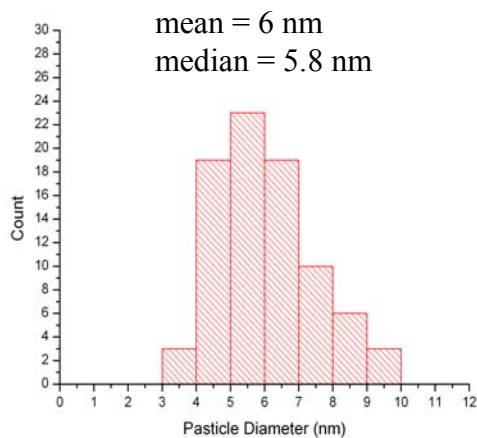


$d_p^* = 1.9 \text{ nm}$
 $d_p = 10.6 \text{ nm}$
 $d_{HA} = 288 \text{ nm}$
 $n_{pp} = 11 \times 10^{16} \text{ s}^{-1}$
 $n_{HA} \approx 2 \times 10^4$
 $N_{HA} \approx 5500 \times 10^9 \text{ s}^{-1}$
 $N_g = 1.38 \times 10^{-20} \text{ moles/pp}$

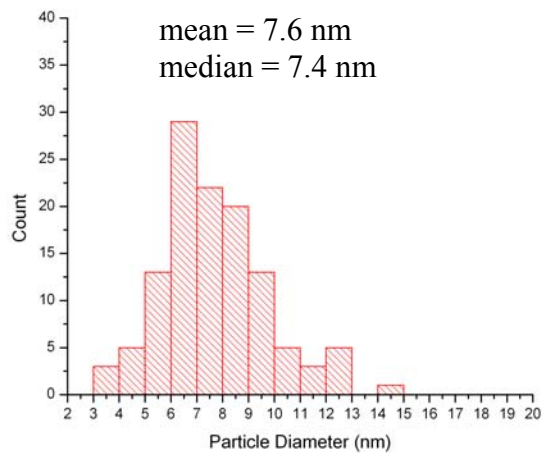


$d_p^* = 1.9 \text{ nm}$
 $d_p = 6.9 \text{ nm}$
 $d_{HA} = 623 \text{ nm}$
 $n_{pp} = 12.9 \times 10^{16} \text{ s}^{-1}$
 $n_{HA} \approx 73 \times 10^4$
 $N_{HA} \approx 180 \times 10^9 \text{ s}^{-1}$
 $N_g = 3.79 \times 10^{-21} \text{ moles/pp}$

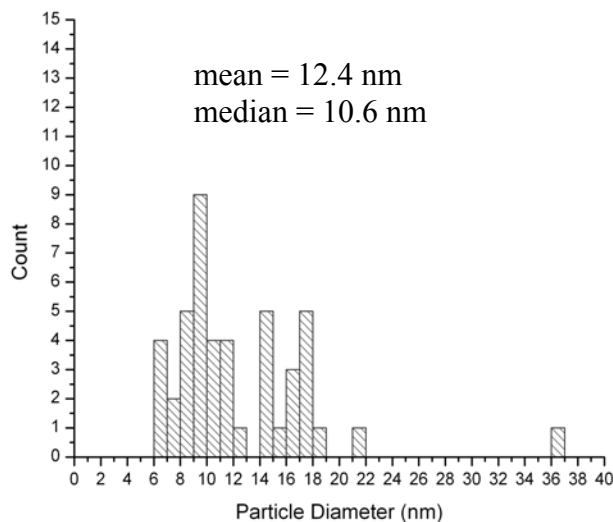
Figure 4-6: Effect of jet flow rate and varying ferrous-ferric concentration on iron oxide hard agglomerate size, nucleation and particle details at (1) $[\text{Fe}^{2+}] = 0.01 \text{ M}$ and 509 mL/min , (2) $[\text{Fe}^{2+}] = 0.036 \text{ M}$ and 509 mL/min , (3) $[\text{Fe}^{2+}] = 0.18 \text{ M}$ and 509 mL/min and (4) $[\text{Fe}^{2+}] = 0.18 \text{ M}$ and 165 mL/min . $[\text{Fe}^{3+}] = 2[\text{Fe}^{2+}]$, $[\text{OH}^-] = 1.45 \text{ M}$ in all experiments.



(a)

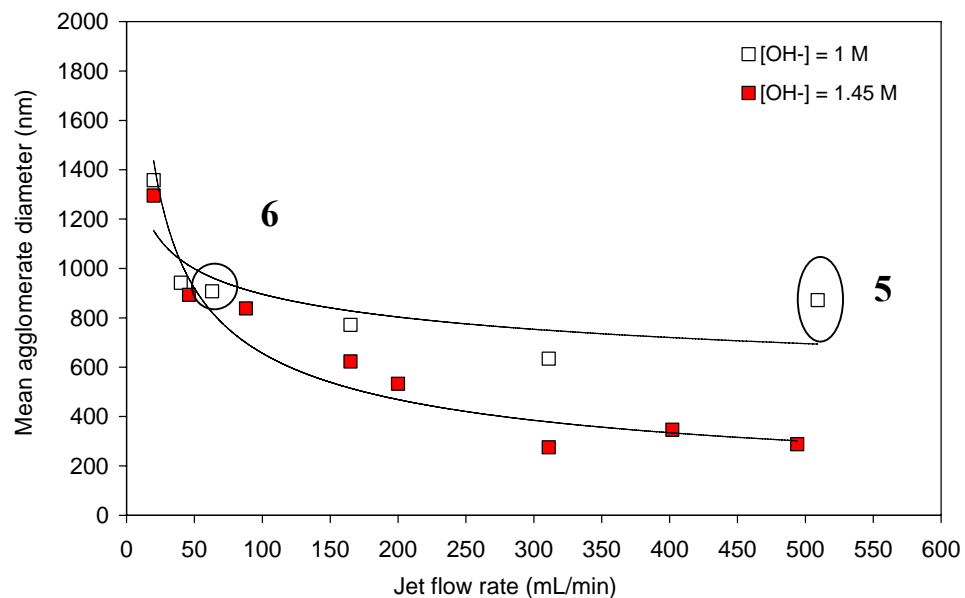


(b)

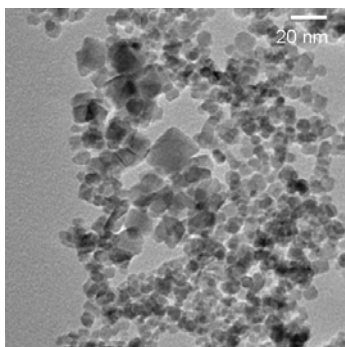


(c)

Figure 4-7: Primary PSD in a hard agglomerate at (a) $[\text{Fe}^{2+}] = 0.01 \text{ M}$, $[\text{Fe}^{3+}] = 0.02 \text{ M}$, (b) $[\text{Fe}^{2+}] = 0.036 \text{ M}$, $[\text{Fe}^{3+}] = 0.072 \text{ M}$ and (c) $[\text{Fe}^{2+}] = 0.18 \text{ M}$, $[\text{Fe}^{3+}] = 0.36 \text{ M}$. $[\text{OH}^-] = 1.45 \text{ M}$ and flow rate = 509 mL/min in all experiments.

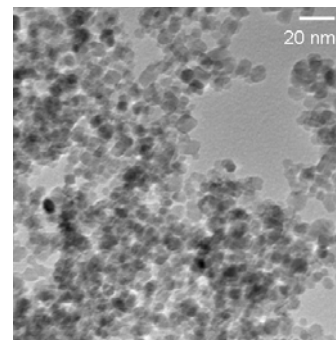


6



$d_p^* = 1.94 \text{ nm}$
 $d_p = 9.2 \text{ nm}$
 $d_{HA} = 907 \text{ nm}$
 $n_{pp} = 2.08 \times 10^{16} \text{ s}^{-1}$
 $n_{HA} \approx 96 \times 10^4$
 $N_{HA} \approx 22 \times 10^9 \text{ s}^{-1}$
 $N_g = 9.02 \times 10^{-21} \text{ moles/pp}$

5



$d_p^* = 1.94 \text{ nm}$
 $d_p = 8.84 \text{ nm}$
 $d_{HA} = 872 \text{ nm}$
 $n_{pp} = 19 \times 10^{16} \text{ s}^{-1}$
 $n_{HA} \approx 96 \times 10^4$
 $N_{HA} \approx 200 \times 10^9 \text{ s}^{-1}$
 $N_g = 7.99 \times 10^{-21} \text{ moles/pp}$

Figure 4-8: Effect of jet flow rate and varying ferrous-ferric concentration on iron oxide hard agglomerate size, nucleation and particle details at (5) $[\text{OH}^-] = 1 \text{ M}$ and 509 mL/min and (6) $[\text{OH}^-] = 1 \text{ M}$ and 63 mL/min . $[\text{Fe}^{3+}] = 2[\text{Fe}^{2+}] = 0.36 \text{ M}$ in all experiments

Literature cited

- Adler, P.M. and P.M. Mills, 1979, *Motion and Rupture of a Porous Sphere in a Linear Flow Field*, Journal of Rheology, **23(1)**, 25-38.
- Bäbler, M., 2008, *A Collision Efficiency Model for Flow-Induced Coagulation of Fractal Aggregates*, AIChE J., **54(7)**, 1748-1760.
- Bäbler, M., Mazzotti, M., Soos, M., Morbidelli, M. and Baldyga, J., 2008, *Modelling the Breakage of Solid Aggregates in Turbulent Flows*, AIChE Meeting, USA.
- Baldyga, J., W. Podgórska and R. Pohorecki, 1995, *Mixing-Precipitation Model with Application to Double Feed Semibatch Precipitation*, Chem. Eng. Sci., **50**, 1281.
- Baldyga, J., Jasińska, M. and W. Orciuch, W., 2002, *Barium Sulfate Agglomeration in a Pipe – An Experimental Study and CFD Modelling*, Proceedings of the 15th Int. Symp. On Ind. Crystallization, Italy, **1**, 149-154.
- Baldyga, J. and M. Jasińska, 2004, *Stirring and Mixing Effects in Agglomerative Precipitation*, Proceedings of the XXI International Congress of Theoretical and Applied Mechanics, Poland, **1**.
- Benet, N., Falk, L., Muhr, H. and E. Plasari, 1999, *Experimental Study of a Two-Impinging-Jet Mixing Device for Application in Precipitation Processes*, Proc. 14th International Symposium on the Industrial Crystals, 1007-1016.
- Bramley, A.S., M.J. Hounslow and R.L. Ryall, 1996, *Aggregation During Precipitation from Solution: A Method for Extracting Rates from Experimental Data*, J. Colloid and Interface Science, **183**, 155-165.
- Braun, B., 2003, *Aggregation and Agglomeration in Precipitative Crystallization*, PhD Thesis, Technische Universität München, Germany.
- Condon, J.M., 2001, *Investigation of Impinging Jet Crystallization for a Calcium Oxalate Model System*, PhD Thesis, Rutgers University, USA.

- David, R, P. Marchal, J.P. Klein and J. Villiermaux, 1991, *Crystallization and Precipitation Engineering –III. A Discrete Formulation of The Agglomeration Rate of Crystals in a Crystallization Process*, Chemical Engineering Science, **46**, 205-213.
- David, R, A.M. Paulaime, F. Espitalier and L. Rouleau, 2003, *Modelling of Multiple-Mechanism Agglomeration in a Crystallization Process*, Powder Technology, **130**, 338-344.
- Ehrl, L., Soos, M., Moussa, A.S. and M. Morbidelli, 2007, *Effect of Primary Particle Size on Steady-State Aggregates Size and Structure under Turbulent Conditions in Stirred Tank*, AIChE Meeting, USA.
- Ehrl, L., Soos, M., Hua, W. and M. Morbidelli, 2008, *The Effect of Flow-Field Heterogeneity on the Aggregation and Breakage on Colloidal Suspension Under Turbulent Conditions*, AIChE Meeting, USA.
- Faivre, D., P. Agrinier, N. Menguy, P. Zuddas, K. Pachana, A. Gloter, J.Y. Laval and F. Guyot, 2004, *Mineralogical and Isotropic Properties of Inorganic Nanocrystalline Magnetites*, Geochimica et Cosmochimica, **68 (21)**, 4395-4403.
- Gavi, E., Marchisio, D.L. and A.A. Barresi, 2008, *On Importance of Mixing for the Production of Nano-particles*, Disp. Sci. Tech., **29**, 548-554
- Gavi, E., Rivautella, L., Marchisio, D.L., Vanni, M., Barresi, A.A. and G. Baldi, 2007, *CFD Modelling of Nano-particle Precipitation in Confined Impinging Jet Reactors*, Chem. Eng. Res. And Des., **85(A5)**, 735-744.
- Goia, D.V. and E. Matijević, 1998, *Preparation of Monodispersed Metal Particles*, New J. Chem., **11**, 1203-1215.
- Gregory, J., 1989, *Fundamentals of Flocculation*, Critical Reviews in Environmental Control, **19(3)**, 185-230.
- Hollander, E., 2001, *Shear Induced Agglomeration and Mixing*, PhD Thesis, Technische Universiteit Delft, Netherlands.

- Johnson, B.K., 2003, *Flash NanoPrecipitation of Organic Actives via Confined Micromixing and Block Copolymer Stabilization*, Ph.D. Thesis: Volume 1 and 2, Princeton University, USA.
- Johnson, B.K. and R.K. Prud'homme, 2003, *Chemical Processing and Micromixing in Confined Impinging Jets*, *AIChE Journal*, **49 (9)**, 2264-2282.
- Jolivet, J.P., Tronc, E. and C. Chaneac, 2002, *Synthesis of Iron Oxide Based Magnetic Nanoparticles and Composites*, *C. R. Chimie*, **5**, 659-664.
- Jolivet, J.P., Froidefond, C., Pottier, A., Chaneac, C., Cassaignon, S., Tronc, E. and P. Euzen, 2004, *Size Tailoring of Oxide Nanoparticles by Precipitation in Aqueous Medium. A Semi-Quantitative Modelling*, *Journal of Material Chemistry*, **14**, 3281-3288.
- Koparde V.N. and P.T. Cummings, 2005, *Molecular Dynamics Simulation of Titanium Dioxide Nanoparticle Sintering*, *J. Phys. Chem. B*, **109**, 24280-24287.
- Kusters, K.A., Wijers, J.G. and D. Thoenes, 1997, *Aggregation Kinetics of Small Particles in Agitated Vessels*, *Chem. Eng. Sci.*, **52(1)**, 107-121.
- Lieser, K.H., 1969, *Steps in Precipitation Reactions*, *Angew. Chem. Internat. Edt.*, **8 (3)**, 188-202.
- Lin, C.L., C.F. Lee and W.Y. Chui, 2005, *Preparation and Properties of Poly(acrylic acid)Oligomer Stabilized Superparamagnetic Ferrofluid*, *Journal of Colloid and Interface Science*, **291**, 411-420.
- Mahajan, A.J. and D.J. Kirwan, 1996, *Micromixing Effects in a Two-Impinging-Jets Precipitator*, *AIChE Journal*, **42(7)**, 1801-1814.
- Maity, D. and D.C. Agrawal, 2007, *Synthesis of Iron Oxide Nanoparticles Under Oxidizing Environment and their Stabilization in Aqueous and Non-Aqueous Media*, *Journal of Magnetism and Magnetic Materials*, **308**, 46-55.
- Marcant, B. and R. David, 1991, *Experimental Evidence for and Prediction of Micromixing Effects in Precipitation*, *AIChE J.*, **37(11)**, 1991.

- Marchisio, D.L., R.O. Fox, T. Cheng, E. Stroofer and A. Barreri, 2003, *CFD Study of Fine Particles Nucleation, Growth and Agglomeration*, Proceedings of the 11th European Conference on Mixing., **1**, 371-378.
- Marchisio, D.L., A.A. Barresi and M. Garbero, 2003, *Nucleation, Growth and Agglomeration in Barium Sulfate Turbulent Precipitation*, *AICHE J.*, **48(9)**, 2039-2050.
- Marchisio, D.L., M. Soos, J. Sefcik and M. Morbidelli, 2006, *Role of Turbulent Shear Rate Distribution in Aggregation and Breakage Processes*, *AICHE J.*, **52(1)**, 158-173.
- Marchisio, D.L., L. Rivautella and A. Barreri, 2006, *Design and Scale-Up of Chemical Reactors for Nanoparticle Precipitation*, *AICHE J.*, **52 (5)**, 1877-1887.
- Masliyah, J.H. and S. Bhattacharjee, 2006, *Electrokinetic and Colloid Transport Phenomena*, Wiley-Interscience, N. J., USA
- Mersmann, 1995, *Crystallization Technology Handbook*, Marcel Dekker, N.Y. USA
- Mersmann, 2001, *Crystallization Technology Handbook*, Second Edition, Marcel Dekker, N.Y. USA
- Muhle K., 1993, *Floc Stability in Laminar and Turbulent Flows, Coagulation and Flocculation: Theory and Applications*, Marcel Dekker Inc, USA.
- Mumtaz, H.S., Hounslow, M.J., Seaton, N.A. and W.R. Paterson, 1997, *Orthokinetic Aggregation during Precipitation during Precipitation: A Computational Model for Calcium Oxalate Monohydrate*, *Trans IChemE*, **75**, 152-159.
- Midler, M., E. Paul, E. Wittington, M. Futran, P. Liu, J. Hsu and S. Pan, *Crystallization Method to Improve Crystal Structure and Size*, US Patent 5,314,506, 1994
- Nielsen, A.E., 1964, *Kinetics of Precipitation*, Macmillian, N.Y., USA.

- Nielsen A.H.E. and J.M. Toft, 1984, *Electrolyte Crystal Growth Kinetics*, J. Crystal Growth, **67**, 278.
- Nyvt, J. and M. Karel, 1985, *Crystallization, Agglomeration*, Cryst. Res. Technol., **20**, 173.
- Parker, D.S., Kaufman, W.J. and D. Jenkins, 1972, *Floc Breakup in Turbulent Flocculation Processes*, ASCE Journal of the Sanitary Engineering Division, **98(SA1)**, 79-99.
- Paul, E.L., Atiemo-Obeng, V.A. and S.M. Kresta, 2004, *Handbook of Industrial Mixing: Science and Practice*, Wiley-Interscience, USA.
- Roelands, M., J. Derksen, J. Horst, H. Kramer and P. Jansens, 2003, *An Analysis of Mixing in a Typical Experimental Setup to Measure Nucleation Rates of Precipitation Processes*, Chem. Eng. Technol., **26 (3)**, 296-302.
- Saffman, P.G. and J.S. Turner, 1956, *Collision of Drops in Turbulent Clouds*, Journal of Fluid Mechanics, **1**, 16-30.
- Schuetz, H.C. and M. Piesche, 2002, *A Model of the Coagulation Process with Solid Particles and Flocs in Turbulent Flow*, Chem. Engineering Science, **57**, 4357-4368.
- Schwarzer, H.C., and W. Peukert, 2002, *Experimental Investigation into the Influence of Mixing on Nanoparticle Precipitation*, Chem. Eng. Technol, **25 (6)**, 657-661.
- Schwarzer, H.C., and W. Peukert, 2004, *Combined Experimental/Numerical Study on the Precipitation of Nanoparticles*, AIChE Journal, **50 (12)**, 3234-3447.
- Schwarzer, H.C., and W. Peukert, 2005, *Prediction of Aggregation Kinetics Based on Surface Properties of Nanoparticles*, Chem. Eng. Science, **60**, 11-25.
- Selomulya, C., 2001, *The Effect of Shear on Flocculation and Floc Size/Structure*, PhD Thesis, University of New South Wales, Australia.

- Siddiqui, S.W., Y. Zhao, A. Kukukova, and S.M. Kresta, 2009, *Mixing Characteristics of a Confined Impinging Jet Reactor: Dissipation Rate, Homogeneous and Heterogeneous Reactions, and Effect of Unequal Flowrates on Performance*, Ind. Eng. Chem. Res. (Article in Press)
- Sonntag, R.C. and Russel, 1987, *Structure and Breakup of Floccs Subjected to Fluid Stresses: 2. Theory*, Journal of Colloid & Interface Science, **115(2)**, 378-389.
- Tronc, E., P. Belleville, J.P. Jolivet and J. Livage, 1992, *Transformation of Ferric Hydroxide into Spinel by Fe^{II} Adsorption*, Langmuir, **8**, 313-319.
- Unwin, P., 2008, *Nanoparticle Sintering: A Study by Molecular Dynamics Simulations*, Technical Report
- Yeung, A.K.C. and Pelton, R., 1996, *Effect of the Shear on the Strength of Polymer-induced Floccs*, Journal of Colloid & Interface Science, **196**, 113-115.
- Zeidan, M., Xu, B.H., Jia, X. and Williams, R.A., 2007, *Simulation of Aggregate Deformation and Breakup in Simple Shear Flows using a Combined Continuum and Discrete Model*, Chem. Eng. Res. And Des., **85(A12)**, 1645-1654.
- Zhu, H. and R.S. Averback, 1996, *Sintering Processes of Two Nanoparticles: A Study by Molecular-Dynamics Simulations*, Philosophical Magazine Letters, **73**, 27-33.

Chapter 5

Scale-up of the Confined Impinging Jet Reactor: Energy Dissipation, Reaction and Effect of Unequal Flow

Introduction

The CIJR offers high mixing efficiency as required for high product quality in many chemical/pharmaceutical applications (Johnson et al., 2003; Marchisio et al., 2006 and Gavi et al. 2007). This work is a continuation of Siddiqui et al. (2009) who characterized mixing in the CIJR by estimating energy dissipation rates and quantifying the hydrodynamic effects on product yield and precipitate particle size for the mixing sensitive iodide-iodate and iron oxide precipitation reactions respectively. The CIJR studied by Siddiqui et al. (2009) had inlet diameters of 1 mm, a mixing volume diameter of 4.76 mm, residence time of 10^{-2} to 10^{-1} seconds and mixing time of 10^{-3} to 10^{-2} s (equation. 5-5). The average energy dissipation was found to vary from 20 W/kg to 6800 W/kg over the range of flow rates investigated. CFD showed that all the incoming fluid must pass through the maximum energy dissipation zone close to the impingement point where the energy dissipation was up to 40X higher than the average value in the mixer. Under unequal inlet flow conditions the energy dissipation retained 84% of the balanced flow value all the way to a 30% difference in flow rates. The product yield values for the homogeneous reaction showed stable results up to a 20-25% imbalance in flow rate.

Despite the large production capacity of even the small CIJR, scale-up is desirable for a further increase in production. In this work we study the effect of equal and unequal flow rates (mixing) on energy dissipation, and then extend these results to product yield of a mixing sensitive iodide-iodate reaction in scaled-up CIJRs. Three geometrically similar scale-up cases have been studied: base case, 2X scale-up and 4X scale-up. Figure 5-1 (a) and Table 5-1 give the complete dimensions of the reactors.

Mixing in two impinging jets has been studied by Mahajan and Kirwan (1996). They found that the larger the jet diameter, the larger the Reynolds number (Re) required to achieve the same micromixing quality.

$$\text{Re}_j = \frac{d_i V_i \rho}{\mu} \quad (5-1)$$

They argued that the micromixing characteristic time could be used to scale up the impinging jet mixer. To achieve constant characteristic mixing time, the same jet velocity needs to be maintained at the new diameter.

$$\tau_m \propto \frac{1}{D_{AB}} \left[\frac{\bar{\rho} \bar{v}^3 d_2 V_{IJR}}{\rho_2 v_2^3 \text{Re}_2^3 \left(1 + \frac{\dot{m}_2}{\dot{m}_1}\right)} \right]^{0.5} \quad (5-2)$$

In the case of a change in reaction conditions upon scale up, they recommended maintaining constant Damkohler number (Da), again scaling the jet velocity to achieve the same micromixing conditions.

$$Da = \frac{\tau_m}{\tau_r} = \frac{r \cdot \tau_m}{C_{Ao}} \quad (5-3)$$

Characteristic time constant (τ_r) for n^{th} order chemical kinetics is given by Baldyga and Pohorecki (1995).

$$\tau_r = \frac{1}{k_n (C_{Ao})^{n-1}} \quad (5-4)$$

Johnson and Prud'homme (2003) reviewed works by Mahajan and Kirwan (1996) and Schaer et al. (1999) and agreed that jet velocity was an important scale-up variable, but also found that maintaining the same velocity on scale-up wasn't sufficient to ensure the equivalent process performance. Jet Reynolds number was also not sufficient to ensure the same micromixing performance and reaction-conversion in geometrically similar reactors. They argued that direct scale-up could be accomplished by achieving an identical micromixing time, for which a scaling relationship was derived in terms of geometric and operating parameters and an experimentally determined scaling factor K_{CIJR} (=1470). The

expression is limited to Reynolds numbers where momentum diffusion is the active mixing mechanism.

$$\tau_m = 1470 \frac{v^{\frac{1}{2}} \Delta^{\frac{3}{2}} d_1^{\frac{1}{2}}}{2V_1^{\frac{3}{2}}} \frac{1}{\left[\left(\frac{\rho_1}{\rho_3} \right)^{\frac{1}{2}} \right]} \frac{1}{\left[\left(1 + \frac{\dot{m}_1}{\dot{m}_2} \right)^{\frac{1}{2}} \right]} \quad (5-5)$$

Marchisio et al. (2006) studied the design and scale-up of the CIJR for nanoparticle production. They showed how CFD and a simple precipitation model could be used to derive scale-up criteria for the production of nanoparticles. The reactor performance was tested under different mixing and reaction conditions where the Damkoehler number (Da) was held constant on scale-up. They concluded that the mean particle size at the reactor outlet for the small (jet diameter = 1mm) and big reactor (jet diameter = 2mm) could be correlated by Da, i.e. the ratio between the mixing and precipitation time calculated with CFD and the precipitation model. They observed that when the mixing was much slower than the chemical reaction (Da >> 1), big particles were obtained; whereas when mixing was faster than the chemical reaction rate (Da < 1) submicron particles were obtained.

Gavi et al. (2007) used CFD to model mixing and homogeneous reaction in the CIJR and to develop a scale-up criterion. They observed that the reaction-conversions corresponding to different geometries did not correlate well at the same Reynolds number and thus concluded that jet Reynolds number was not the appropriate scaling variable. Instead, the Damkoehler number could be used as a scaling parameter where conversion curves for various geometries were seen to converge. The experimental data from Johnson for two geometries (jet diameter = 0.5 mm and 1mm with mixing chamber diameter of 4.76 mm) were validated with CFD.

As evident from the above discussion, for geometrically similar scale-up, other parameters need to be scaled-up to obtain the same micromixing effects. In this work we explore the effect of scaling based on jet Reynolds number (Re_j), time of flight (t_f), jet momentum, residence time (τ_{res}), and Damkoehler number

(Da) on energy dissipation rate and product yield (of iodide-iodate reaction) in 2X scale-up and 4X scale-up CIJR. Jet momentum and Reynolds number are defined at the average inlet jet velocity and at the incoming jet diameter. Time of flight (t_f) is the time it takes for the incoming jet to impinge (with other jet) at the centre of the jet spacing in the mixer.

$$t_f = \frac{D_c}{V_1 + V_2} \quad (5-6)$$

Residence time (τ_r) is the time fluid stays in the mixer.

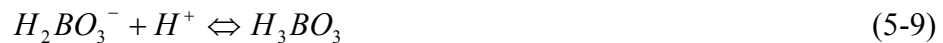
$$\tau_{res} = \frac{V_{CIJR}}{Q_{total}} = \frac{V_{CIJR}}{Q_1 + Q_2} \quad (5-7)$$

In this work the mixing efficiency of scale-up geometries under varying hydrodynamic conditions is characterized by the energy dissipation that is computed through mechanical energy balance approach across the mixing volume and yield of mixing sensitive iodide-iodate reaction. Operating robustness is determined by unequal flow experiments where the effect of unbalanced flow and unequal momentum on energy dissipation rate and product yield is analyzed.

The energy dissipation rate (ε) is estimated from the following expression (Siddiqui et al., 2009) where the pressure drop across the mixing volume (Δp) is measured between the inlets and the outlet and taking the average. The kinetic energy change is the difference in total KE between the inlets and the outlet in the CIJR.

$$\bar{\varepsilon}_{tot} = \frac{2Q_i \Delta p + \Delta KE}{\rho V_{CIJR}} \quad (5-8)$$

The three-step competitive-parallel iodide-iodate model reaction system has been extensively used as a micromixing probe for comparing various mixing geometries and varying mixing conditions in CIJR (Siddiqui et al., 2009), where the neutralization reaction is the fast and product-forming reaction.



$H_2BO_3^-$ ions are obtained from the coexisting H_3BO_3 and NaOH in the reaction mixture, which is a buffer solution. The slower reaction (Dushman reaction)

proceeds by forming byproduct (I₂) with reaction between iodide, iodate and hydrogen ions:



The byproduct iodine (I₂) further reacts with iodide ions to form the byproduct triiodide ions (I₃⁻).



Iodine (I₂) and triiodide (I₃⁻) are the byproducts. While the triiodide concentration is estimated from the measured absorbance (using a spectrophotometer) of the product solution, the iodine concentration is determined by mole balance. Under imperfect mixing conditions, local high concentrations of H⁺ occur in the reaction mixture facilitating byproduct formation. The product selectivity is thus determined by the ratio of the rate constants.

The reaction rate corresponding to the slow reaction is (Guichardon et al., 2000):

$$r = k[I^-]^2[IO_3^-][H^+]^2 \quad (5-12)$$

Here the rate constant k is $1.3 \times 10^9 \text{ M}^{-4} \text{ s}^{-1}$ at 25°C. Any effect of ionic strength on the rate constant of the slower reaction has been neglected in this study. The product yield of the reaction depends on the number of moles of the limiting reagent (H⁺) consumed in byproduct formation and is estimated as:

$$Y = 1 - \frac{\text{moles of H}^+ \text{ consumed in byproducts}}{\text{total moles of H}^+ \text{ added to the system}} \quad (5-13)$$

Much has been said about using iodide-iodate as a micromixing probe (Siddiqui et al., 2009; by Kölbl, 2008; Kölbl et al., 2008 and Bourne, 2008). Kölbl (2008) states that although the iodide-iodate reaction is reliable and easy, it has shortcomings for quantitative measures of absolute mixing times due to the uncertainty in reaction kinetics of the Dushman reaction, iodine precipitation and spectroscopic measurement limitation at high reactant concentrations. Kölbl et al. (2008) argues that using the iodide-iodate reaction, different mixing devices can only be compared quantitatively when measured at the same reactant concentrations. They argue that at very high reactant concentration, absorbance values may be out of range for the Beer-Lambert's law which may limit yield

measurements. The reactant concentrations thus need to be chosen carefully. They report that slow mixing devices need to be probed at low reactant concentration, while fast mixing devices require high reactant concentrations so as to meet the detection limits of the spectrophotometers. The shortcomings of the reaction model were also discussed by Bourne (2008), who concluded that though the quantitative conclusions need to be considered carefully, the results could be used for qualitative comparisons.

The primary focus of this research is to determine the effect of scale-up of the CIJR on its mixing efficiency. A chemical marker (product yield of iodide-iodate reaction) and a non-chemical marker (energy dissipation) are used to estimate micromixing efficiency under balanced flow and momentum conditions. Operational robustness under unequal flow conditions is studied using the same two methods. The second objective is to determine a set of scaling parameters which can be successfully used to scale-up micromixing performance in CIJR. The third objective is to determine if there is a limit on geometric scale-up where micromixing becomes poor and the impinging jets are no longer effectively confined.

Experimental setup and operating conditions

Figure 5-1 and Table 5-1 give the dimensions of the CIJR and the arrangement of the pressure transducers (Omegadyne, PX600, 0-200 psig miniature flush diaphragm transducer). For pressure drop measurements the pressure taps are located within 1mm of the inlets and the outlet to avoid any pressure drop associated with the pipes. The pressure lines leading to pressure ports are filled with water prior to experiments. The pressure transducers are connected to a data-logging system where the pressure data is recorded for two minutes for each experimental run. For the product yield experiments, mixer geometries with no pressure ports were used.

Constant pulse-free flows to the CIJR were provided by micropump-head (Series GB, external gear pump, max flow rate 4L/min) and pump drives (MCP-Z standard, IDEX corporation). The pumps were calibrated by mass and

volumetric flow methods for the whole range of flow rates under study. A flow visualization technique was also used to monitor flow stability under balanced flow conditions.

Iodide-Iodate reaction

Reagent solutions for the product yield experiments were prepared in Reverse Osmosis water using potassium iodate, potassium iodide, sodium hydroxide, boric acid powder and 10N sulfuric acid solution. Potassium iodide and iodate solutions were prepared in deoxygenated water to prevent any oxidation of iodide ions to iodine prior to reaction. A detailed solution preparation methodology appears elsewhere (Siddiqui et al., 2009). Table 5-2 gives the solution concentrations corresponding to the inlet jet streams. Under equal flow rate conditions, the mean reagent concentrations in the reactor are half the inlet concentration. For unequal flow rates, the mean reagent concentrations in the reactor depend on the ratio of the flow imbalance.

Post reaction, the collected product samples were put to light absorbance measurements at a wavelength of 352 nm using an optical probe (7mm path length). The extinction coefficient was obtained by running a series of absorbance measurements with standard triiodide solutions and was estimated to be 1914.8 m²/mol. The extinction coefficient was sensitive to the fiber optic and the water source used for making the standard solutions. Details are discussed elsewhere (Siddiqui et al., 2008). The experiments were highly reproducible. Error bars are not been plotted on the yield results because they are roughly of the same size as the symbols.

Results

The results are divided into two parts. In the first part, mixing in the scale-up geometries is characterized for equal momentum and balanced flow conditions in terms of energy dissipation and product yield of the iodide-iodate reaction. The various scale-up criteria tested are listed in Table 5-3. In the second part the robustness of the CIJR is investigated for unbalanced flow in the 2X scale-up and

4X scale-up. The effect of flow unbalance on the energy dissipation rate and on the product yield is investigated.

Balanced Flow, Equal Momentum

Energy Dissipation Rate

Figures 5-2 to 5-5 show the effect of scale-up on energy dissipation rate. The scaling parameters are jet Reynolds number, jet momentum, time of flight and residence time. Energy dissipation increases with Reynolds number (Re), however; at constant Re (Figure 5-2), the dissipation decreases on scale-up. At a constant Re, both the jet velocity and jet pressure head decrease with an increase in jet diameter, causing a decrease in the mechanical energy change from the inlets to the exit. This leads to a decrease in the energy dissipation in scale-up CIJRs operating at the same Re. At low flow rates, the difference in energy dissipation between different CIJRs is small but it gets larger at high Reynolds numbers. At Re = 2000, the dissipation values are similar. At Re = 10,000 a 6X drop in dissipation is measured for a 4-fold scale-up. A similar drop in energy dissipation on scale-up is seen when jet momentum is used as the scaling parameter (Figure 5-3). As with the Re, energy dissipation is seen to increase with an increase in jet momentum for each of the CIJRs. At constant jet momentum, both pressure and jet velocity decrease with an increase in jet diameter, leading to a decrease in energy dissipation on scale-up. A greater increase in energy dissipation is seen in the original CIJR (base case) than in the 2X scale-up or 4X scale-up CIJRs for an equal increment in jet momentum.

Scale-up of the mixing chamber leads to an increase in both the jet inter-spacing and the mixing volume, which increases the time-of-flight (Figure 5-4) and residence time (Figure 5-5) respectively at constant flow rate. Energy dissipation scales up with none of these parameters. Energy dissipation also increases with an increase of time of flight. From Table 5-3 a 2.4X decrease in energy dissipation is seen for a 10% increase in residence time on 2X scale-up. Likewise a 5X decrease in energy dissipation is seen for a 53% increase in residence time on 4X scale-up.

A comparison of the effect of scale-up on energy dissipation in terms of the above 4 scaling parameters indicates that energy dissipation can be scaled with Re and jet momentum up to $Re = 2000$ and momentum = 0.005 kg m/s^2 respectively. Beyond this point the differences between the geometries begin to amplify. The time of flight and residence time fail to scale energy dissipation in the geometries.

Product Yield in Iodide-Iodate Reaction

Figure 5-6 shows the effect of scale-up on product yield with Reynolds number as the scaling parameter. The product yield increases with an increase in Re , however; at constant Re it decreases with scale-up this effect on is most pronounced at a 4X scale-up. Though the product yield decreases with scale-up at all hydrogen concentrations, the lowest yields are obtained at higher concentrations. On scale-up at constant Re , the dissipation drops resulting in high local concentrations and an increase in tri-iodide ion production. The product yield is quite similar at high Re (> 4000) for a 2X scale-up CIJR at both low and high hydrogen concentration; however, the 4X scale-up CIJR shows a drop in product yield at all concentrations and flow conditions, with the exception of a data point.

Figure 5-7 shows the scaling of product yield with Damkoehler number. The yield decreases with increasing Da at all hydrogen concentrations as expected. At the higher hydrogen concentration, the curves fall on top of each other suggesting that Da could be successfully used to scale-up the micromixing performance of CIJR's. The curves do not collapse at low hydrogen concentration. As the local concentration varies more in the bigger mixing volume (on scale-up) with smaller energy available for mixing, lower product yields are obtained at higher hydrogen concentration. This effect amplifies with 4X scale-up and at high hydrogen concentration, forcing the graphs for all 3 geometries to fall on top of each other. The 4X scale-up gives the lowest product yield and higher Da , a reflection of the drop in dissipation on scale-up. The product yield curves for the original CIJR and 2X scale-up overlap indicating

similar micromixing effects on 2X scale-up. The Da can thus be used conveniently for 2X scale-up but not further.

Figure 5-8 and Figure 5-9 show the effect of scale-up on product yield with energy dissipation and jet momentum as the scaling parameters. Product yield increases with an increase in energy dissipation as expected. Mixing efficiency is proportional to energy dissipation, so high product yield are obtained at high dissipation. The plots for the original and 2X scale-up appear to converge at ~ 100 W/kg after which the product yield varies only very slightly with increasing dissipation. Lower product yield is obtained at high hydrogen concentration. The product yield also increases with jet momentum, however; when jet momentum is held constant on scale-up, the 4X scale-up CIJR gives a lower product yield than the smaller CIJRs. The jet velocity decreases with an increase in jet diameter, leading to a decrease in jet momentum and the mechanical (KE and pressure) available for mixing. Whereas energy dissipation can be used to scale-up micromixing in CIJR up to 2X, jet momentum cannot be. 4X scale-up completely fails to scale-up up either of these. This is due to a sharp drop in energy dissipation and jet momentum with increase in jet diameter and mixing volume scale-up.

Figure 5-10 and Figure 5-11 show the effect of scale up on product yield with residence time and time-of-flight. Product yield decreases with an increase in either residence time or time-of-flight. It is seen that product yield trends corresponding to original and 2X scale-up for residence time fall on top of each other. Product yield however fails to scale-up with time of flight. This is in contrary to the energy dissipation failing to scale-up with either of the scaling factors.

Of the various scaling parameters tested, it is concluded that Reynolds number and jet momentum can be used to scale-up energy dissipation of CIJR (up to 2-fold) at low Re conditions and low jet momentum conditions. Da , energy dissipation and residence time can also be used to scale-up mixing performance up to a size scale-up factor of 2. Both energy dissipation and product yield drop upon scaling to 4X scale-up. 4X scale-up CIJR does not

consistently scale-up with any of the scaling factors. This indicates that a 2X scale-up is the limit for optimum mixing performance of CIJR.

Unequal Flow, Unequal Momentum

Normalized Energy Dissipation Rate

Figure 5-12 (a) shows the effect of unequal flows on energy dissipation calculated from a mechanical energy balance on the original CIJR. A rapid decrease in energy dissipation is observed with a drop in stream 2 flow rate for Reynolds number less than 3500. The dissipation stabilizes at a flow rate of 165 mL/min, where the transition to turbulent flow is evident. A flow imbalance at high Re gives only a small drop in the dissipation: 84% of the maximum energy dissipation is retained until a 30% difference in flow. Figure 5-12 (b) shows the effect of unequal flow rates on energy dissipation in the 2X scale-up. Again in the limit of fully turbulent flow, 81% of the maximum energy dissipation is retained all the way to a 30% drop in stream-2 flow rate. Unreliable results were obtained for unbalanced flow experiments in the 4X scale-up. At low flow rates and under unequal flow and momentum conditions, the jets failed to impinge or fill the mixing volume, thus violating the basic principle of the CIJR.

Product Yield in Iodide-Iodate Reaction

Figure 5-13 shows the effect of a reduction in sulfuric acid (hydrogen source) flow rate at varying hydrogen concentrations in a 2X scale-up CIJR. At all hydrogen concentrations, relatively low product yields are obtained at low Reynolds numbers, however; at high Reynolds numbers (≥ 2000) and all flow inequalities, the product yield is stable. With a drop in sulfuric acid flow, a high reaction pH is always maintained and thus any byproduct iodine formed is due to the inefficient local mixing conditions. The variation in the product yield is surprisingly stable which indicates that high local mixing is achieved in CIJR. A lower product yield is obtained at higher hydrogen concentration though yield is stable despite inequality in flow rates. Similar observations were made for mixing performance of 4X scale-up in Figure 5-14. Lower product yields are

obtained at high hydrogen concentrations than at low concentrations. Relatively low yield is obtained at low Reynolds number and all flow inequalities, however; at high Reynolds number (≥ 2000) a higher yield with little variation due to flow imbalance is seen. Smaller CIJR give a larger product yield than the scaled-up CIJR. 4X scale-up gives the lowest product yield.

Both the balanced and imbalanced flow results show that the CIJR can be scaled up to 2X with comparable mixing performance but the 4X scale-up gives poor mixing performance and low product yield.

Conclusions

Energy dissipation in three sizes of CIJR has been determined from a mechanical energy balance. The energy dissipation decreases on scale-up due to decrease in jet velocity and the pressure head. At fully turbulent Re limit of 10,000, the overall energy dissipation is 6800, 3000 and 1250 W/kg in original, 2X and 4X scale-ups respectively. The difference in the energy dissipation in the 3 geometries corresponding to same Re increase with Reynolds number.

Various scale-up criteria (Reynolds number, time of flight, residence time, jet momentum and Damkoehler number) and their effect on mixing performance in terms of energy dissipation and the product yield of the iodide-iodate reaction have been studied. The mixing performance curves merge on 2X scale-up with Damkoehler number (Da) scaling. Residence time can also be used to scale-up mixing performance for a 2X scale-up. Re and jet momentum can be used to scale-up energy dissipation for very low Re and jet momentum values.

Under unbalanced flow conditions in the fully turbulent regime (Re = 10,000), the 2-fold geometry retains 84% of the balanced flow dissipation all the way to a 30% difference in flow rate. The product yield values are surprisingly stable for up to a 30% flow unbalance in both the 2X and 4X scale-up. The results show that the 4-fold scale-up gives poor mixing performance and 2X scale-up is likely the upper limit for achieving a balance between high production capacity and good micromixing capability.

Tables

Table 5-1: Dimensions of the three sizes of CIJR

	Original (base case)	2X	4X
Variables	Dimensions (mm)	Dimensions (mm)	Dimensions (mm)
r_c	2.38	4.76	9.52
d_i	1	2	4
d_o	1.5	3	6
h_1	3.31	6.62	13.24
h_2	5.21	10.42	20.84
h_3	2.38	4.76	9.52
L_1	20	40	80
L_2	30	60	120
D_c	4.76	9.52	19.04

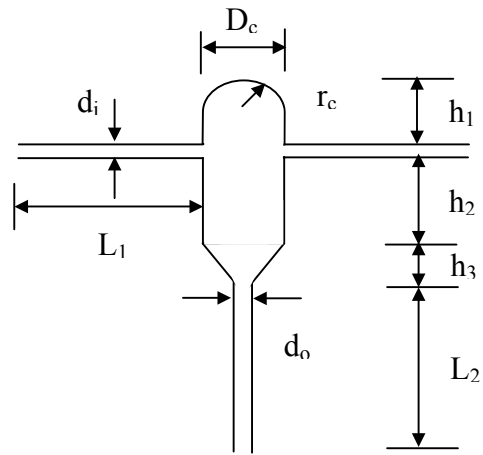
Table 5-2: Reagent concentrations for the iodide-iodate reaction

Feed stream (inlet)	Reagent	Conc. 1 (M)	Conc. 2 (M)
1	I^-	0.0234	0.0234
1	IO_3^-	0.00466	0.00466
1	$H_2BO_3^-$	0.1818	0.1818
2	H^+	0.0936	0.1818

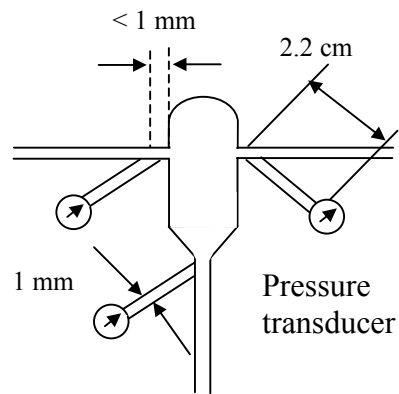
Table 5-3: Scale-up criterion

Geometric scale-up	Flow rate (mL/min)	Re_j	Residence time (s)	Time of flight (s)	ε_{avg} (W/kg)	Jet momentum (Kg.m/s²)	Da [H⁺] = 0.0936M	Da [H⁺] = 0.1818M
Original	30	637	0.17	0.00375	1	0.00032	0.30493	1.15035
	40	849	0.1275	0.0028	2	0.000533	0.19806	0.74718
	56	1189	0.09107	0.002	11	0.00112	0.11956	0.45106
	63	1338	0.08095	0.00178	13	0.00137	0.10020	0.37801
	88	1868	0.05699	0.001274	40	0.00283	0.06069	0.22898
	165	3503	0.03094	0.00068	231	0.00962	0.02364	0.08918
	200	4246	0.02548	0.00056	420	0.01418	0.01771	0.06683
	311	6603	0.01638	0.00036	1592	0.0343	0.00914	0.03446
	509	10807	0.01002	0.000227	6802	0.08638	0.00436	0.01646
2X	56	594	0.72604	0.01603	1	0.000277	3.82600	14.43380
	194	2059	0.20958	0.004623	15	0.00333	0.59337	2.23852
	379	4024	0.10728	0.002366	178	0.01271	0.21730	0.81979
	1038	11019	0.03917	0.000864	2871	0.09532	0.04794	0.18087
4X	74.5	395	4.34	0.0964	1	0.000122	79.82102	301.12953
	369	1959	0.88145	0.01944	3.95	0.00301	7.23831	27.30696
	787	4181	0.4133	0.0091	4.42	0.01370	2.32389	8.76699
	1925	10200	0.16895	0.00373	1322	0.08196	0.60748	2.29175

Figures



(a)



(b)

Figure 5-1: Scale-up CIJR (a) dimensions and (b) configuration of pressure transducers.

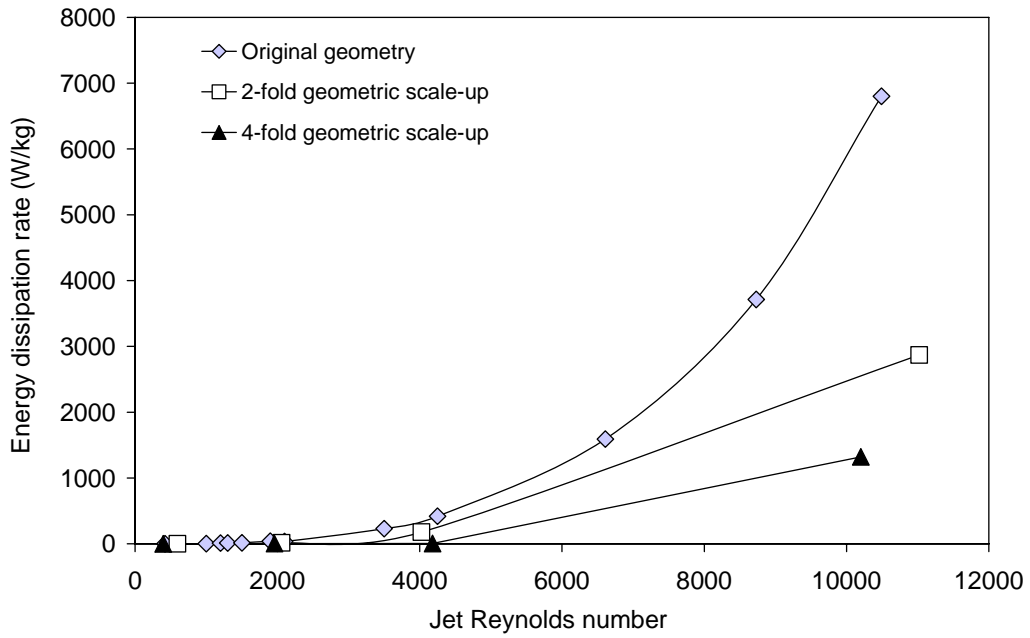


Figure 5-2: Effect of jet Reynolds number on energy dissipation rate. Based on total (mechanical) energy balance

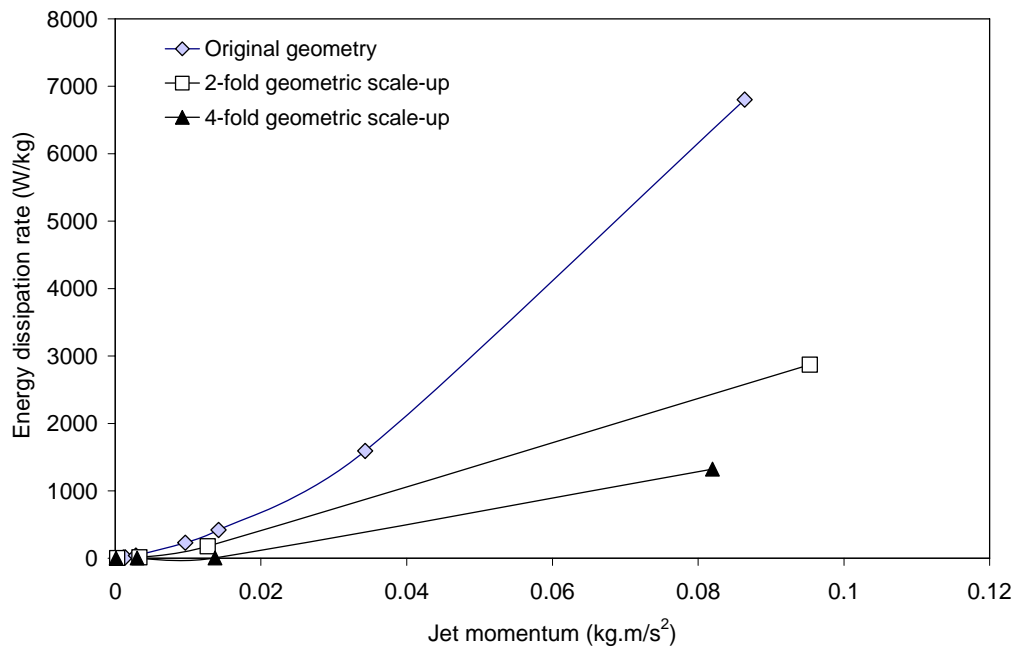


Figure 5-3: Effect of jet momentum on energy dissipation rate

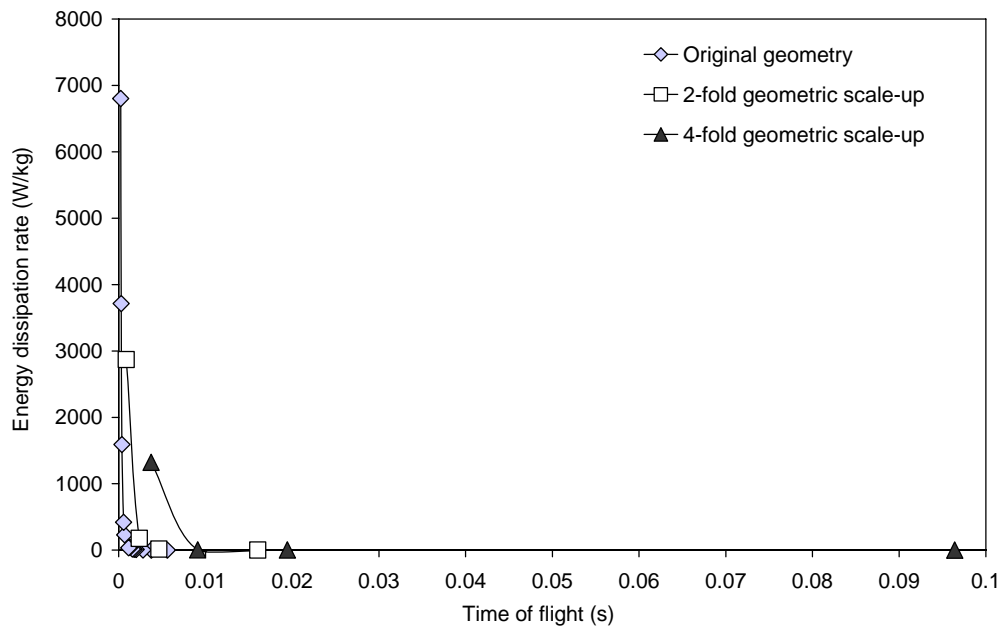


Figure 5-4: Effect of time of flight on energy dissipation rate

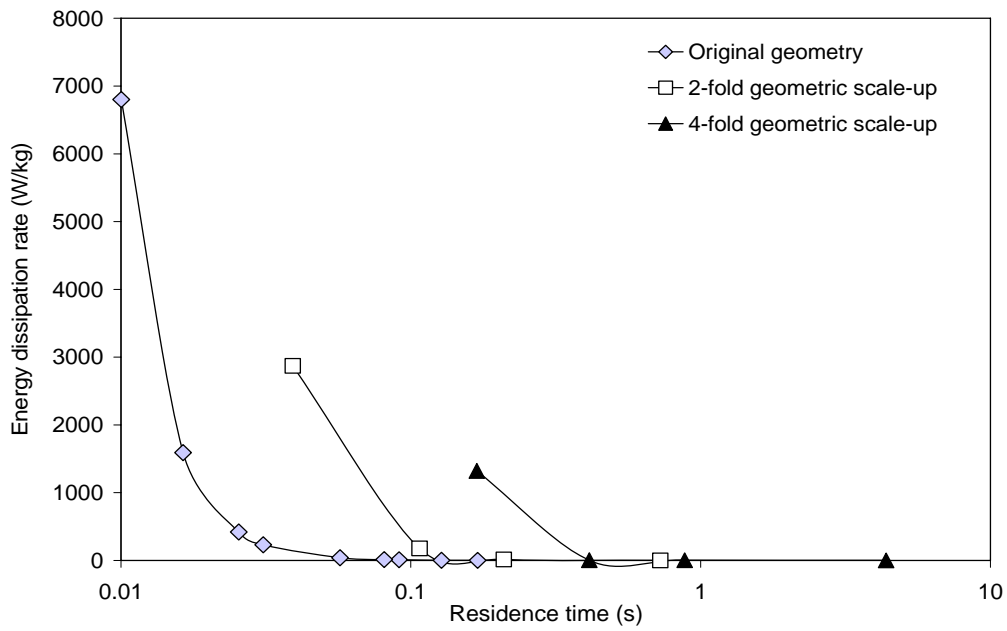
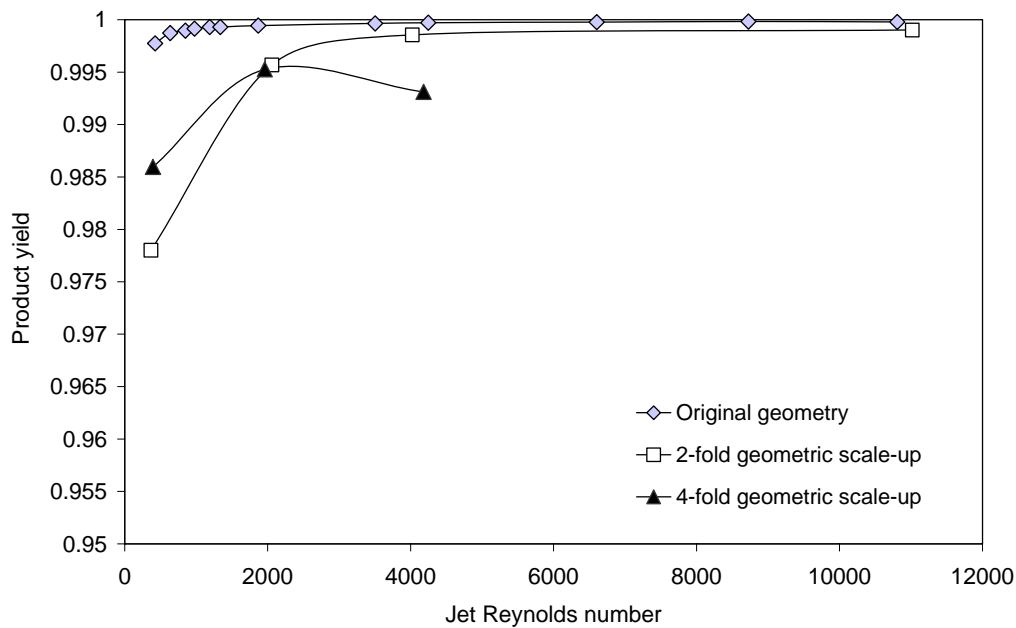
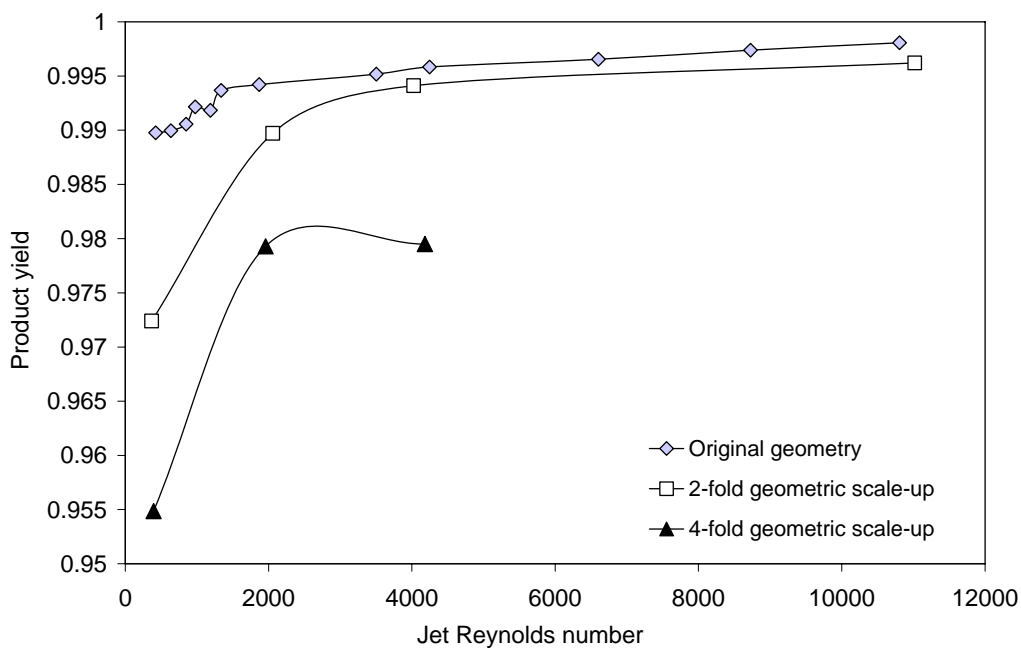


Figure 5-5: Effect of residence time on energy dissipation rate

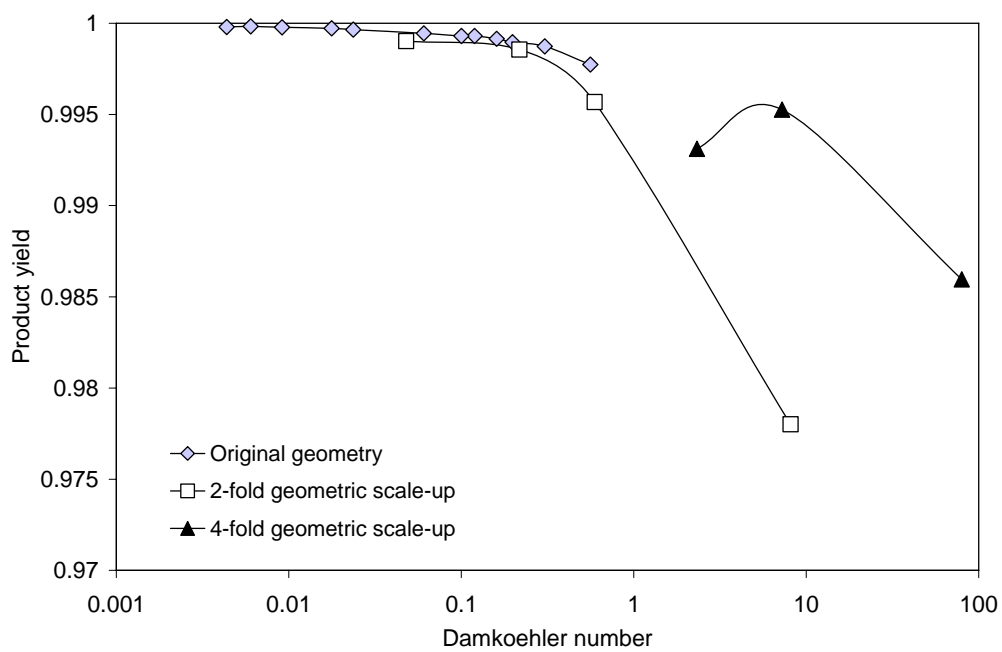


(a)

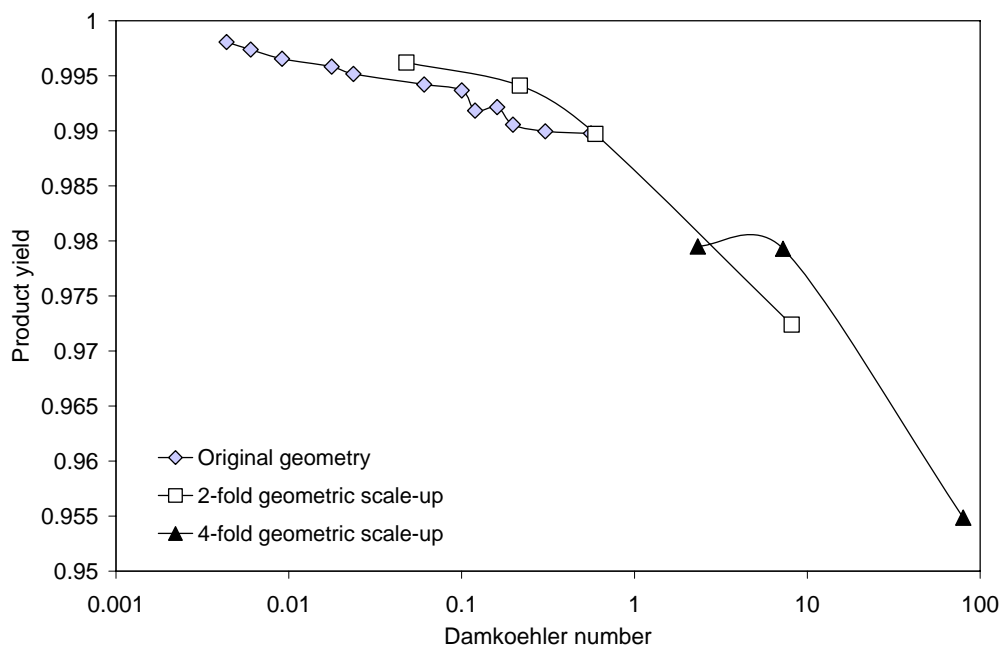


(b)

Figure 5-6: Effect of jet Reynolds number on product yield at (a) $[H^+] = 0.0936 \text{ M}$, (b) $[H^+] = 0.1818 \text{ M}$ and $[H_2BO_3^-] = 0.1818 \text{ M}$ in all experiments

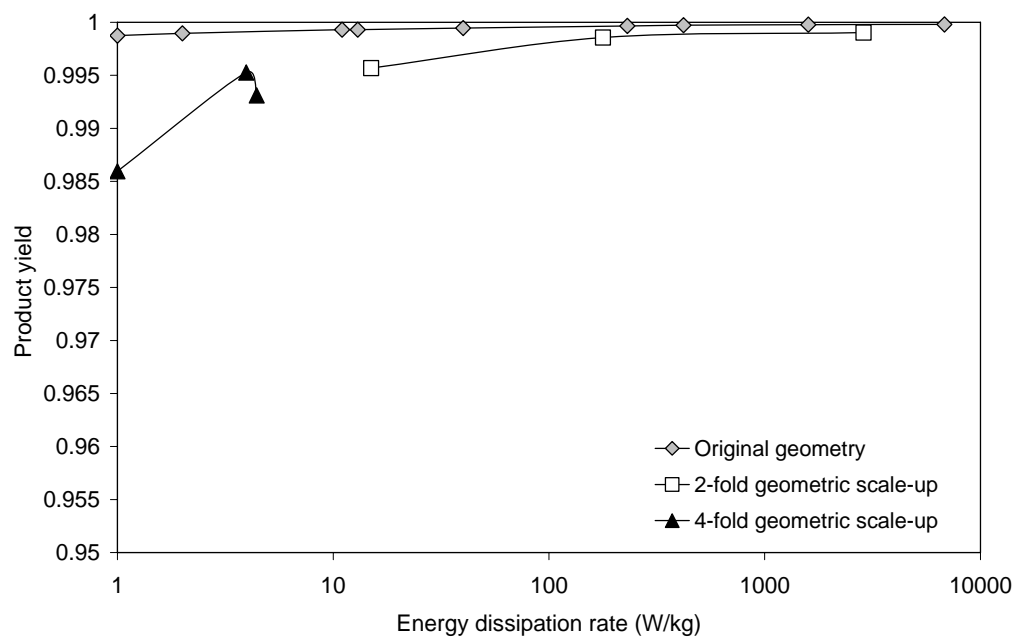


(a)

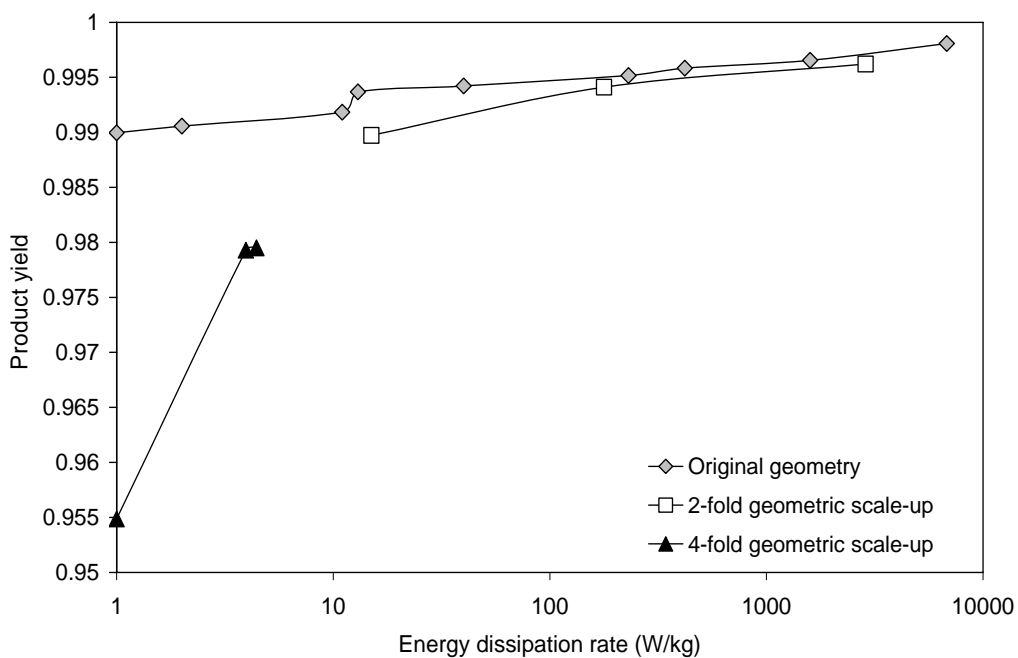


(b)

Figure 5-7: Effect of Damkoehler on product yield at (a) $[H^+] = 0.0936 \text{ M}$, (b) $[H^+] = 0.1818 \text{ M}$ and $[H_2BO_3^-] = 0.1818 \text{ M}$ in all experiments



(a)



(b)

Figure 5-8: Effect of energy dissipation on product yield at (a) $[H^+] = 0.0936 \text{ M}$ and (b) $[H^+] = 0.1818 \text{ M}$ and $[H_2BO_3] = 0.1818 \text{ M}$

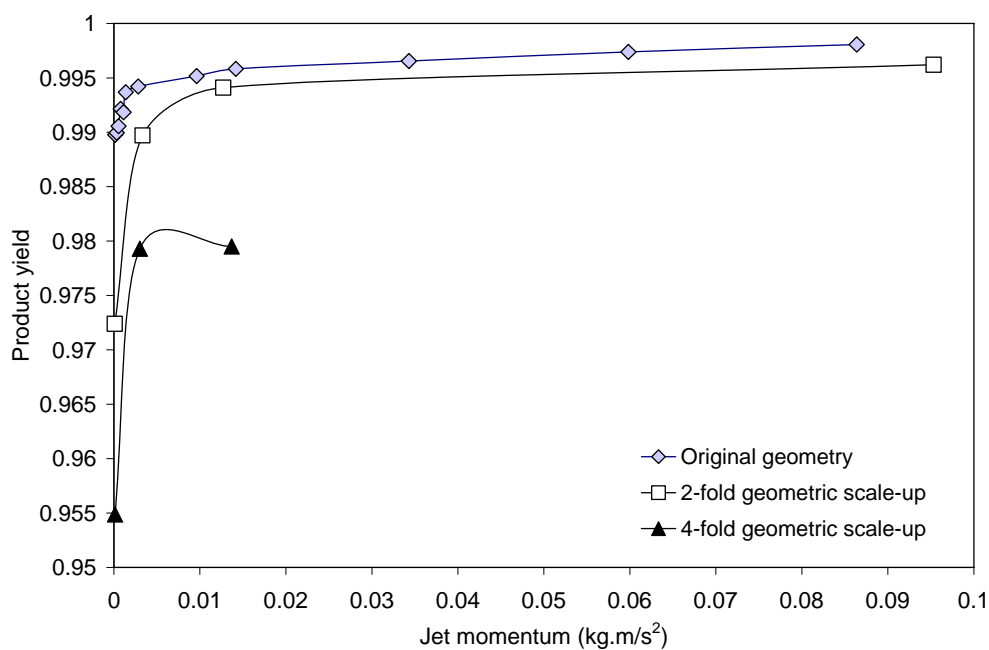


Figure 5-9: Effect of jet momentum on product yield at $[H^+] = 0.1818\text{ M}$ and $[H_2BO_3^-] = 0.1818\text{ M}$

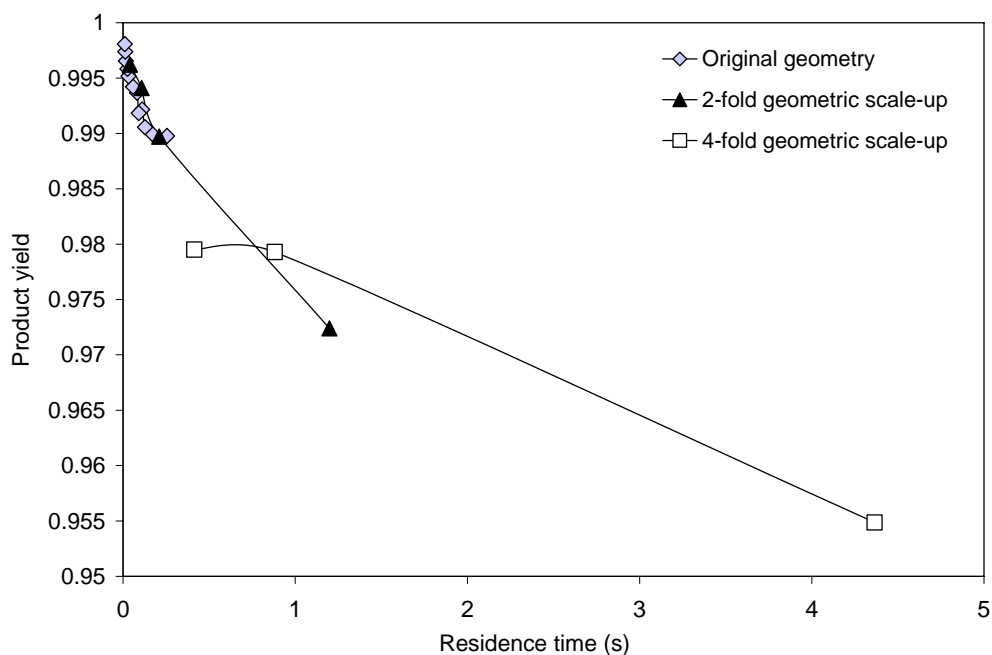


Figure 5-10: Effect of residence time on product yield at $[H^+] = 0.1818\text{ M}$ and $[H_2BO_3^-] = 0.1818\text{ M}$

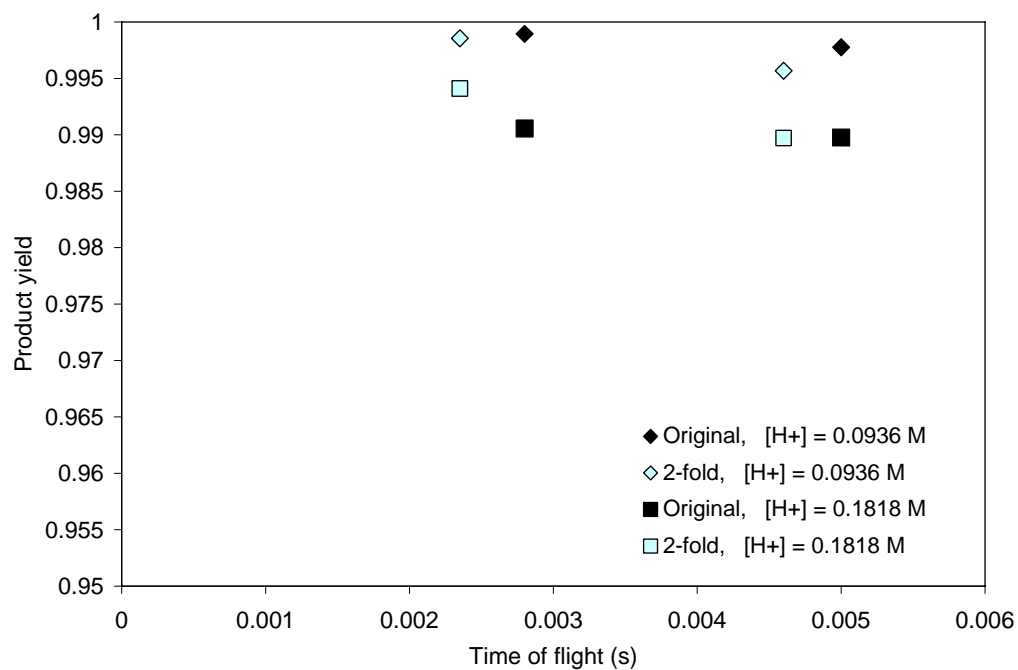
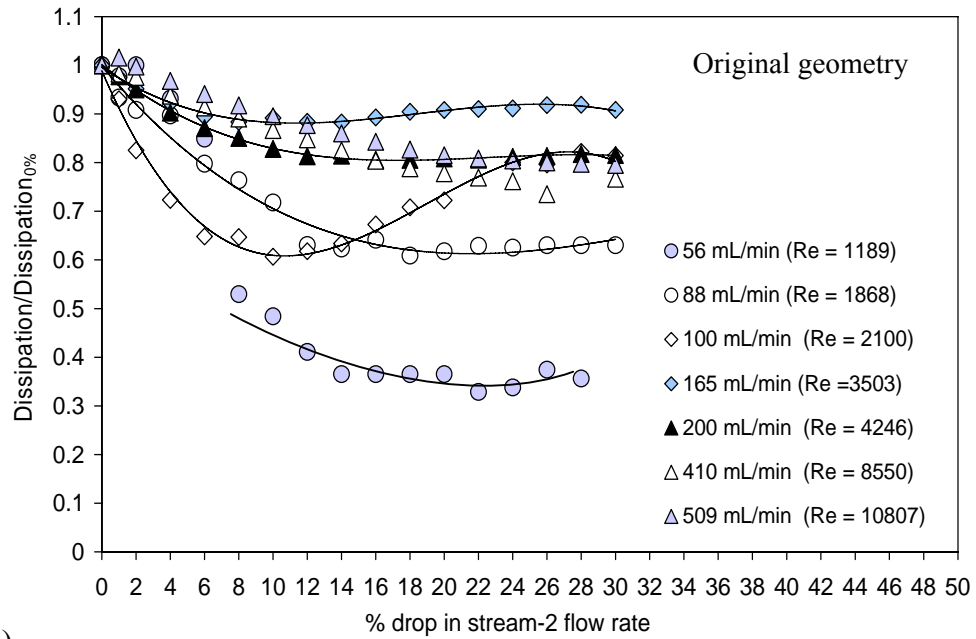
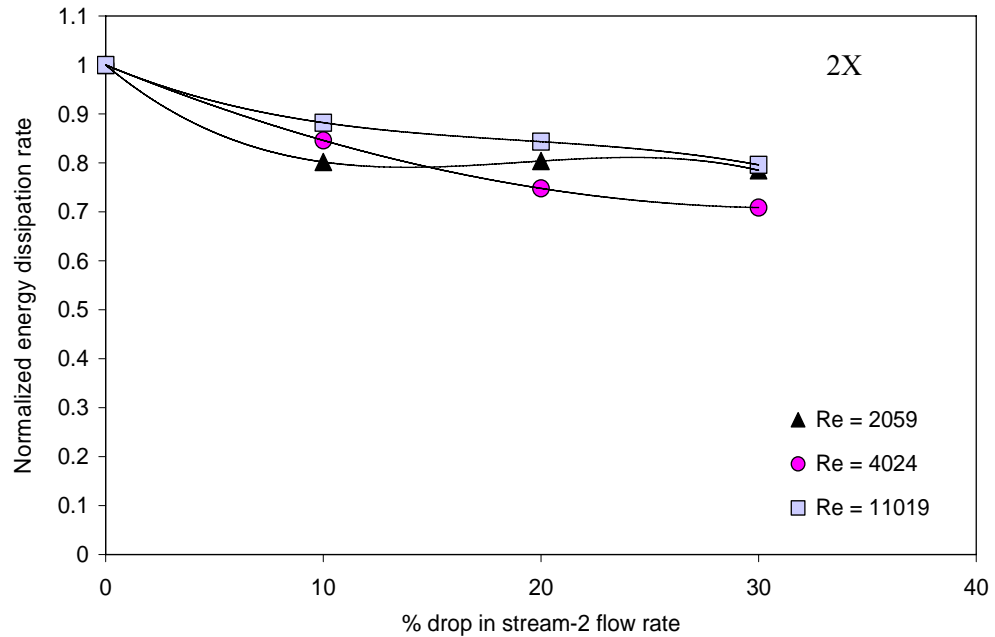


Figure 5-11: Effect of time of flight on the product yield at varying hydrogen concentrations

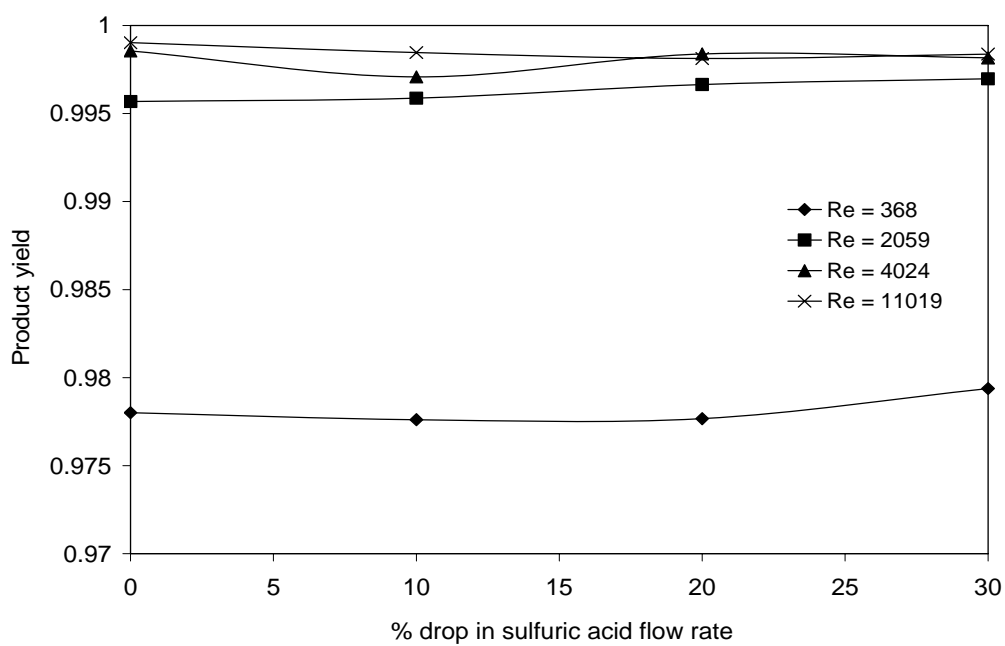


(a)

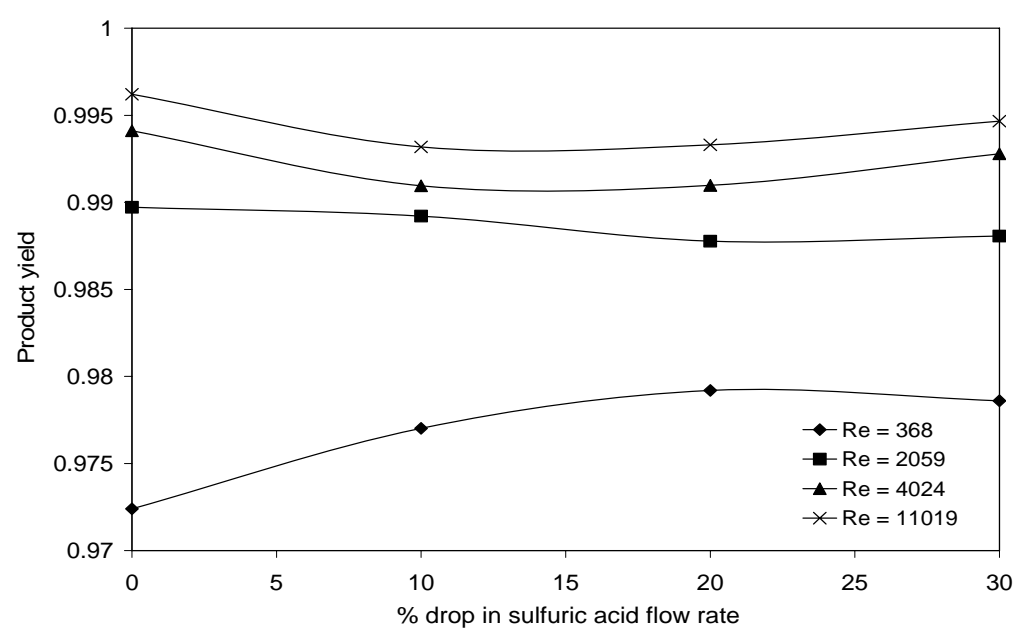


(b)

Figure 5-12: Effect of reduced flow on normalized energy dissipation rate at varying jet Reynolds number in (a) original geometry (from Siddiqui et al., 2009) and (b) 2X scale-up geometry

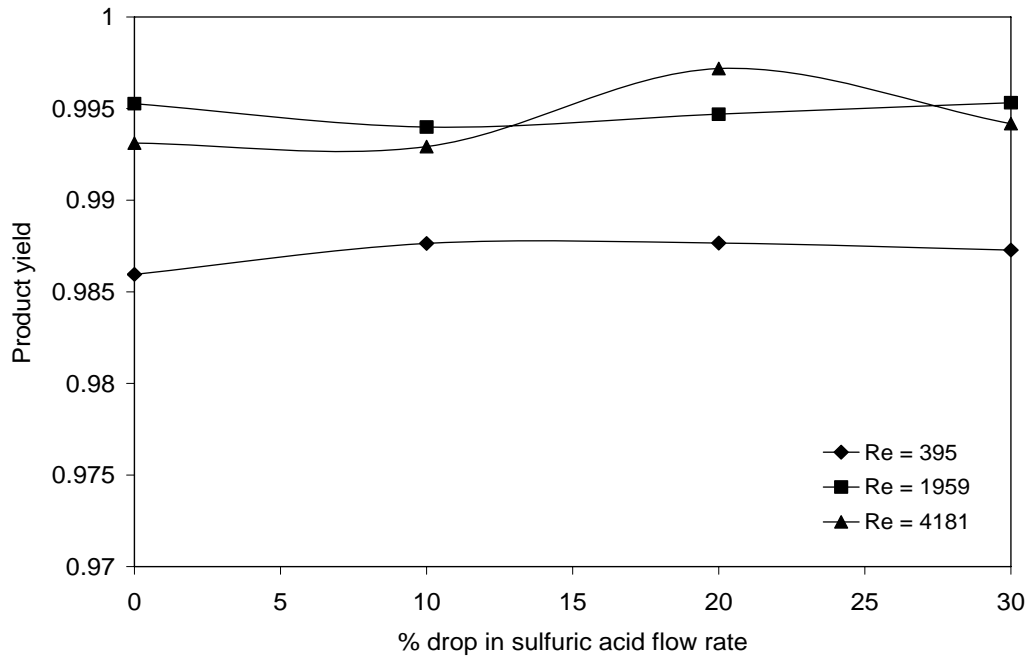


(a)

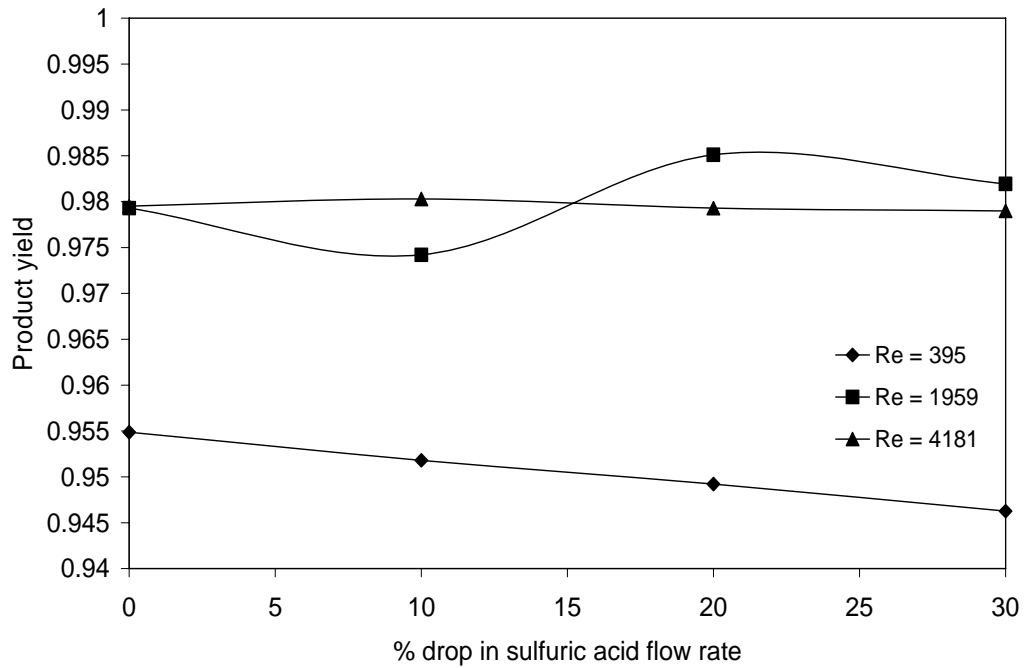


(b)

Figure 5-13: Effect of reduced sulfuric acid flow on product yield at (a) $[H^+] = 0.0936$ M, (b) $[H^+] = 0.1818$ M and $[H_2BO_3^-] = 0.1818$ M in all experiments in 2X scale-up geometry



(a)



(b)

Figure 5-14: Effect of reduced sulfuric acid flow on product yield at (a) $[H^+] = 0.0936$ M, (b) $[H^+] = 0.1818$ M and $[H_2BO_3^-] = 0.1818$ M in all experiments in 4X scale-up geometry

Literature cited

- Baldyga, J. and R. Pohorecki, 1995, *Turbulent Micromixing in Chemical Reactors – A Review*, Chem. Eng. J., **58**, 183-195.
- Bourne, J., 2008, *Comments on Iodide/Iodate Method for Characterizing Micromixing*, Chem. Eng. J., **140**, 638-641.
- Gavi, E., D.L. Marchisio and A.A. Barresi, 2007, *CFD Modelling and Scale-up of Confined Impinging Jet Reactors*, Chem. Eng. Sci., **62**, 2228-2241.
- Guichardon, P., L. Falk and J. Villiermaux, 2000, *Characterization of Micromixing Efficiency by the Iodide-Iodate Reaction System. Part II: Kinetic Study*, Chem. Eng. Sci., **55**, 4245-4253.
- Johnson, B. K. and R.K. Prud'homme, 2003, *Chemical Processing and Micromixing in Confined Impinging Jets*, AIChE J., **49 (9)**, 2264-2282.
- Kölbl, A., M. Kraut and K. Schubert, 2008, *The Iodide-Iodate Method to Characterize Microstructured Mixing Devices*, AIChE J., **54 (3)**, 639-645.
- Kölbl, A., *Further Comments on the Iodide-Iodate Reaction Method for Characterising Micromixing*, Chem. Eng. J. (Article in Press)
- Mahajan, A. J. and D.J. Kirwan, 1996, *Micromixing Effects in a Two-Impinging-Jets Precipitator*, AIChE J., **42(7)**, 1801-1814.
- Marchisio, D. L., L. Rivautella and A. Barreri, 2006, *Design and Scale-Up of Chemical Reactors for Nanoparticle Precipitation*, AIChE J., **52 (5)**, 1877-1887.
- Schaer, E. P., P. Guichardon, L. Falk and E. Plasari, 1999, *Determination of Local Energy Dissipation Rates in Impinging Jets by a Chemical Reaction Method*, Chem. Eng. J., **72**, 125-138.
- Siddiqui, S.W., Y. Zhao, A. Kukukova and S.M. Kresta, 2009, *Characteristics of a Confined Impinging Jet Reactor: Energy Dissipation, Homogeneous and Heterogeneous Reaction Products, and Effect of Unequal Flow*, Ind. Eng. Chem. Res. (Article in Press)

Chapter 6

Conclusions and Future Work

Conclusions

In this chapter main conclusions of this thesis are presented, and ideas for future work are given. The goal of this research has been to explore mixing characteristics of CIJR (1X) and scale-up (2X and 4X) geometries, investigate the effect of mixing on the product quality of homogeneous (iodide-iodate) and heterogeneous (iron oxide) chemical reactions and to use that knowledge to understand the competing steps in the agglomerate formation in a fast precipitative environment using iron oxide as the model system. The study also investigates into ways of limiting particle agglomeration under intense mixing and supersaturation conditions.

Energy dissipation, which is a measure of the mixing intensity, has been quantified in CIJR through pressure drop and mechanical energy balance across the mixing volume. Mixing performance is tracked through mixing-sensitive iodide-iodate product yield and iron oxide particle (agglomerate) size measurements. Particle agglomeration is studied through a simplified model - mixing induced nucleation, particle growth and the agglomeration steps. Major conclusions are described below.

Mixing characterization - CIJR

The flow in CIJR is found to be turbulent above jet flow rate of 165 mL/min ($Re = 3500$) and fully turbulent above a flow rate of 300 mL/min ($Re = 6600$). Energy dissipation estimated from various estimation methods have shown agreement over the investigated flow rate range, and is found to vary from 20 W/kg to 6800 W/kg. It is 100X higher than the typical average power per mass in a stirred tank. Dissipation profiles from CFD show that the peak dissipation values occur at the impingement point and decays away in both radial and axial directions. A major advantage of the CIJR over stirred tank is that all the incoming fluid must pass through the maximum energy dissipation region upon

entering the CIJR. In stirred tanks there is a persistent chance of fluid bypassing high dissipation zone, resulting in poor mixing.

Mixing-sensitive iodide-iodate and iron oxide reaction confirm high mixing efficiency of the CIJR where both feed concentration and flowrate affect the iodide-iodate product yield and the iron oxide particle size. The effect of mixing is most pronounced at high reactant concentrations. The product yield from the CIJR is consistently higher (~ 99.8%) than the best performance of stirred tank (~ 91%).

Under unequal flow conditions the energy dissipation retains 84% of the balanced flow value all the way to a 30% difference in flow rates. Iodide-iodate product yield remains stable until the flow difference begins to affect the reaction stoichiometry and the pH.

Nanoparticle agglomeration and control

The agglomerate size is seen to vary with both flowrate and feed concentration. The smallest agglomerate size is obtained at a high flow rate and high reactant concentrations. Mixing effects are more pronounced at high reactant concentrations. Stabilizers added insitu see limited success in limiting agglomeration. Though an increase in the TEG additive quantity decreases hard agglomerate size, there isn't any significant change in the primary particle size. Dextran gives the smallest primary particle size but largest agglomerates. TEG gives largest primary particle but smallest hard agglomerates. Post-reaction sonication helps in dispersing soft agglomerates, but insitu sonication shows no significant reduction in agglomerate size with or without stabilizer. The limited performance of in situ sonication could be due to a 'transient' balance between the breakage of ill-formed agglomerates and increase in the collision rate with the increase in turbulence.

Nucleation, particle growth and agglomeration mechanisms of nanoparticles

The biggest primary particles and the smallest hard agglomerates are obtained under high flow rate and high reactant concentrations. The number of primary particles agglomerating together to form a hard agglomerate is found to decrease with primary particle size. This indicates to the size dependent agglomerative tendency of the primary particles.

Both diffusional growth of particles and bridge formation between particles is found to be very rapid and occur within the residence time of the reactor. pH doesn't have significant effect on hard agglomerate size but smaller primary particle (~ 8 nm) are obtained at highest pH values. Brownian, laminar and turbulent aggregation models have been successfully used to understand particle agglomeration occurring at various length scales in mixing process. Hard agglomerate are always smaller than the Kolmogorov length scale. Shear dominates collision and agglomeration between small particles (> 100nm) due to turbulent velocity fluctuations. Brownian agglomeration is the dominating collision mechanism for the smallest particles (< 70nm). Between these limits, both mechanisms may be expected to play a role.

Mixing Characterization - Scale-up CIJRs

Energy dissipation is seen to decrease on scale-up due to decrease in jet velocity and the hydrostatic pressure at constant Reynolds number. At fully turbulent Re of 10,000, energy dissipations are estimated to be 6800, 3000 and 1250 W/kg in original, 2X and 4X CIJR respectively.

Mixing performance curves are observed to merge together on scale-up with Damkohler number. Re and residence time could also be used to scale-up mixing performance in geometrically scale-up CIJRs.

Under unbalance flow and momentum conditions in fully turbulent regime (Re = 10,000), 2X geometry retains 84% of the balanced flow value all the way to a 30% difference in flow rate. The product yield values are stable upto 30% unbalance in flow in 2X and 4X scale-up geometries. However at very flow rates

the jets failed to impinge in 4X geometry. Product yield results indicate that the 4X scale-up gives poor mixing performance than the original and 2X scale-up CIJR. It is thus proposed that 2X is the likely upper limit for achieving a balance between high production capacity and good micromixing capability.

Future work

The present thesis is an attempt to study the impact of mixing along with reactant concentration on the quality (yield and particle size) of the product resulting from fast chemical reactions. Whereas product yield is used as a tool to characterize mixing, tracking particle (agglomerate) size is the ultimate goal. This study supports that mixing effects are important when synthesizing particles via fast precipitation route. We have made several assumption over the course of the study like the primary particles and hard agglomerates are well formed and spherical, complete nucleation precedes particle growth, the process: nucleation, particle growth and agglomeration is completed within the reactor and adsorption of stabilizer over the particle surface is complete within the reactor. All reactive studies have been experimental in nature.

Future efforts could be to use computation means to study - nucleation, particle growth, bridge formation, particle stabilization and particle agglomeration, to fully understand the competing mechanisms that determine 'final' hard agglomerate size. Understanding of each of these intermediate steps is of great usefulness to industrial applications. Nucleation, particle growth and bridge formation are dependent on local supersaturation and therefore on the local hydrodynamic conditions within the CIJR. Nucleation is however known to be significantly more dependent on local supersaturation conditions than particle growth. These 'local' effects need to be incorporated in any future studies. Also we haven't taken into consideration any surface-chemistry effects while forming agglomerates. It may also be possible to use computational-chemistry towards a better understanding of the process. It is thus a numerical challenge to incorporate multiple mechanisms into one computational model. This thesis is thus a step to further an understanding in mixing and precipitation processes and

to provide an experimental proof that mixing affects particle growth and therefore particle agglomeration.

